Doctoral Dissertation
Doctoral Program in Electrical, Electronics and Communications Engineering
($36^{\text{th}}$ cycle)

# Deterministic Design of Metasurface Antennas

**Lucia Teodorani**
* * * * *

**Supervisor**
Prof. Giuseppe Vecchi

**Doctoral examination committee**
Prof. Andrea Massa, Referee, Università di Trento
Prof. Enrica Martini, Referee, Università degli Studi di Siena
Prof. David González-Ovejero, CNRS
Prof. Jordan Budhu, Virginia Polytechnic Institute and State University
Prof. Zvonimir Sipus, University of Zagreb

Politecnico di Torino
2024

I hereby declare that, the contents and organisation of this dissertation constitute my own original work and does not compromise in any way the rights of third parties, including those relating to the security of personal data.

Lucia Teodorani
2024

# Summary

This Thesis focuses on the deterministic design of metasurface antennas.

Metasurfaces are metamaterial-inspired surfaces composed of sub-wavelength elements; they possess the ability to manipulate electromagnetic waves with unprecedented flexibility and have been employed in a wide range of antenna applications. Metasurface design relies on the macroscopic approximation of its electromagnetic response by means of a homogenized Impedance Boundary Condition (IBC). The determination of the impedance profile that may guarantee the desired antenna performance constitutes the first crucial step in the design process.

The research work involves both static and reconfigurable antennas.

A novel beam-scanning dual-metasurface antenna is designed, where beam steering is achieved by pairing a sinusoidally-modulated reactance surface with a varactor-loaded reconfigurable metasurface.

A new, generalized deterministic numerical method for the full design of metasurface antennas is developed that allows to self-consistently include 3-D metallic feeding structures inside the optimization instance, thus enabling accurate estimation of the antenna performances, e.g. the peak realized gain. This method is successfully applied to the design of several edge-fed rectangular metasurfaces and center-fed circular antennas, and the results are validated with full-wave simulations. The most difficult designs involving broadside-radiating leaky wave antennas are also fabricated and measured.

Finally, the proposed automated design method, initially developed to deal with isotropic metasurfaces, is modified to be able to synthesize fully tensorial metasurfaces, without any a priori assumption on the tensor impedance profile.

# Acknowledgements

The author would like to thank Dr. Francesco Vernì, Dr. Marcello Zucchi, Dr. Rossella Gaffoglio and Dr. Giorgio Giordanengo for being amazing collaborators and co-authors of some of the work presented in this Thesis. Also thanks to the wonderful research team at Fondazione LINKS and, of course, to my supervisor Professor Giuseppe Vecchi.

This work was supported by the Italian Ministry of Research PRIN 2017S29ZLA "Metasurface Antennas for Space Applications" and PRIN 2020EY2LJT "METEOR".

# Contents

# List of Tables

# List of Figures

# Chapter 1

# Overview

The research work reported in this Thesis has been focused on the design and realization of metasurface antennas. This Chapter outlines the general framework of the research; a more in-depth analysis of the current state of the art and related literature is carried out at the beginning of every Chapter.

Metasurfaces, i.e., metamaterial-inspired surfaces composed of sub-wavelength elements, have emerged as a transformative paradigm in antenna design [1]. They possess the ability to manipulate electromagnetic waves with unprecedented flexibility, offering many opportunities to tailor and enhance antenna functionalities. They have been employed in a wide range of applications, including lenses, reflectarrays and reconfigurable intelligent surfaces (RIS).

Metasurfaces are most commonly implemented with printed conductive elements over a dielectric substrate; one or more metallization layers can be used depending on the application. Varying the dimensions of these sub-wavelength "unit cells" allows to control the electromagnetic response of the metasurface.

Since metasurface antennas typically reach a large size in terms of wavelengths, the full-wave analysis of these structures is challenging, and even more so for any design approach based on such level of analysis. However, it is possible to approximate the electromagnetic behaviour of metasurfaces at a geometrical scale of the order of the wavelength, in the following called "macroscopic". At this macroscopic scale, the local field can be averaged ("homogenized") and represented by an *Impedance Boundary Condition* (IBC) that relates the tangent electric and magnetic fields. This approximation as continuous distribution of equivalent surface impedance has facilitated the electromagnetic analysis of large metasurface antennas and enabled a two-step design process: first, the impedance spatial distribution that serves the desired application is determined; then, this surface impedance is physically implemented using suitable unit cells.

The mapping between unit cell and surface impedance is usually based on the assumption of local periodicity to account for inter-cell couplings, and it is well documented in literature [2].

This Thesis focuses on the first step in the design of metasurface antennas, i.e. the determination of the proper impedance profile that satisfies specific application-dependant requirements, typically related to the radiation pattern of the antenna.

The existing design methods can be divided into two categories: analytically-based approaches versus automated algorithms. Methods belonging to the first category usually involve analytical modulations of the surface impedance [3, 4, 5], and can be interpreted under the paradigm of Leaky-Wave Antennas (LWAs).

Fully-numerical design algorithms are essentially optimizations, and the related problem is not convex. They are further divided into two categories: statistics-based global optimizations, and deterministic optimizations. The former category involves meta-heuristics like particle swarm, genetic algorithms etc.; they have the potential of avoiding local minima (maxima) but require a large number of evaluations of the functional to be minimized (or maximized). This number is essentially exponential with respect to the number of design parameters, and each evaluation requires a full-wave simulation; hence, they are practically forced to employ parameterizations that derive from the analytical approach, with a limited number of parameters. Deterministic approaches are not constrained by analytical considerations and benefit from a much higher number of degrees of freedom; in turn, they may fall into local traps. These methods can generate unconventional impedance profiles that satisfy arbitrary design requirements [6, 7, 8].

In this Thesis, both analytical and deterministic numerical design methods are explored in the framework of different applications. Chapter 2 presents the design of a beam-scanning dual-metasurface antenna, where beam steering is achieved by pairing a radiative, modulated impedance surface with a reconfigurable metasurface; for this purpose, analytically-based techniques are employed, such as the leaky-wave radiation arising from sinusoidally-modulated reactance surfaces [3] and the transverse equivalent network analysis of multilayered structures [9]. These approximated analytical tools allow nonetheless to design with sufficient accuracy a novel beam-scanning antenna in which reconfigurability is conveyed by on-plane varactors in a tunable-impedance surface. In Chapter 2 the limitations given by the sinusoidal impedance modulation on the beam-scanning antenna are also highlighted, justifying the interest in automated numerical design methods.

In this perspective, Chapter 3 presents a novel automated method for the design of scalar metasurface antennas that includes realistic 3-D feeding structures inside the optimization instance. The proposed method is a generalization of [6]. The proper modeling of the feed and launching structure inside the optimization instance leads to a fully self-consistent design of the entire metasurface antenna and ensures that the synthesized structure behaves as expected in a realistic environment. The inclusion of metallic feeding structures in the synthesis algorithm is made possible by introducing a cost function that enforces the PEC condition in the corresponding regions, in self-consistent interaction with the IBC areas where the

unknown impedance pattern must be synthesized. In Chapter 3, this method is described and applied to two different geometries of metasurface antennas: a circular antenna fed by a central vertical pin with annular matching ring, and a rectangular "strip-like" metasurface connected to an input coaxial cable by a tapered microstrip section. Several designs, characterized by more or less difficult radiation patterns, are presented, and the far-field results predicted by the automated design method are compared with full-wave simulations of the complete antennas, showing excellent agreement.

The proposed design method maximizes the realized gain, accounting for the interactions between launching structure and metasurface, and thus leads to the synthesis of an impedance surface with a low input reflection coefficient. This consideration has prompted its testing in the design of broadside-radiating, edge-fed LWAs, which notoriously suffer from the open stopband problem at broadside [10]. The design of a broadside-radiating "strip-like" LWA is firstly presented in Chapter 3, demonstrating the capability of the proposed generalized method to effectively overcome the open stopband issue.

Chapter 4 offers experimental validation of the method. Two prototypes of numerically-synthesized, broadside-radiating LWAs, built on two different dielectric substrates, are fabricated and their performance measured. The agreement between design, simulation and measurement proves that the proposed automated design method can indeed synthesize metasurface antennas in a reliable, self-consistent way, ensuring the persistence of the desired radiation properties from the design stage up to fabrication.

Chapter 5 introduces a new version of the automated design method tailored to the design of tensor metasurfaces – whereas its initial version considered scalar impedances. Given the greater capabilities in terms of manipulation of electromagnetic waves possessed by tensor impedance surfaces, enabling the design algorithm to deal with this kind of metasurfaces is the natural step forward. The main advantage of the underlying optimization method is that it optimizes the (equivalent) current on the metasurface; the impedance is then recovered from this current. The extension to tensor impedance requires two fundamental steps: first, a new strategy must be implemented to retrieve the tensor impedance components from the optimum current density; second, new IBC realizability functionals must be defined to enforce the synthesis of tensor impedances with prescribed properties (e.g., capacitive). Preliminary numerical results relative to the design of a circular tensor metasurface radiating a broadside pencil beam show that the automated design method is capable of synthesizing tensor impedance surfaces with this approach.

Finally, in Chapter 6, a summary of the main achievements of this research work is given, along with possible future developments and improvements.

# Chapter 2

# Beam-Scanning Dual-Metasurface Antenna

This chapter reports the published article [11].

Beam-scanning antennas are employed in a wide range of applications, such as in satellite communications and 5G networks. Current commercial solutions rely mostly on electronically reconfigurable phased arrays, which require complex feeding networks and are affected by high losses, high costs, and are often power-hungry. In this Chapter, a novel beam scanning architecture employing a pair of planar metasurfaces, for use in thin reconfigurable antennas, is presented and experimentally demonstrated. The structure consists of a radiative passive (non-reconfigurable) modulated metasurface, and a second metasurface that controls beam pointing, operating as a variable-impedance ground plane. Unlike other existing approaches, surface impedance variation is obtained by on-plane varactor diodes, no vias and a single voltage bias. This Chapter presents a design procedure based on an approximate theoretical model and simulation verification; a prototype of the designed antenna is fabricated for operation in X band, and a good agreement between measured results and simulations is observed. In the presented simple embodiment of the concept, the angular scanning range is limited to 10°; this limitation is discussed in view of future applications.

## 2.1 Introduction

In recent years, reconfigurable antennas have been the subject of constantly growing interest, since beam steering is required in a wide range of present, emerging and future applications, as in satellite communications, radars, 5G and beyond-5G networks [12, 13, 14].

Commercial solutions, current and under development, rely mostly on electronically reconfigurable phased arrays, but the inherent complex feeding networks and

high losses make these antennas less than optimal [15]; this has prompted research into alternative architectures. Among these, solutions are favored in which the radiating part and the power distribution structure coexist; the interplay between wave guiding (spatial power distribution) and radiation is well captured by the leaky-wave paradigm [3, 10, 16], that allows for approximate designs. Beam steering at fixed frequency has been achieved using materials with tunable electric properties [17, 18, 19, 20], done electromechanically [21] or by employing a multitude of (lumped) active components like varactors [22, 23, 15, 24, 25, 26, 27].

In [27], varactors were used to individually load the grooves of a corrugated microstrip line, with operation below 6 GHz; the resulting antenna was thin and simple, but the use of (TEM) microstrip guiding likely affected operation at higher frequencies because of the intrinsic losses. In [23], varactors were employed as tuning elements for a high-impedance surface in a 1-D Fabry-Perot leaky-waveguide; the inherent transverse resonance mechanism required a thickness of about 3/4 wavelength. In [15], varactors were inserted in tunable-impedance phase-shifting side walls in a waveguide antenna (a modified WR90) derived from a standard waveguide slot array (in leaky-wave operation mode).

One of the most recent uses of metasurfaces is as refracting or reflective intelligent surfaces [28, 29, 30]; also beamformers [31] for satellite-terrestrial networks have been revamped.

In this Chapter, a novel fixed-frequency beam scanning mechanism is introduced and demonstrated. The main goal of the present study is to investigate on the potential of beam steering via distributed varactor diodes with a *single* DC control, i.e. on-plane varactors and no vias: this can be realized with existing standard low-cost technologies (e.g. pick-and-place). Using the metasurface paradigm, varactors can act as variable (reactive) loads in a suitably designed texture, yielding a variable impedance surface, with surface impedance value controlled by the DC bias.

By combining a modulated upper metasurface (responsible for radiation) with a reconfigurable impedance plane (responsible for beam scanning) we effectively separate RF wave propagation from DC bias, while maintaining a very small form factor.

In this Chapter, Section 2.2 illustrates the adopted design techniques and describes the geometry of the designed antenna, while simulation results and experimental measurements of the fabricated prototype are reported in Section 2.3. In Section 2.4, these results are discussed and future work is outlined. Finally, conclusions are drawn in Section 2.5.

## 2.2 Concept and Design

### 2.2.1 Principle of Operation

The beam scanning mechanism is conceived as a *dual* metasurface structure (see Fig. 2.1a). Radiation is effected by a (static) transparent metasurface with metal texture on a dielectric (inspired by [4]); in a fixed-beam configuration, the radiating metasurface would be backed by a metal plane providing wave guiding. Here, the ground plane is replaced by a *tunable-impedance metasurface*. The principle of operation is based on the radiation of a guided wave, whose phase velocity is controlled by the variable-impedance surface.

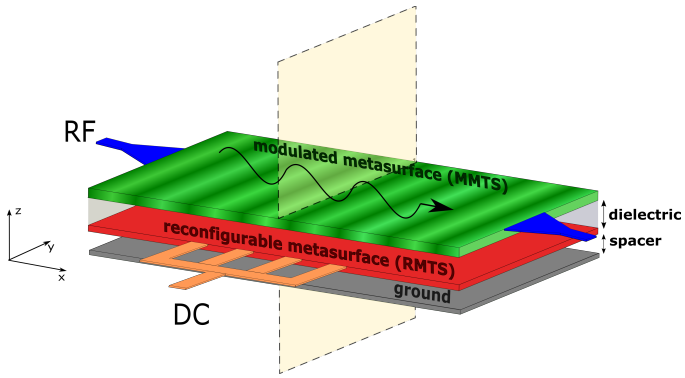


(a)

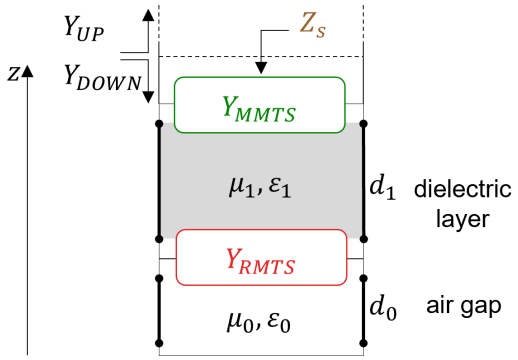


(b)

Figure 2.1: Structure of the proposed antenna. (a) Schematic architecture. (b) Transverse equivalent network: $Y_{\mathrm{MMTS}}$ is the admittance of the upper metasurface, $Y_{\mathrm{RMTS}}$ is the admittance of the lower (reconfigurable) metasurface, $d_1$ is the thickness of the dielectric layer, $d_0$ indicates the air gap, $Y_{\mathrm{UP}}$ and $Y_{\mathrm{DOWN}}$ are the admittances looking up and down from the interface between the antenna and free space, $Z_{\mathrm{s}}$ is the equivalent impenetrable surface impedance that approximates the whole multilayer structure.

The present study considers an antenna with scan in the vertical plane; the transverse size can range from small to multi-wavelength, depending on the type of feeding structure; for the sake of simplicity here the intermediate size of one wavelength was considered, which would allow for star-type 2D scanning [32].

Radiation of a guided mode is conveniently framed in the leaky-wave paradigm; hence, radiation happens via the spatially-modulated upper metasurface, exploiting both well-known results [3] and recent advances in metasurface antennas [4]. Operation principle, and thus first-pass design, can be conveniently understood for the simplest modulation of the radiating metasurface, i.e. for the sinusoidal one [4]:

$$Z_{\mathrm{s}}(x) = \mathrm{j}X_{\mathrm{s,ave}}\left[1 + M\cos\left(\frac{2\pi}{p}x\right)\right] \tag{2.1}$$

where $Z_{\mathrm{s}}$ is the equivalent impenetrable surface impedance that approximates the whole multilayer structure and takes into account the effects of both metasurfaces (Fig. 2.1b), $x$ is the coordinate along the direction of wave propagation, $M$ is the modulation index, $p$ is the modulation period, and $X_{\mathrm{s,ave}}$ is the average surface reactance.

In this case, leaky-wave radiation happens for the $n = -1$ Floquet harmonic of the traveling wave [3, 4]; for TM mode propagation, the radiation angle $\theta_{-1}$ is linked to the average surface reactance $X_{\mathrm{s,ave}}$ by the approximate expression [4, 27]:

$$\theta_{-1} = \arcsin\left(\sqrt{1 + \left(\frac{X_{\mathrm{s,ave}}}{\eta_0}\right)^2} - \frac{2\pi}{k_0 p}\right) \tag{2.2}$$

where $\eta_0$, $k_0$ are the free-space impedance and wavenumber, respectively.

### 2.2.2 Design method

The design is carried out in terms of standard guided-mode analysis [9] via the Transverse-Resonance Equation (TRE). As depicted in Fig. 2.1b, the total admittance from the antenna-free space boundary is controlled by the variable impedance layer, resulting in a controllable wavenumber of the guided wave.

The use of the usual "adiabatic" approximation for slow variations of the top impedance allows to approximate the antenna with a transverse equivalent network (TEN) (see Fig. 2.1b) at any given sample point of the modulated structure. From this transmission-line representation of the structure, the *local* value of the surface impedance $Z_{\mathrm{s}}(x)$ can be retrieved by solving the corresponding TRE:

$$Y_{\mathrm{UP}}(x) + Y_{\mathrm{DOWN}}(x) = 0 \tag{2.3}$$

where $Y_{\mathrm{UP}}$ and $Y_{\mathrm{DOWN}}$ are the admittances looking up and down from a reference plane located at the interface between the antenna and free space. Indicating with

$d_1$ the thickness of the dielectric layer between the two metasurfaces and with $d_0$ the air gap between reconfigurable metasurface and ground plane, standard transmission-line theory yields [33]:

$$Y_{\text{UP}} = Y_0^{\text{TM}} \tag{2.4}$$

$$Y_{\text{DOWN}} = Y_{\text{MMTS}} + Y_1^{\text{TM}} \frac{Y_{\text{EGP}} + \text{j}Y_1^{\text{TM}} \tan\left(k_{z1} d_1\right)}{Y_1^{\text{TM}} + \text{j}Y_{\text{EGP}} \tan\left(k_{z1} d_1\right)} \tag{2.5}$$

$$Y_{\text{EGP}} = Y_{\text{RMTS}} - \text{j}Y_0^{\text{TM}} \cot\left(k_{z0} d_0\right) \tag{2.6}$$

where $Y_{\text{MMTS}}$ is the admittance of the upper metasurface, $Y_{\text{RMTS}}$ is the admittance of the lower (reconfigurable) metasurface and $Y_{\text{EGP}}$ is the admittance of the equivalent ground plane looking down from just above the tunable impedance plane (Fig. 2.1b). In (2.4)-(2.6), $Y_0^{\text{TM}}$ and $Y_1^{\text{TM}}$ are the TM wave admittances in free space and dielectric substrate:

$$Y_0^{\text{TM}} = \frac{\omega \varepsilon_0}{k_{z0}} \tag{2.7}$$

$$Y_1^{\text{TM}} = \frac{\omega \varepsilon_1}{k_{z1}} \tag{2.8}$$

where $k_{z0}$ and $k_{z1}$ are the wavenumbers in the transverse direction:

$$k_{z0} = \sqrt{k_0^2 - k_x^2} \tag{2.9}$$

$$k_{z1} = \sqrt{k_1^2 - k_x^2} \tag{2.10}$$

and $k_x$ is the longitudinal wavenumber. From (2.5) and (2.6) it can be seen that the solution of the TRE depends on the sheet admittances of both metasurfaces ($Y_{\text{MMTS}}$ and $Y_{\text{RMTS}}$). Since all quantities in (2.4)-(2.6) can be expressed as a function of $k_x$, it is possible to solve (2.3) for $k_x$ and then obtain the (local) surface impedance as:

$$Z_{\text{s}} = \text{j}X_{\text{s}} = \frac{1}{Y_{\text{DOWN}}} \tag{2.11}$$

It is worth noting that the longitudinal wavenumber $k_x$ considered above is used only to compute the local surface impedance based on the adiabatic approximation, and does not correspond to the actual wavenumber of the leaky wave that arises from the modulation of such impedance.

The average value of $X_{\text{s}}$ is linked to the radiation angle through (2.2). This means that tuning $Y_{\text{RMTS}}$ directly affects the beam direction, thus validating the concept of this architecture. Once a desired radiation angle for the $n = -1$ harmonic is chosen, the modulation period $p$ is retrieved from (2.2) after selecting a proper value of $X_{\text{s,ave}}$ among those physically attainable with the considered structure.

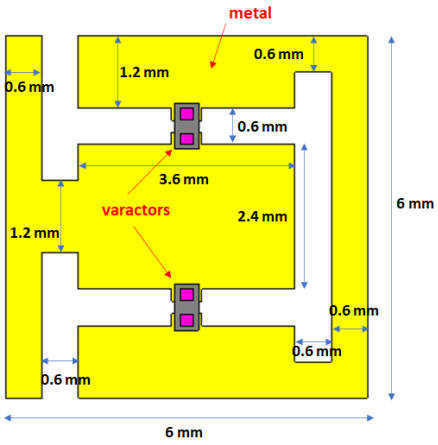


Figure 2.2: Unit cell of the reconfigurable metasurface.

The design process now requires the choice of the geometry of both metasurfaces and the computation of their sheet admittances $Y_{\text{MMTS}}$ and $Y_{\text{RMTS}}$, in order to solve (2.3). For the upper layer, a unit cell is chosen such that its admittance can be easily modulated by varying only one geometric feature, e.g. the gap width between two adjacent metal strips, as in [4]. For the implementation of the tunable metasurface, the unit cell shown in Fig. 2.2 is used. This shape is inspired by the geometry described in [34]. Each unit cell contains two MAVR-011020-1411 varactors, that are approximated as RC series elements for simulation purposes; the values of resistance and voltage-dependent capacitance are taken from the manufacturer's datasheet [35]. Varying the bias voltage changes the varactors' capacitance, which in turn affects the sheet admittance of this layer. In the design phase, the equivalent resistance of the varactors is ignored, thus allowing to deal with purely imaginary sheet admittances. The resistive component of the equivalent RC series element will be included when simulating the complete antenna, in order to accurately predict the performance of the fabricated prototype.

The computation of $Y_{\text{MMTS}}$ must be carried out for every possible value of the gap width in the constitutive unit cell, while $Y_{\text{RMTS}}$ must be determined for every possible biasing state of the varactor diodes. This allows to obtain the equivalent impenetrable surface reactance $X_{\text{s}}$ by solving the TRE for every combination of gap width in the upper metasurface and capacitance value in the reconfigurable plane. Moreover, at any given frequency both admittances are also dependent on the longitudinal wavenumber $k_x$ [36, 23]: namely, $Y_{\text{MMTS}} = Y_{\text{MMTS}}(g, k_x)$ and $Y_{\text{RMTS}} = Y_{\text{RMTS}}(C, k_x)$, where $g$ and $C$ are the gap width and the varactors' capacitance, respectively. Therefore, to compute such admittances the technique described in [23, 37] is adopted, where the dependence on the longitudinal wavenumber is retrieved by performing scattering simulations of the constitutive unit cells for different angles of incidence. In particular, similarly to what is done in [37], the

rational functions used to express $Y_{\text{MMTS}}$ and $Y_{\text{RMTS}}$ are:

$$Y_{\text{MMTS}}(g, k_x) = \text{j}\frac{[g - g_{\text{z1}}(k_x)]\,[g - g_{\text{z2}}(k_x)]}{g\,[g - g_{\text{p1}}(k_x)]\,[g - g_{\text{p2}}(k_x)]} \tag{2.12}$$

$$Y_{\text{RMTS}}(C, k_x) = \text{j}\frac{[C - C_{\text{z1}}(k_x)]\,[C - C_{\text{z2}}(k_x)]\,[C - C_{\text{z3}}(k_x)]}{C - C_{\text{p}}(k_x)} \tag{2.13}$$

In (2.12) and (2.13) subscripts $z$ and $p$ indicate zeros and poles of the rational functions. These quantities are expressed as third degree polynomials of $k_x$. In the frequency range of interest ($[10.55\,\text{GHz}, 10.75\,\text{GHz}]$), for the considered geometries $Y_{\text{MMTS}}$ is capacitive and $Y_{\text{RMTS}}$ is always inductive.

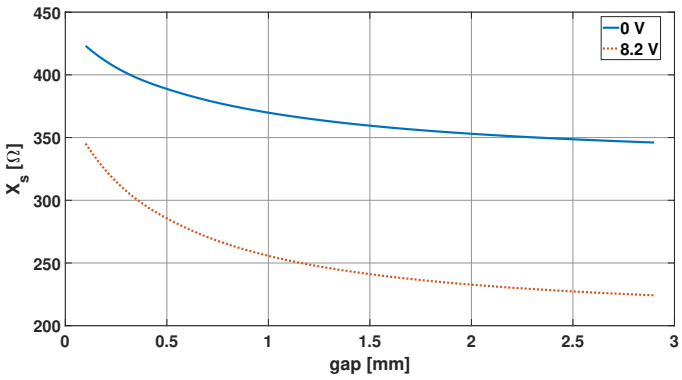


Figure 2.3: Surface reactance of the whole structure vs gap width in the array of strips, for two different values of the varactors' bias voltage.

Figure 2.3 shows how the surface reactance of the whole antenna is affected by a change in the varactors' bias voltage. The curve relating $X_{\text{s}}$ to the gap width is shifted when the bias voltage goes from 0 V to 8.2 V. This means that, for a fixed spatial modulation in the upper layer, the sinusoidal profile of the surface reactance (and its average value $X_{\text{s,ave}}$) seen by the traveling wave is dependent on the varactors' basing state. Since $X_{\text{s,ave}}$ is linked to the radiation angle through (2.2) and the period $p$ is fixed by the upper metasurface, beam steering occurs.

### 2.2.3 Implementation

A center-band frequency of 10.65 GHz is considered. A Rogers RT5880 ($\varepsilon_r = 2.2$, $\tan\delta = 0.0009$) 3.175 mm-thick substrate is placed between the upper radiating layer and the lower variable-impedance plane. The unit cell of the modulated metasurface is chosen to be about 1/10 of the wavelength, i.e. 3 mm. The air gap between the reconfigurable plane and the ground is set to 1.5 mm in order to allow enough space for the varactors.

The modulation period $p$ of the top impedance surface is computed from (2.2) setting a radiation angle of 20° for a 0 V bias voltage of the varactors, and this results in $p = 27$ mm. Since the unit cell of the modulated metasurface is 3 mm wide, the cosinusoidal variation of the reactance in one period is sampled in 9 points, i.e. with sufficient sampling. For the radiating part, 8 modulation periods are chosen for a total length of 216 mm; this is a good compromise between beam width and (leaky-wave) tapering, and at any rate yielding low $S_{21}$ towards the matched load.

The bias scheme of the varactors in the variable-impedance plane is depicted in Fig. 2.4, that shows an alternate-potential scheme. The necessary single DC bias is conveyed by two 0.15 mm-wide buses placed at the opposite sides of the metasurface; the RF reactance of the very thin (high-impedance) lines was considered enough to decouple RF and DC without the need of a filter, and that was confirmed by simulations.

The resulting complete structure of the designed antenna is shown in Fig. 2.5. The upper modulated metasurface is depicted in Fig. 2.5a, while Fig. 2.5c shows the lower reconfigurable impedance plane; the vertical stackup of the antenna can be seen in Fig. 2.5b. The overall thickness of the structure is less than $\lambda_0/6$ at the working frequency of 10.65 GHz, resulting in a very small form factor. It should be noted from Fig. 2.6 that the unit cell of the reconfigurable metasurface is twice as large as that of the upper layer, in order to reduce the total number of varactors needed in the structure, which amounts to 360.

The excitation is provided with a 50 Ω coaxial cable, that is matched to the antenna by a properly designed tapered section (Fig. 2.5a).

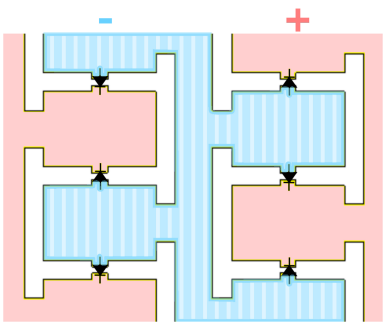


Figure 2.4: DC voltage distribution in the reconfigurable metasurface.

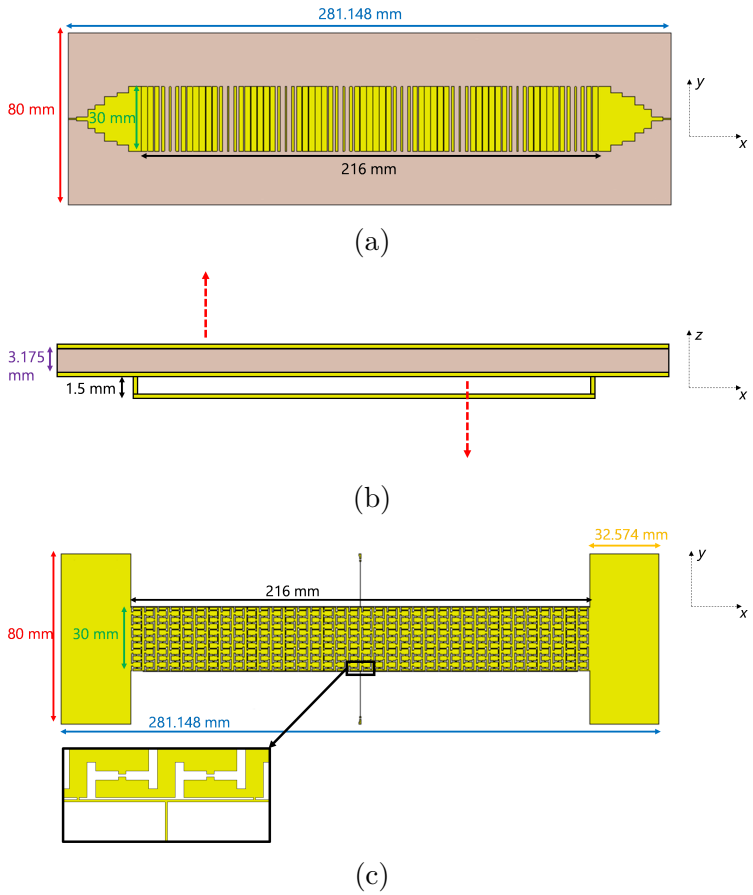


Figure 2.5: Complete model of the designed antenna. (a) Upper sinusoidally modulated reactance surface. (b) Lateral view of the antenna. (c) Reconfigurable plane; the inset shows one of the two DC buses.

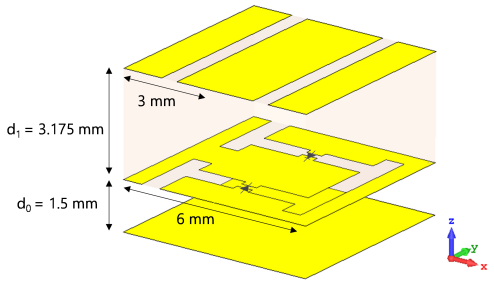


Figure 2.6: Unit cell of the fully-stacked structure.

## 2.3 Results

Full-wave simulations of the designed antenna have been performed with the commercial software CST Studio Suite [38]. The varactor diodes are used in a 0 V - 8.2 V biasing range and their capacitance goes from 0.233 pF to 0.0548 pF, while their equivalent resistance is 13.2 Ω, according to the manufacturer's datasheet [35]. The beam pointing angles obtained from these simulations at the working frequency of 10.65 GHz are listed in Table 2.1, showing excellent agreement with the main beam directions computed using the approximate model described in Sec. 2.2.

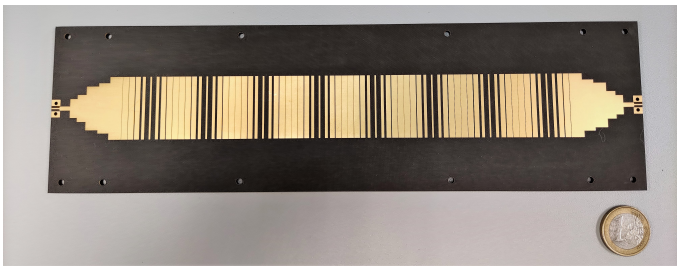

(a)

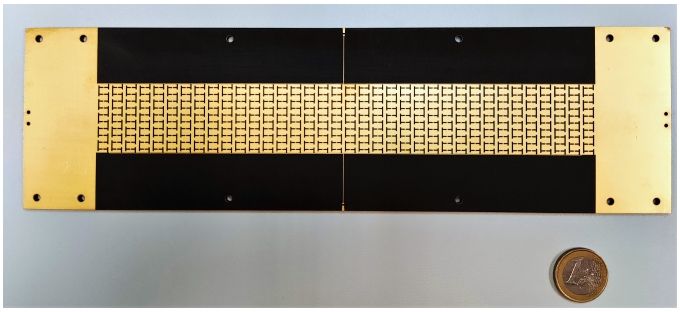

(b)

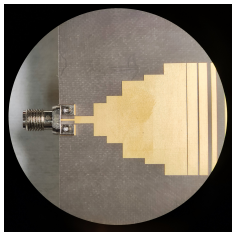

(c)

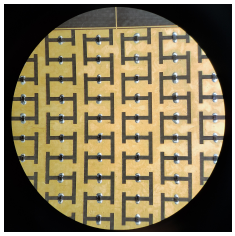

(d)

Figure 2.7: Fabricated antenna prototype. (a) Top modulated metasurface. (b) Reconfigurable impedance plane. (c) Coaxial cable and matched tapered input section at the left end of the upper metasurface (same tapered section is present at the opposite end). (d) Zoom showing the soldered varactors in the lower reconfigurable metasurface.

Table 2.1: Calculated, Simulated and Measured Radiation Angles at 10.65 GHz.

| **Voltage [V]** | **Calculated** | **Simulated** | **Measured** |
|---|---|---|---|
| 0 | 22.7° | 20° | 19.5° |
| 8.2 | 11.9° | 13° | 12.5° |

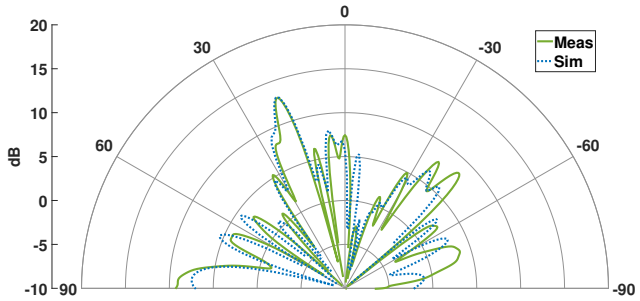


(a) 0 V

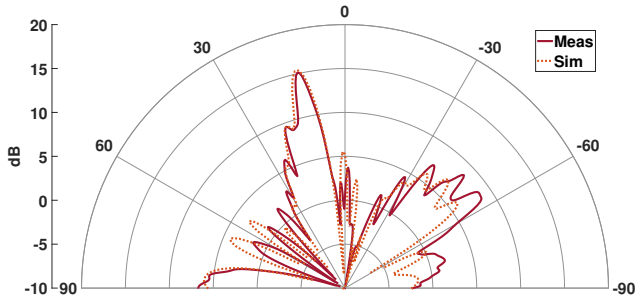


(b) 8.2 V

Figure 2.8: Measured and simulated radiation pattern in the E-plane at 10.65 GHz for different values of bias voltage.

A prototype was fabricated and tested (Fig. 2.7). The modulated metasurface and the reconfigurable plane are pictured in Figs. 2.7a and 2.7b, while Figs. 2.7c and 2.7d show the tapered feeding section on the upper layer and the varactor diodes soldered in the lower metasurface, respectively. Radiation measurements have been performed in a NF-FF spherical range; the full radiation pattern has been obtained, allowing evaluation of directivity and radiation efficiency.

Measured far-field patterns at 10.65 GHz for different bias voltages are shown in Fig. 2.8, together with the simulation results, which are in excellent agreement.

The antenna gain bandwidth is 200 MHz around the working frequency of 10.65 GHz; the impedance bandwidth is larger than the gain one. The scattering parameters $S_{11}$ and $S_{21}$ of the fabricated prototype are shown in Fig. 2.9: $S_{11}$ is always below −10 dB in the working band for all varactors' bias voltages, while $S_{21}$ remains below −20 dB, which is very important for the efficiency of a traveling-wave antenna.

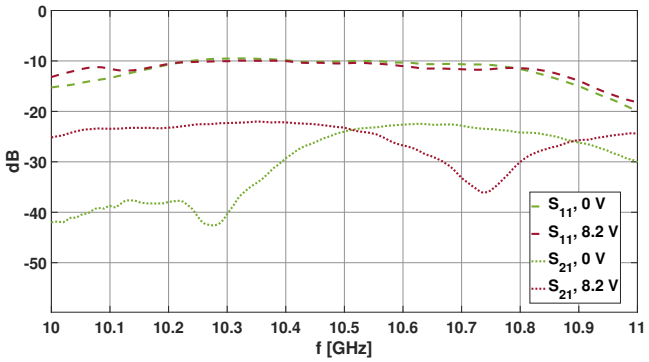


Figure 2.9: Measured $S_{11}$ and $S_{21}$ for two different values of bias voltage.

In the considered frequency range, the measured gain spans from 11.6 dB to 13.4 dB with varying bias voltage, while the radiation efficiency is between 67% and 76%. The measured aperture efficiency goes from 20% to 32%.

The realized gain estimated from full-wave simulations of the complete antenna spans from 11.4 dB to 14.2 dB, and it's therefore very similar to the measured one. Simulations show that the resistive component in the lumped elements causes the biggest loss in the total power balance, with this loss being greater than the conductor and dielectric losses by one order of magnitude. This means that assuming a constant resistance value of 13.2 Ω for the RC series equivalent model of the varactors, despite leading to an under- and over-estimation of the gain at 0 V and 8.2 V, respectively, still provides sufficiently accurate predictions on the overall performance of the fabricated prototype.

In Fig. 2.8 a side-lobe is noticeable in the backward radiation direction; this lobe can be ascribed to radiation of the $n = -2$ harmonic, which falls within the fast wave region at the working frequency [4]. These results are consistent with what can be predicted using (2.2), i.e. the $n = -2$ harmonic radiating at about $-41°$ and $-57°$ for a bias voltage equal to 0 V and 8.2 V respectively. The radiation pattern also presents an irregular shape and high side-lobes; this can be ascribed to the anisotropy of the impedance planes, in particular of the lower reconfigurable metasurface. In fact, its unit cell geometry and the placement of the varactor diodes inside it are such that a change in the bias voltage alters not only the component of the sheet impedance in the direction of wave propagation, but also the transverse one. This may cause disturbances in the wave propagation.

## 2.4 Discussion

In Table 2.2, the performances of the antenna described in this Chapter are compared to those of other solutions found in literature. In it, "efficiency" stands for radiation efficiency.

Table 2.2: Comparison with other LWAs found in literature.

| **Reference** | **Frequency [GHz]** | **Scanning Range** | **Antenna Length** | **Thickness** | **Efficiency** | **Gain [dB]** |
|---|---|---|---|---|---|---|
| [23] | 5.6 | 21° | $5\lambda_0$ | $3\lambda_0/4$ | 60% - 75% | 5 - 13 |
| [27] Band 2 | 5.75 | 22° | $7.15\lambda_0$ | $\lambda_0/17$ | 40% - 50% | 9.5 - 12 |
| [15] | 9.3 | 43° | $13\lambda_0$ | $\lambda_0/3$ | 38% - 46% | 8 - 11.8 |
| This work | 10.65 | 7° | $7.7\lambda_0$ | $\lambda_0/6$ | 67% - 76% | 11.6 - 13.4 |

Radiation efficiency and gain values are comparable to the ones reported in the other works (above the average). The comparison is conservative because all reported references work at a lower frequency, which inherently entails lower losses. Moreover, the fact that losses in the varactors constitute the majority of power dissipation suggests that reducing the number of active components could significantly increase the antenna gain. Therefore, a robustness analysis could be performed in order to determine the minimum number of varactors (and their positions) in the texture of the reconfigurable metasurface, that would allow for the same tunability of the impedance layer while avoiding to place two active elements in each unit cell. Overall, the small form factor, simple biasing and high efficiency make the proposed architecture interesting for several low-profile applications.

The angular scanning range achieved with this first prototype is, on the other hand, limited: improvement of this is thus important and the subject of current work. Here some of the reasons of this limitation are listed and ways to improve it are proposed.

A possible degree of improvement is represented by the choice of the dielectric substrate and its thickness, especially for the side lobes. In particular, a higher relative permittivity results in a wider range of surface reactance values $X_s$, which allows for a larger modulation factor $M$ and, consequently, a higher leakage constant [4]. This in turn translates into the reduction of side-lobes.

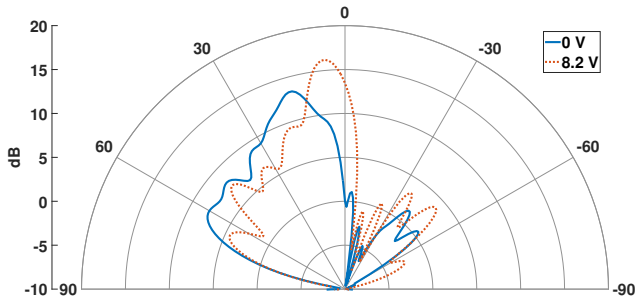


Figure 2.10: Simulated radiation pattern at 10.75 GHz for different bias voltages for an alternative design with Rogers RO3006 substrate ($\varepsilon_r = 6.5$).

Figure 2.10 shows the simulated radiation pattern at 10.75 GHz for an alternative design of the proposed antenna featuring a Rogers RO3006 substrate ($\varepsilon_r = 6.5$) of thickness equal to 2.56 mm: the radiation angle steers from 15° to 5° when the bias voltage goes from 0 V to 8.2 V. In this case, no other harmonic beside the $n = -1$ radiates, and the very small backward-directed side-lobes are due to the spurious radiation of a second, higher-order TM mode. Directivity values are the same as in the previous configuration. A further reduction of sidelobes could be obtained by tapering the modulation index $M$ along the length of the antenna [39] - which was not pursued here.

Another margin of improvement involves the geometry of the reconfigurable metasurface's unit cell. The tunable unit cell used in this first prototype was inspired from the literature and had a different original use [34]; a new geometry could be devised to obtain a wider impedance range for the same diodes.

Moreover, the design presented in this Chapter is based on the combination of a capacitive impedance (top) and an inductive one (bottom) and the propagation of the TM mode. However, different combinations of impedances can be employed (e.g., capacitive-capacitive) that may increase the scanning range if properly designed, especially if a dielectric material with higher electric permittivity is used. In particular, analyses carried out with the approximate analytical model show that use of the TE mode (instead of the TM) yields a much larger steering range. This possibility is currently being studied and will be the subject of future work (excitation of the TE mode is less natural than the TM).

## 2.5 Conclusions

In this Chapter, a novel beam steering configuration with varactor diodes, a single voltage bias, and no vias has been demonstrated. The small form factor, simple

biasing, and high efficiency make the proposed architecture interesting for low-profile applications. The angular scanning range achieved with this first prototype is limited, but several ways to improve it were discussed.

# Chapter 3

# Generalized Deterministic Automated Design of Metasurface Antennas with 3-D Feeding Structures

This Chapter expands the published article [40].

We present an automatic, deterministic procedure to fully design an isotropic metasurface antenna, self-consistently including the metallic feeding structure. The impedance pattern has full spatial variability in two dimensions, to allow designs otherwise difficult. The design is based on the integral-equation formulation with a current-only approach, in which the surface impedance profile is derived only after the optimal current is found; this allows to avoid the solution of the forward problem at all steps of the algorithm, with a drastic reduction of computational resources; it does not require any assumption on the impedance profile. We also show how a 3-D feed can be accounted for in a hybrid scheme partially employing commercial 3-D simulation software. Application examples address center-fed circular metasurface antennas, in which the feed is not connected to the metasurface, and rectangular "strip-like" leaky-wave antennas where the metasurface is electrically connected to the feeding surface. In all cases, the design is carried out up to the final layout, and the full antenna is simulated to verify the design.

## 3.1 Introduction

The design of metasurface (MTS) antennas almost always employs the so-called *Impedance Boundary Condition* (IBC) for approximating the local electromagnetic behavior of the surface through a single parameter, the surface impedance; the design then entails defining the spatial distribution of this parameter. Following

this, the impedance is locally implemented by means of properly-shaped unit cells. This two-step, multi-scale approach allows to address the design of electrically large antennas, keeping the overall complexity under control.

Initially, methods for the design of metasurface antennas were targeted to circular domains and considered only sinusoidally modulated profiles [41, 42]. These methods, based on analytical considerations, demonstrated the practical feasibility of designing large metasurface antennas, and paved the way for more general and sophisticated approaches. More recently, fully numerical schemes have enabled the analysis and design of shaped MTS antennas on circular domains and other boundaries [43, 44, 45, 46, 6], with various degrees of generality in the impedance profile.

The direct way to numerically address the design issue is an optimization of the impedance profile [47]; however, IBC synthesis methods have emerged that seek for the optimization of the (equivalent) *current* on the metasurface [48, 49, 8, 7, 50, 51, 52, 53, 54] as an alternative to those directly seeking an impedance profile. The former methods will be called "current-only" here, and the latter impedance-based. There are also methods that optimize the induced current and the impedance simultaneously [55], or the amplitude of explicitly-defined aperture fields [56, 57, 58]. Current-only methods enjoy a significantly lower numerical complexity than the impedance-based, and are typically deterministic; in them, the sought-for impedance profile is obtained from the optimized current at the end of the process.

In particular, the current-only method presented in [6] is deterministic and can be proven to be of minimal complexity per-iteration. It allows arbitrary spatial variation of the impedance, without a-priori knowledge on the targeted IBC profile (as opposed to, e.g., methods tailored to sinusoidally modulated MTS antennas, which require specific parameterizations [59, 46, 45]). The inputs are the geometry of the IBC surface, the definition of the feed, and the radiation pattern mask constraints.

The design of the feeding structure is usually carried out independently from that of the metasurface, with the main objective of maximizing the power excited in the appropriate surface wave [41, 60]. Its effect is then included in the design by means of the incident field, i.e., the field radiated by the feed in isolation; this procedure does not account for the feed–metasurface interaction. A very recent contribution [46] has addressed the full wave feeder modeling in the impedance-based optimization (as opposed to the present interest in current-based); it employs a physics-based specialized parametric impedance profile (as opposed to the present search for a general impedance profile). As demonstrated there, a proper, self-consistent modelling of the feeding structure is important for a correct estimation of the (peak) gain of the metasurface antenna.

In this work, we generalize the method presented in [6] to encompass a specified feeding structure in the current-only inverse design of the metasurface antenna.

This results in the fully self-consistent design of the entire metasurface antenna, and the ability to find the necessary impedance profile without a priori guesses. The synthesis algorithm presented in this Chapter is restricted to isotropic metasurfaces; an extension to the design of anisotropic antennas is currently being developed. We observe that the proposed method is more general than our present emphasis on feeding structures. In fact, the PEC regions can have any function, not just feeding; nevertheless, this constitutes the most relevant case in practical designs. We address center-fed metasurface antennas, but also edge-fed "strip-like" leaky-wave antennas, in which the feed is electrically connected to the IBC part; this last case is hardly addressable without the present self-consistent treatment. We will also demonstrate the importance of leaving full spatial variability in the sought-for impedance pattern when addressing design instances where a guess of the solution is not readily available.

To the best of our knowledge, this is the first time that the feed structure is addressed into a current-only design method, with full spatial variability of the impedance pattern; also, this is the first time that a feeding structure electrically connected to the metasurface is considered.

Preliminary results relative to the present topic have been submitted as a conference paper [61]; this is the first account of the method, of its theory and implementation.

This Chapter is organized as follows. In Section 3.2, the mathematical formulation of the electromagnetic problem is outlined. Section 3.3 presents the details of the proposed self-consistent current-based design algorithm, with focus on the types of feed that can be handled. In Section 3.4, application examples are provided to validate the approach. In particular, two classes of antennas will be considered: a circular antenna excited by a coaxial aperture in the ground plane, and a rectangular, "strip-like" antenna fed at one edge by a coaxial-to-microstrip transition. For each case, a comparison of the performance with and without self-consistent modelling of the feed is given, in order to highlight its importance in practical scenarios. Finally, conclusions are drawn in Section 3.5.

## 3.2 Forward Problem

In the analysis of metasurface antennas, the geometry can be divided into two distinct regions (Fig. 3.1): the surface $\mathcal{S}_{\text{PEC}}$ which contains all metallic portions (e.g., the feeding structure), and the surface $\mathcal{S}_{\text{IBC}}$ on which the *Impedance Boundary Condition* (IBC) applies. This condition links the tangential electric field to the jump of the tangential magnetic field through the surface impedance tensor $\overline{\overline{\boldsymbol{Z}}}$ [62]:

$$\boldsymbol{E}_{\tan} = \overline{\overline{\boldsymbol{Z}}} \cdot \left[ \hat{\boldsymbol{n}} \times (\boldsymbol{H}^{+} - \boldsymbol{H}^{-}) \right]. \tag{3.1}$$

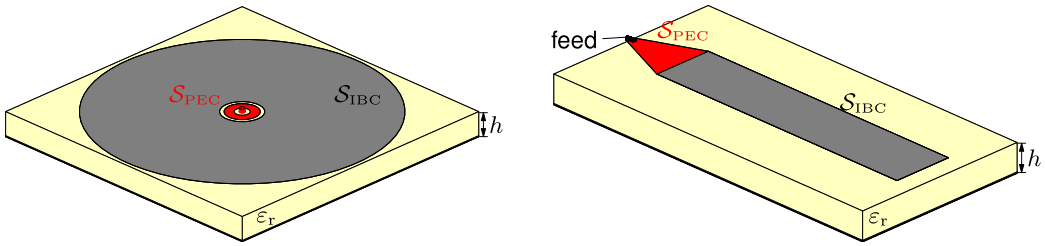


(a) (b)

Figure 3.1: Examples of two geometries of metasurface antennas: (a) center-fed circular antenna, (b) edge-fed "strip-like" antenna.

In this work, as in [6], we will consider only a *scalar impedance*, i.e., $\overline{\overline{\boldsymbol{Z}}} = Z\,\overline{\overline{\boldsymbol{I}}}$ (where $\overline{\overline{\boldsymbol{I}}}$ is the identity tensor).

By introducing the equivalent current density

$$\boldsymbol{J} = \hat{\boldsymbol{n}} \times (\boldsymbol{H}^{+} - \boldsymbol{H}^{-}), \tag{3.2}$$

the electromagnetic problem is formulated as an *Electric Field Integral Equation*:

$$\left[\boldsymbol{E}_{\text{inc}}(\boldsymbol{r}) + \mathcal{L}\boldsymbol{J}(\boldsymbol{r})\right]_{\text{tan}} = \begin{cases} Z(\boldsymbol{r})\,\boldsymbol{J}(\boldsymbol{r}), & \boldsymbol{r} \in \mathcal{S}_{\text{IBC}} \\ \boldsymbol{0}, & \boldsymbol{r} \in \mathcal{S}_{\text{PEC}} \end{cases} \tag{3.3}$$

where $\boldsymbol{E}_{\text{inc}}$ is the field radiated by the (independent) sources in the absence of the metasurface and all metallic (PEC) parts, and $\mathcal{L}$ is the *Electric Field Integral Operator* (EFIO) defined as

$$\mathcal{L}\boldsymbol{J}(\boldsymbol{r}) = \iint \overline{\overline{\boldsymbol{G}}}^{\text{EJ}}(\boldsymbol{r}, \boldsymbol{r}') \cdot \boldsymbol{J}(\boldsymbol{r}')\, \mathrm{d}S(\boldsymbol{r}'), \tag{3.4}$$

where $\overline{\overline{\boldsymbol{G}}}^{\text{EJ}}$ is the multilayer dyadic Green's function for the (grounded or ungrounded) substrate [63]. In the following, we indicate with $\boldsymbol{J}_{\text{ibc}}$ and $\boldsymbol{J}_{\text{pec}}$ the current density $\boldsymbol{J}$ on the two regions $\mathcal{S}_{\text{IBC}}$ and $\mathcal{S}_{\text{PEC}}$, respectively.

For the numerical discretization we adopt the usual Method of Moments approach with Galerkin testing: we consider a mesh given by a triangular tessellation of the whole antenna surface and we approximate the sought current $\boldsymbol{J}(\boldsymbol{r})$ as a linear combination of Rao-Wilton-Glisson (RWG) basis functions $\boldsymbol{\Lambda}_n$ [64] defined on the $N$ internal mesh edges,

$$\boldsymbol{J}(\boldsymbol{r}) = \sum_{n=1}^{N} I_n\, \boldsymbol{\Lambda}_n(\boldsymbol{r}). \tag{3.5}$$

In the following, we will denote by $N$ the total number of RWG functions (i.e., on both IBC and PEC regions), and by $N_{\text{ibc}}$ and $N_{\text{pec}}$ the number of functions with

support on $\mathcal{S}_{\text{IBC}}$ and $\mathcal{S}_{\text{PEC}}$, respectively. Thus, in its most general form, the forward (analysis) problem reduces to the linear system

$$\mathsf{V}_{\text{inc}} + \mathsf{L}\mathsf{I} = \mathsf{Z}\mathsf{I}, \tag{3.6}$$

where the array $\mathsf{I}$ collects the RWG basis coefficients $I_n$ and the remaining quantities are defined as

$$(\mathsf{L})_{mn} = \langle\, \boldsymbol{\Lambda}_m \,, \mathcal{L}\boldsymbol{\Lambda}_n \,\rangle, \tag{3.7}$$
$$(\mathsf{Z})_{mn} = \langle\, \boldsymbol{\Lambda}_m \,, Z\boldsymbol{\Lambda}_n \,\rangle, \tag{3.8}$$
$$(\mathsf{V}_{\text{inc}})_m = \langle\, \boldsymbol{\Lambda}_m \,, \boldsymbol{E}_{\text{inc}} \,\rangle, \tag{3.9}$$

where $\langle\, \boldsymbol{a} \,, \boldsymbol{b} \,\rangle = \int \boldsymbol{a} \cdot \boldsymbol{b}\, \mathrm{d}S$ is a symmetric bilinear form. It follows from (3.3) that, for test functions that lie on $\mathcal{S}_{\text{PEC}}$, $Z = 0$ and the corresponding matrix entries (3.8) are equal to zero. The interaction between the IBC and PEC currents is better highlighted by recasting (3.6) as

$$\begin{bmatrix} \mathsf{V}^{\text{inc}}_{\text{ibc}} \\ \mathsf{V}^{\text{inc}}_{\text{pec}} \end{bmatrix} + \begin{bmatrix} \mathsf{L}_{\text{ibc}} & \mathsf{L}^{\mathsf{T}}_{\text{cpl}} \\ \mathsf{L}_{\text{cpl}} & \mathsf{L}_{\text{pec}} \end{bmatrix} \begin{bmatrix} \mathsf{I}_{\text{ibc}} \\ \mathsf{I}_{\text{pec}} \end{bmatrix} = \begin{bmatrix} \mathsf{Z}_{\text{ibc}} & \mathbf{0} \\ \mathbf{0} & \mathbf{0} \end{bmatrix} \begin{bmatrix} \mathsf{I}_{\text{ibc}} \\ \mathsf{I}_{\text{pec}} \end{bmatrix}, \tag{3.10}$$

where:

- $\mathsf{I}_{\text{ibc}}$ and $\mathsf{I}_{\text{pec}}$ collect the RWG coefficients of $\boldsymbol{J}_{\text{ibc}}$ and $\boldsymbol{J}_{\text{pec}}$, respectively,
- $\mathsf{V}^{\text{inc}}_{\text{ibc}}$ and $\mathsf{V}^{\text{inc}}_{\text{pec}}$ gather the coefficients of the projected incident field on the two regions,
- the two square matrices $\mathsf{L}_{\text{ibc}}$ $(N_{\text{ibc}} \times N_{\text{ibc}})$ and $\mathsf{L}_{\text{pec}}$ $(N_{\text{pec}} \times N_{\text{pec}})$ represent the self-interaction of the two regions,
- the rectangular matrix $\mathsf{L}_{\text{cpl}}$ $(N_{\text{pec}} \times N_{\text{ibc}})$ identifies the coupling between the IBC and PEC regions.

The far-field can be computed from the current via the *radiation operator* $\mathcal{R}$:

$$\mathcal{R}\boldsymbol{J}(\hat{\boldsymbol{r}}) = \frac{k_0}{2\pi \mathrm{j}} \iint \overline{\overline{\boldsymbol{G}}}^{\text{ff}}(\hat{\boldsymbol{r}}, \boldsymbol{r}') \cdot \boldsymbol{J}(\boldsymbol{r}')\, \mathrm{d}S(\boldsymbol{r}') \tag{3.11}$$

where $\overline{\overline{\boldsymbol{G}}}^{\text{ff}}(\hat{\boldsymbol{r}}, \boldsymbol{r}')$ is the multilayer far-field tensor [65] and the unit vector $\hat{\boldsymbol{r}}(\theta, \varphi)$ identifies the direction of radiation in spherical coordinates.

## 3.3 Self-Consistent Current-Only Inverse Design with Specified Feed

### 3.3.1 Requirements

The inputs to the design process are the specification of the substrate, the definition of the surface geometry, and of the source, i.e., the specification of the incident field. The definition of the geometry also involves the specification of the PEC structures, that may be planar or 3-D (see Fig. 3.1).

The goal of the design process is an impedance profile that, for the given incident field,

- radiates a field pattern obeying the specifications (pattern masks), and
- is physically realizable.

To obtain a physically realizable impedance we must enforce that the metasurface be locally *passive* and *lossless*, and that the synthesizable reactance values fall within the technologically feasible range. It is also possible to model a realistic, lossy impedance surface by taking into account conductor and dielectric losses; accurate material loss evaluation was not pursued in this thesis, but it can be easily featured in the proposed synthesis algorithm, in a way that will be briefly discussed in Section 3.3.5.

Far-field specifications are of the *mask type*, i.e., defined via *inequalities* for each considered far-field direction. These constraints must typically be expressed in terms of directivity or gain.

### 3.3.2 Self-consistency

The current-based design method presented in [6] formulates the problem in such a way that it involves *only* the equivalent current on the IBC—not the impedance. This avoids the solution of the forward problem (3.6) at each step; instead, only the computation of the on-surface and radiated fields is required, with complexity $O(N \log N)$.

The self-consistent inclusion of the PEC structure (e.g., the feed) implies that the design algorithm must look for a *pair* of currents $(\boldsymbol{J}_{\text{ibc}}, \boldsymbol{J}_{\text{pec}})$ such that:

- *together* they satisfy radiated field specifications;
- on the IBC region, $\boldsymbol{J}_{\text{ibc}}$ satisfies IBC constraints (passivity, absence of losses, feasibility range);
- on the PEC region, $\boldsymbol{J}_{\text{pec}}$ satisfies the PEC boundary condition.

Note that the two parts of the current self-consistently interact with one another through the IBC-PEC coupling term $\mathsf{L}_{\text{cpl}}$ in (3.10).

### 3.3.3 Current-only optimization framework for Metasurface Antenna design

Here, we highlight only the most relevant features of the current-only design method in [6], as necessary to understand the proposed generalized design approach.

The total cost function that the algorithm aims to minimize can be expressed as

$$f = f_{\text{rad}} + f_{\text{ibc}} + f_{\text{pec}}, \tag{3.12}$$

where each term is a functional, i.e., a scalar non-negative function, of the surface current only. The model descriptors to be optimized are the current coefficients.

Here, $f_{\text{rad}}$ accounts for the radiated field requirements, and $f_{\text{ibc}}$ encompasses the realizability constraints to be enforced on the IBC region (passivity, losslessness and feasibility range). The term $f_{\text{pec}}$ is added in order to enforce the PEC condition on the related surface. The radiated field and impedance terms are briefly discussed in App. A.1 and A.2, respectively, while the term associated to the PEC condition will be introduced in detail in Section 3.3.6. The considered minimization problem is intrinsically non-convex (due to the passivity constraint); to limit the difficulties of non-convexity all functionals are expressed as fourth-degree multivariate polynomials in the current coefficients [7].

For the minimization of the cost function a *non-linear conjugate gradient* algorithm [66, p. 121] is employed. Since this thesis does not focus on optimization techniques, the choice of the non-linear conjugate gradient algorithm as the optimization method to minimize the cost function (3.12) is motivated by ease of implementation and the intrinsic advantage in maintaining continuity with the automated synthesis method firstly described in [6]. In fact, other optimization methods, such as global optimizers integrated with machine-learning techniques, could be applied to the synthesis of metasurface antennas [67]; rigorous tests to assess the effectiveness and the efficiency of different optimization techniques must be carried out in order to select the most performing algorithm for the problem at hand: this represents a natural step forward in the development of the proposed automated method and will be addressed in future works.

Given the large size of the problem, the numerical cost of computing the functional and its gradient at each iteration is an issue of paramount importance; hence, all operations are cast in such a way to be amenable to the use of fast factorizations, with $O(N)$ memory requirements and $O(N \log N)$ complexity per iteration. Therefore, the entire design process has a complexity of $O(N_{\text{iter}}^{\text{cur}} N \log N)$, where $N_{\text{iter}}^{\text{cur}}$ is the total number of iterations needed by the *current-only* algorithm to obtain the result. On the contrary, a classical *impedance-based* design requires, at each iteration, the solution of the linear system representing the electromagnetic problem for a given impedance distribution. In the most favorable scenario where fast iterative algorithms are used, this step has a complexity of at least $O(N_{\text{sol}} N \log N)$ per iteration (where $N_{\text{sol}}$ is the number of iterations needed by the iterative solver),

resulting in a global complexity $O(N_{\text{iter}}^{\text{imp}} N_{\text{sol}} N \log N)$ for the full design. In the latter case, the number of iterations $N_{\text{iter}}^{\text{imp}}$ is typically dependent on the global search algorithm employed for the optimization, and grows roughly exponentially with the number of parameters used to represent the impedance profile. This means that, for the optimization to be practically feasible, the number of parameters should be small (typically less than 10), forcing the designer to choose a priori the shape of the impedance profile (e.g., spiral modulation) based on the knowledge of the required radiation pattern. This is not always possible, as in the case of complicated shaped-beam patterns, limiting the generality of the *impedance-based* design process. Overall, a *current-only* approach offers more generality and a better scaling of the numerical complexity with an increasing number of degrees of freedom (and a larger antenna size, as a consequence).

### 3.3.4 Enforcement of radiation constraints

The radiated field is required to comply with upper and lower bounds for both the co- and cross-polarization components in the main beam,

$$M_{\text{L}}^{\text{co}} \leq F^{\text{co}} \leq M_{\text{U}}^{\text{co}} \tag{3.13}$$

$$F^{\text{cx}} \leq M^{\text{cx}} \tag{3.14}$$

and for the total amplitude in the side-lobe region,

$$F^{\text{tot}} \leq M^{\text{tot}}. \tag{3.15}$$

where $F$ is the squared amplitude of the electric field component radiated in the far-field in a given direction. The masks are defined with respect to the reference level $L_0$, which can be fixed or given in terms of the radiation pattern (e.g., the amplitude in the direction of maximum radiation). The radiation requirements are summarized graphically in Fig. 3.2. By choosing a suitable value of $L_0$ which corresponds to the desired gain, the algorithm maximizes the radiated power for a given (input) power of the incident field.

Indicating with $P_{\text{inc}}$ the power associated to the (given) incident field $\boldsymbol{E}_{\text{inc}}$, the radiation pattern can be expressed in terms of the *realized gain* [68],

$$G_{\text{r}}(\hat{\boldsymbol{r}}) = \frac{|\boldsymbol{E}(\hat{\boldsymbol{r}})|^2/\eta_0}{P_{\text{inc}}/4\pi} \tag{3.16}$$

where $\eta_0$ is the free-space impedance, and $\boldsymbol{E}(\hat{\boldsymbol{r}})$ is the far-field radiated in a given direction. By invoking Poynting's theorem, and neglecting losses in the conductors and the substrate, one arrives at the following power balance equation:

$$P_{\text{rad}} + P_{\text{refl}} + P_{\text{rim}} = P_{\text{inc}} \tag{3.17}$$

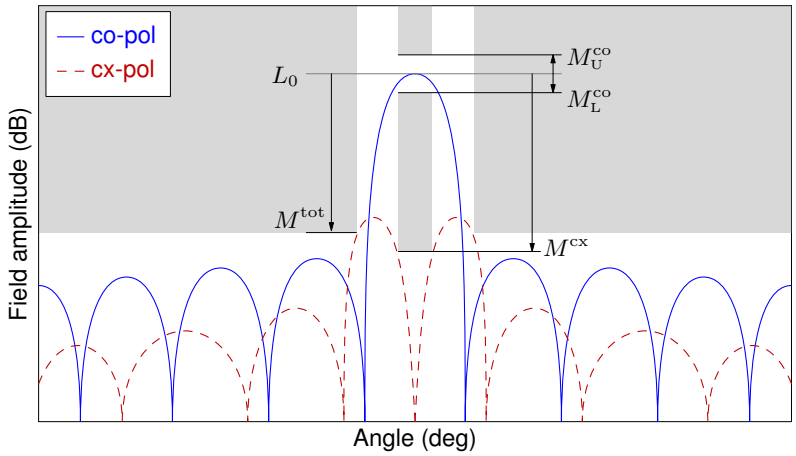


Figure 3.2: Example of far-field specifications: main lobe co-pol upper mask $M_{\mathrm{U}}^{\mathrm{co}}$ and lower mask $M_{\mathrm{L}}^{\mathrm{co}}$, cross-pol mask $M^{\mathrm{cx}}$ and side lobes mask $M^{\mathrm{tot}}$. All masks are defined relative to the reference level $L_0$, as indicated by the arrows.

where $P_{\mathrm{inc}}$ is the incident power (associated to the incident field), $P_{\mathrm{rad}}$ is the power radiated in far field, $P_{\mathrm{refl}}$ is the power reflected toward the source, and $P_{\mathrm{rim}}$ is the residual surface wave power that is diffracted by the outer rim of the antenna (not modelled when considering an infinite dielectric). Therefore, maximizing the radiated power for a constant incident power (right-hand side of (3.17)) intrinsically minimizes the input reflection coefficient and the spurious contribution from the rim diffraction.

With these considerations, it is evident that the ability to include a real model of the feeding structure is crucial for the robustness of the optimization process.

### 3.3.5 Enforcement of IBC constraints

The requirements for passivity and losslessness, the bounds on the synthesizable reactance values, and the scalarity condition can all be expressed in terms of fields as follows [6]:

$$\mathrm{Re}\left(\boldsymbol{E}_{\tan}\cdot\boldsymbol{J}^{*}\right)=0, \tag{3.18}$$

$$X_{\mathrm{L}}\left|\boldsymbol{J}\right|^{2}\leq\mathrm{Im}\left(\boldsymbol{E}_{\tan}\cdot\boldsymbol{J}^{*}\right)\leq X_{\mathrm{U}}\left|\boldsymbol{J}\right|^{2}, \tag{3.19}$$

$$\left|\boldsymbol{E}_{\tan}\times\boldsymbol{J}^{*}\right|=0. \tag{3.20}$$

All the above conditions must hold locally for all $\boldsymbol{r}\in\mathcal{S}_{\mathrm{IBC}}$; in accordance with our cell-based spatial discretization scheme, we will enforce these conditions in the average sense over each mesh cell. The formulation of these functionals, including their explicit expression in terms of matrix operations, are reported in App. A.2.

Once the optimal current has been obtained through the optimization process, the impedance profile can be derived via (3.6) by expressing the unknown

impedance profile as a linear combination of (scalar) basis functions, and solving the resulting linear system for the unknown impedance coefficients.

In the present work, we have employed basis functions which result in a piecewise constant impedance profile over the triangles of the mesh. This particular case, detailed in App. B, admits a closed-form solution for the impedance $Z_i$ over the $i$-th cell:

$$Z_i = \frac{\iint_{\mathcal{S}_i} \boldsymbol{E}_{\tan} \cdot \boldsymbol{J}^* \, \mathrm{d}S}{\iint_{\mathcal{S}_i} |\boldsymbol{J}|^2 \, \mathrm{d}S}. \tag{3.21}$$

### Modeling of lossy IBC

The proposed synthesis method can be easily modified to take into account conductor and dielectric losses, that, together with feed-antenna mismatch, negatively impact the realized gain and the efficiency of the metasurface antenna. While this additional degree of accuracy was not explored in the design cases illustrated in this Chapter, it can be achieved through two fundamental steps:

- incorporation of the dielectric losses within the multilayer Green's function, and
- modification of the passivity and losslessness condition (3.18) to take into account conductor losses.

While the former step is straightforward, the latter can be formulated in such a way that the resulting functional is still a fourth-degree polynomial in the current coefficients, thus maintaining the related advantages in terms of line search procedure [69]. This can be obtained by expressing the surface resistance $R$ as a function of the reactance $X$, similarly to what was done in [57], and approximating their relation with a first-degree polynomial. In case of sub-wavelength square copper patches printed on a grounded lossy dielectric substrate, such as the ones that will be used to physically implement the designed metasurfaces in Section 3.4, normal-incidence scattering simulations can be performed to retrieve the complex surface impedance $Z = R + \mathrm{j}X$ as a function of the patch width, and the relation between $R$ and $X$ [57]. Figure 3.3 shows the real and imaginary part of the sheet impedance in case of square copper patches of periodicity 2 mm printed on a lossy RO3006 substrate, at the frequency of 10 GHz; the lossless version of these unit cells will be employed, for example, in the designs of Section 3.4.4.

The relation $R = R(X)$ from Fig. 3.3 can be reasonably approximated as a first-degree polynomial

$$R(X) = c_1 X + c_0, \tag{3.22}$$

with $c_1, c_0 \in \mathbb{R}$, $c_1 < 0$ and $c_0 > 0$. This means that $R_{\mathrm{U}} = R(X_{\mathrm{L}})$ and $R_{\mathrm{L}} = R(X_{\mathrm{U}})$.

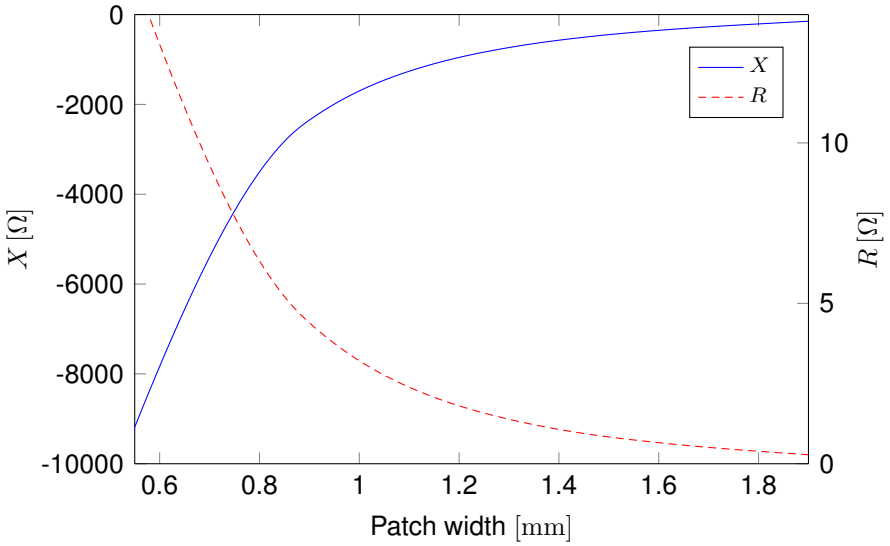


Figure 3.3: Mapping between patch width and complex impedance for copper patches printed on a lossy RO3006 substrate.

Considering a lossy metasurface, one now has that

$$\mathrm{Re}\left(\boldsymbol{E}_{\tan}\cdot\boldsymbol{J}^{*}\right)=R\left|\boldsymbol{J}\right|^{2}=c_{1}X\left|\boldsymbol{J}\right|^{2}+c_{0}\left|\boldsymbol{J}\right|^{2}, \tag{3.23}$$

$$\mathrm{Im}\left(\boldsymbol{E}_{\tan}\cdot\boldsymbol{J}^{*}\right)=X\left|\boldsymbol{J}\right|^{2}. \tag{3.24}$$

Therefore, the condition of passivity and losslessness (3.18) can no longer be enforced, but it must be substituted with a constraint that ensures the realizability of the synthesizable lossy impedance; for the considered geometry and substrate, this translates into enforcing (3.22) together with (3.19) and (3.20). The new constraint can be expressed as

$$\mathrm{Re}\left(\boldsymbol{E}_{\tan}\cdot\boldsymbol{J}^{*}\right)-c_{1}\,\mathrm{Im}\left(\boldsymbol{E}_{\tan}\cdot\boldsymbol{J}^{*}\right)-c_{0}\left|\boldsymbol{J}\right|^{2}=0, \tag{3.25}$$

while the related functional is the fourth-degree polynomial

$$\rho^{\mathrm{loss}}=(P-c_{1}Q-c_{0}\mathcal{J})^{2}, \tag{3.26}$$

where the quantities $P$, $Q$ and $\mathcal{J}$ are those defined in App. A.2.

### 3.3.6 Enforcement of PEC condition

We now discuss how to enforce the PEC condition coherently with the design algorithm presented in Section 3.3.3. The condition of *Perfect Electric Conductor*,

$$\boldsymbol{E}_{\tan}(\boldsymbol{r})=\boldsymbol{0}, \tag{3.27}$$

needs to be enforced everywhere on PEC surfaces, and this has to be done by a *functional*, i.e., a mapping from the $N$ complex current coefficients into a *single* real non-negative number. Opposed to this, we observe that Galerkin's testing of (3.27), corresponding to the PEC part of (3.3), leads to a *vector* of $N_{\text{pec}}$ complex numbers.

The construction of the necessary functional can be done in two different ways, as detailed below. This functional will be denoted by $\rho^{\text{pec}}(\mathsf{I})$; it is related to the term $f_{\text{pec}}$ in (3.12) through a weighting factor, $f_{\text{pec}} = w^{\text{pec}}\rho^{\text{pec}}(\mathsf{I})$. One must assign a specific value to this weighting factor (like those related to other functionals) in the intrinsically multi-objective optimization.

### Cell-wise enforcement of PEC condition

The first way to enforce the PEC condition (3.27) is through its average over individual cells. In passing from these multiple conditions to a real scalar, non-negative number to be minimized, we face the same issue that arises when enforcing the local passivity condition (see [7, 6]): to avoid cancellations between positive and negative contributions, we must enforce the minimization of the sum of the *squares* of fields on individual cells. This results in expressing the functional as:

$$\rho^{\text{pec}} = \sum_{i \in \mathcal{I}_{\text{pec}}} \rho_i^{\text{pec}}, \tag{3.28}$$

with

$$\rho_i^{\text{pec}} = \frac{1}{A_i} \iint_{\mathcal{S}_i} |\boldsymbol{E}_{\tan}|^2 \, \mathrm{d}S. \tag{3.29}$$

Here, $A_i$ is the surface area of $\mathcal{S}_i$, and $\mathcal{I}_{\text{pec}} = \{i \in \mathbb{N} \,|\, \mathcal{S}_i \subset \mathcal{S}_{\text{PEC}}\}$ collects the indices of mesh cells belonging to the PEC region.

We observe that this approach is totally coherent with the overall design approach in [6], summarized for convenience in App. A.2, which is based on local averages of the squared magnitude of fields and currents. We will refer to this formulation as "cell-wise" enforcement.

### Edge-wise enforcement of PEC condition

Another option is to consider explicitly the PEC condition (3.27) as in the standard EFIE (PEC part of (3.3)), recast here for ease of reference:

$$\boldsymbol{E}_{\tan}(\boldsymbol{r}) = \Big[\boldsymbol{E}_{\text{inc}}(\boldsymbol{r}) + \mathcal{L}\boldsymbol{J}(\boldsymbol{r})\Big]_{\tan} = \boldsymbol{0}. \tag{3.30}$$

Upon discretization on the PEC region, (3.30) becomes

$$\boldsymbol{\epsilon}_{\text{pec}} = \mathsf{V}_{\text{pec}}^{\text{inc}} + \mathsf{L}_{\text{cpl}}\mathsf{I}_{\text{ibc}} + \mathsf{L}_{\text{pec}}\mathsf{I}_{\text{pec}} = \mathsf{0}. \tag{3.31}$$

In the above, the $N_{\mathrm{pec}} \times 1$ vector $\boldsymbol{\epsilon}_{\mathrm{pec}}$ is the EFIE error, and its norm—the EFIE residue—is the term that is minimized in any iterative solution of the associated problem.

In view of the above, we can thus define the PEC functional as the square of the PEC-restricted EFIE residue:

$$\rho^{\mathrm{pec}} = \left\| \boldsymbol{\epsilon}_{\mathrm{pec}} \right\|^2 . \tag{3.32}$$

We will refer to this formulation as "edge-wise" enforcement, as it derives directly from the EFIE discretized by RWG functions, which are edge-based. The main advantage of using the edge-wise enforcement approach (3.32) is that it can be in principle extended to model other kinds of boundaries, such as those that appear in the case of finite dielectric substrates.

Both formulations will be tested in Section 3.4 in two self-consistent antenna designs that include a realistic feeding structure.

### 3.3.7 Computation

As for the method in [6], the present method allows to use fast algorithms for the field computations in the functional and the gradient computation alike. The PEC-related contributions to the functional all require only field evaluations, in turn expressible in terms of matrix-vector products; these can be computed with $O(N \log N)$ complexity using fast factorizations.

The same holds also for the PEC-related contributions to the gradient. In particular, if the PEC condition is enforced cell-wise via (3.28), the *complex gradient* [70] of the functional can be expressed as:

$$\tilde{\nabla} \rho^{\mathrm{pec}} = \mathbf{L}^{\mathsf{H}} \mathbf{G}^{-1} \sum_{i \in \mathcal{I}_{\mathrm{pec}}} \boldsymbol{\Gamma}_i \mathsf{V} \tag{3.33}$$

with $\mathsf{V} = \mathbf{G}^{-1}(\mathsf{V}_{\mathrm{inc}} + \mathbf{L}\mathsf{I})$. Conversely, if edge-wise enforcement (3.32) is applied, one has:

$$\tilde{\nabla} \rho^{\mathrm{pec}} = \begin{bmatrix} \mathbf{L}_{\mathrm{cpl}} & \mathbf{L}_{\mathrm{pec}} \end{bmatrix}^{\mathsf{H}} \boldsymbol{\epsilon}_{\mathrm{pec}} \tag{3.34}$$

In both cases, the matrix-vector products involving $\mathbf{L}^{\mathsf{H}}$ (or sub-blocks of it) are required only once per gradient evaluation.

### 3.3.8 Handling of the feed

The enforcement of the PEC condition is now applied to self-consistently include the PEC feeding structure into the automated design. In this work, two different types of feedings are considered:

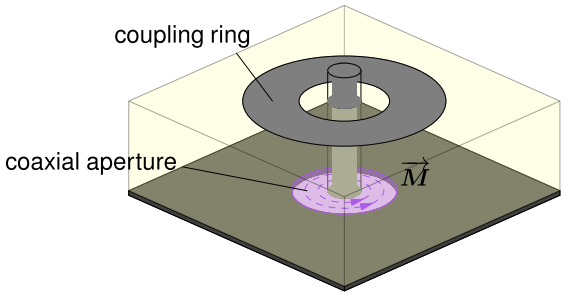


Figure 3.4: 3-D model of a coaxial feed through the ground plane; the specific geometry was inspired by [41]. The source is represented by the equivalent magnetic current $\boldsymbol{M}$ on the aperture.

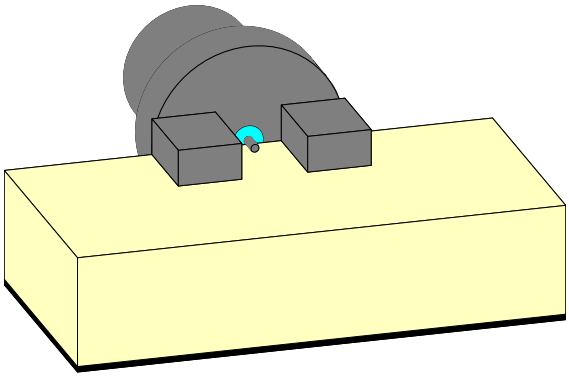

Figure 3.5: 3-D model of the coaxial feed used as source for the edge-fed antenna.

- Feeding from a waveguide (often a coaxial one) through the ground plane of the antenna, including both the vertical structure (most notably, a pin) and horizontal metal parts; this is depicted in Fig. 3.1a and 3.4 with reference to the cases analyzed in Section 3.4.2 and 3.4.3.
- Feeding from the edge of the (planar) antenna, as depicted in Fig. 3.1b and 3.5; this case is described in Section 3.4.4.

The two classes differ mainly for the handling of the incident (forcing) field. We recall that this incident field is the one radiated by external sources in the structure without metallizations (other than the ground plane) and IBC.

The effect of all metal parts (e.g., pin, matching rings, etc.) is self-consistently accounted for by the equivalent currents $\boldsymbol{J}_{\text{pec}}$ on the surface $\mathcal{S}_{\text{PEC}}$ of these parts. These currents are determined entirely *by the design process*.

It is indeed to be remarked that the optimization algorithm evolves the equivalent current over the IBC and PEC regions in such a way that, on completion, this current corresponds to a realizable surface impedance, generates a compliant radiated field *and* satisfies the PEC condition on the metal parts.

In the following, we will describe how the two considered types of feeding are handled in the design process.

#### 3-D feeding through the ground plane

In this case, the source term is the equivalent magnetic current in the coaxial aperture at the level of the ground plane [71, 72], as seen in Fig. 3.4. In order to accelerate convergence, inside the iterative optimization instance the current $\boldsymbol{J}_{\text{pec}}$ on the PEC structures (vertical pin and matching rings) is initialized to the values it would have in the absence of the IBC.

#### 3-D edge-feeding

In case of edge-feeding, the real-life source is typically a coaxial connector placed horizontally on the top of the grounded dielectric substrate, with its outer conductor connected to the ground plane (see Fig. 3.5). Modeling of the 3-D coaxial feed in this case would be awkward and not exact in the underlying integral equation with infinite dielectric kernel. Hence, the modeling is done in two phases.

First, the coaxial connector is fully modeled inside a commercial electromagnetic solver, on a grounded dielectric substrate of infinite size, and without any top-layer metallization. The structure is simulated (full-wave) for a prescribed input port excitation and the radiated electric field is then extracted; this will constitute the incident field (this step corresponds to finding the incident field radiated by the modal current in the case of feeding through the ground in Sec. 3.3.8). This incident field is then used on the overall antenna, IBC and PEC parts.

Finally, we observe that, for this class of antennas, the design process without the feed is hardly meaningful, as opposed to the case of the center-fed circular (or similar) antennas. We will address a simplified, non self-consistent version of the above in the example section (Section 3.4) and show its shortcomings.

## 3.4 Application Examples

We address here the design of a standard circular metasurface antenna fed at its center, and of an elongated rectangular antenna ("strip-like") fed at one end (edge). These test cases are represented in Fig. 3.1a and 3.1b, respectively. In the circular type (Fig. 3.1a), a vertical pin is placed at the center of the antenna, and an annular ring provides matching to the surrounding surface; in this case, the source is represented by the equivalent magnetic currents located at the insertion of the input coaxial cable into the ground plane, while a PEC constraint is imposed on both the pin and the annular ring. In the second case (Fig. 3.1b), the source of the incident field is on-surface, and the PEC region is introduced to represent the tapered section used to connect the feed to the radiating metasurface.

For the center-fed circular antenna, it is expected that the feeding structure may be well decoupled from the metasurface design [42, 73]; conversely, the edge-fed strip-like antenna has direct continuity of the PEC feeding structure and the radiating IBC; hence, the coupling is expected to be significant.

In both cases, two steps are required for the correct modeling of the feed in the optimization instance: the optimization of the geometry of the launching structure, and the extraction of the incident field $\boldsymbol{E}_{\text{inc}}$ to be given as input to the automated design method.

The results shown in this Section are obtained as follows: from the optimum current, the impedance profile $Z(\boldsymbol{r})$ is retrieved, as indicated in Section 3.3.5, keeping only its imaginary part. In the specific examples presented in this Chapter, having established a priori the periodicity of the unit cells that will be used to physically implement the synthesized impedance, the triangular meshing of the antenna geometries is done in such a way that an exact number of triangular mesh cells fits inside a square unit cell of this "higher-level" tessellation. Since the impedance that is synthesized by the automated design method is reconstructed on every triangular cell, this "conformal" meshing allows to compute the impedance corresponding to a square unit cell unequivocally as the average of the values of the synthesized impedance on the triangular mesh cells inside that square. The final impedance profile is therefore constant over square cells. Next, the actual solution is computed by solving the forward problem (3.6) for this impedance profile, the PEC parts, and the specified source field; the corresponding radiation pattern is then calculated. This means that the results take into account a possible efficiency reduction due to the impedance reconstruction process (from the optimized current). These final results are identified as "outputs of the design method".

After this consistency verification, the actual antenna is realized and simulated. The (scalar) impedance distribution is realized with patches; here we use square patches throughout. The final test is the full-wave solution of the actual antenna, which is carried out using either the commercial solver CST Studio Suite [38], or an in-house MoM solver that supports multilayered media through a proper Green's function formulation and enables fast factorization with a GIFFT algorithm [74, 75]. The design instances are carried out on a Desktop PC with Intel Core i9 processor and 64 GB RAM.

### 3.4.1 Feed design

For both the feed geometries considered in this Chapter, the definition of the layout and dimensions of the launching structures must be finalized ahead of the IBC design process. This is done by employing the built-in optimizer inside CST; specifically, the Nelder Mead simplex algorithm is used to perform a multi-objective optimization involving the desired goals.

For the circular antenna layout, the central pin height and the annular ring

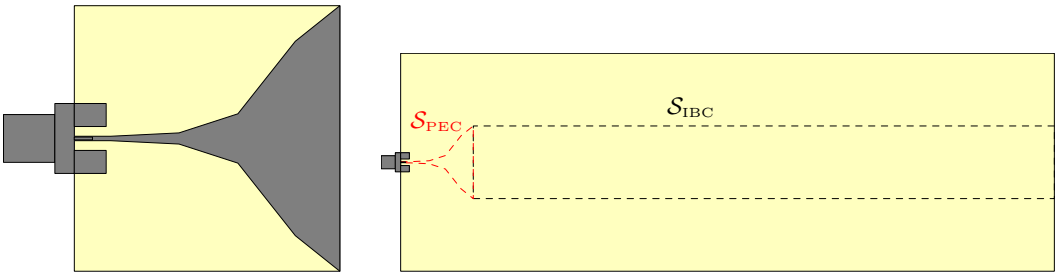


Figure 3.6: Modeling of the realistic feed for the design of the edge-fed antenna (Section 3.4.4): (a) coaxial connector and optimized tapered microstrip section, (b) top view of the coaxial connector placed on the grounded dielectric substrate in absence of metallizations on the top layer. Dashed lines enclose the areas over which the incident field is evaluated and extracted to be given as input to the automated design method.

radius and width (see Fig. 3.4) are optimized in order to minimize the reflection coefficient *and* maximize the radial power flow inside the dielectric substrate. Both objectives are important, since the mere minimization of $S_{11}$ does not guarantee that the field is conveyed through the dielectric to the metasurface, rather than radiated in free space by the vertical pin.

For the edge-fed antenna, a proper tapered microstrip section must be designed to connect the coaxial feed to the actual metasurface. In particular, the tapered input section is optimized in order to match the coaxial feed to the input impedance of a microstrip as wide as the metasurface "strip" transverse width. This choice for the optimization of the tapered section ensures a potential good matching between feed and metasurface, optimally launching the forward traveling wave. In fact, one has to keep in mind that our proposed automated design method will intrinsically try to minimize the reflection coefficient (as explained in Section 3.3.4).

Once the dimensions of the tapered matching section have been finalized, $\boldsymbol{E}_{\mathrm{inc}}$ is retrieved by performing a full-wave simulation of the coaxial connector placed on the grounded dielectric substrate, in absence of any metallization, and extracting the field impinging over the entire structure layout (initial transition region plus IBC region), as explained in Section 3.3.8. This is exemplified in Fig. 3.6, that shows the optimized launching structure and the simulation setup for the extraction of the incident field for the dielectric substrate and working frequency of the design presented in Section 3.4.4.

### 3.4.2 Circular metasurface with broadside pencil beam

The design of a circular metasurface radiating a circularly-polarized pencil beam is considered. A RO3003 dielectric substrate with $\varepsilon_r = 3$ and thickness 1.27 mm is

chosen. The antenna has a radius of $6\,\lambda_0$ at the working frequency of 23 GHz, for a diameter of 156 mm. The reference geometry is shown in Fig. 3.1a. The employed feed structure is shown in Fig. 3.4, and has been inspired by [41, 42].

After the optimization of the launching structure and the determination of the incident field as described in Section 3.4.1, the bounds on the synthesizable impedance and the far-field mask-type constraints must be imposed. The desired far-field masks are shown in all figures reporting radiation patterns. For this design, we consider a capacitive reactance in the range $[-2000\,\Omega, -200\,\Omega]$, which can be implemented using square patch-type unit cells with a periodicity of 1.625 mm ($\approx \lambda_0/8$). The mapping between sheet reactance values and square patch dimensions is retrieved by performing normal-incidence scattering simulations of the constitutive unit cells, as done in [4]. An initial constant current with linear polarization is chosen on the IBC region, while for convergence purposes the initial $\boldsymbol{J}_{\text{pec}}$ is set equal to the one that would flow on the feeding structure in absence the metasurface, as explained in Section 3.3.8. This design task is performed twice, using either the *cell-wise* or the *edge-wise* enforcement of PEC constraint, in order to test the effectiveness of both formulations. Finally, an alternative design case in which the launching structure is replaced by an ideal incident field is reported, to highlight the advantages of the proposed self-consistent inclusion of the realistic model of the feed in the overall performance of the designed antennas.

The number of RWG basis functions for the full geometry, including the launching structure, is $N = 44\,244$ ($N = 41\,776$ in the case of ideal incident field). The optimization of the full circular antennas (including the launching structure) took 1500 iterations, each requiring 7 s to complete, for a total running time of about 3 h for each case. The test design case, with the ideal incident field, required 500 iterations of 4 s each, for a total time of $\approx 33$ min.

Due to the large size of the antenna and the considerable amount of mesh cells needed to obtain accurate results, the simulation of circular metasurfaces with a commercial solver is not possible with the hardware available to the authors; therefore, the actual antennas (with unit cells) are simulated using a MoM-based in-house solver.

### Design with cell-wise enforcement of PEC constraint

The incident field, the optimum current and impedance pattern returned by the automated design method applying the *cell-wise* PEC constraint formulation are shown in Fig. 3.7, while the resulting radiation pattern and its comparison to the one obtained simulating the complete actual antenna are pictured in Fig. 3.8. Only the far-field cut at $\varphi = 0°$ is reported as example, but the mask constraints were set on the whole 3-D upper hemisphere. A perspective view of the complete antenna, with square patches and central feeding structure, that has been simulated with the in-house MoM solver to verify the results of the design method is pictured in

Fig. 3.9.

From Fig. 3.8 we can see that there is good agreement around the main beam between the expected and simulated radiation patterns, both in the co- and cross-polarization components. However, the side lobes appear higher in the simulated pattern, although still quite low and following the shape of the design ones.

The simulated antenna exhibits a total radiation efficiency of 81% and an aperture efficiency of 18%; these quantities are evaluated according to the definitions

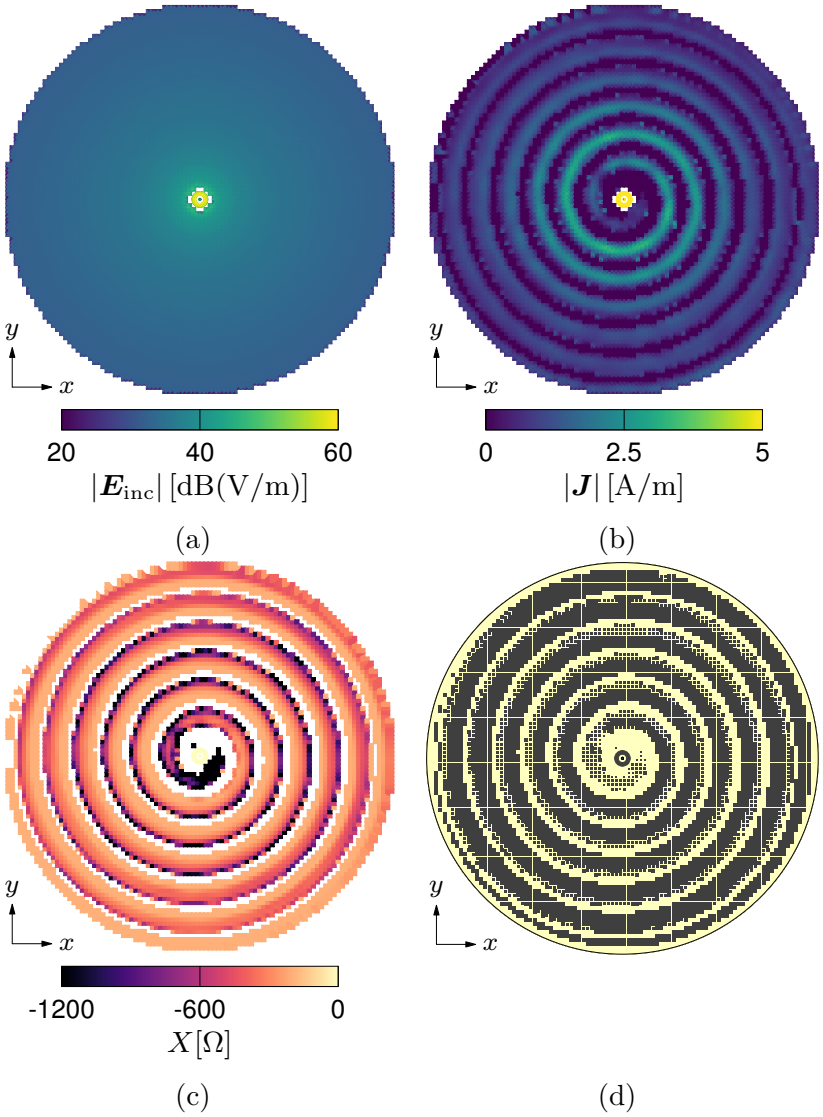


Figure 3.7: *Circular metasurface with pencil beam*, design input/outputs using cell-wise enforcement of PEC constraint: (a) incident electric field, (b) optimum current density returned by the automated method, (c) synthesized impedance pattern, and (d) implementation via square patches of the synthesized impedance.

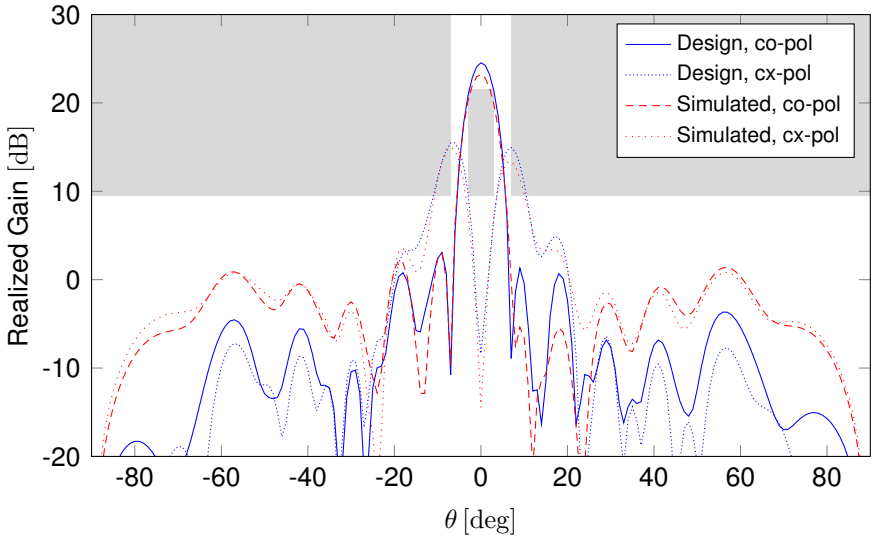


Figure 3.8: *Circular metasurface with pencil beam*, full self-consistent design with cell-wise enforcement of PEC constraint: comparison between the far-field pattern due to the reconstructed equivalent currents (*Design*) and the one obtained with full-wave simulation of the complete antenna shown in Fig. 3.9 (*Simulated*).

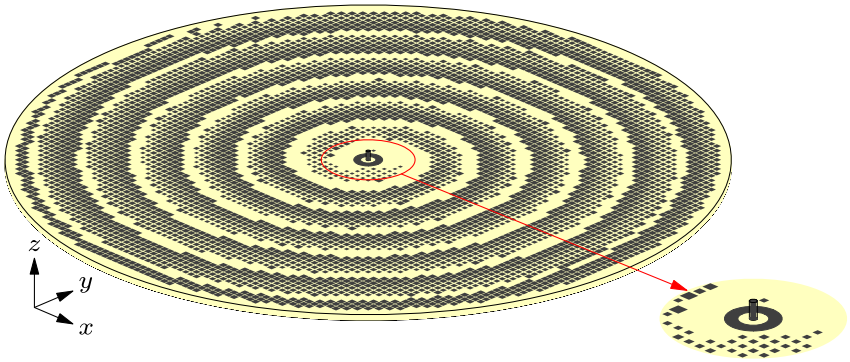


Figure 3.9: Perspective view of the actual circular antenna, with square patches and central feeding structure, that has been simulated with the in-house MoM solver to verify the results of the design method in Section 3.4.2.

given in [68].

### Design with edge-wise enforcement of PEC constraint

The same design is now carried out enforcing the PEC condition *edge-wise*. The synthesized impedance pattern and its implementation using square patches are shown in Fig. 3.10, while the comparison between the far-field predicted by the design method and the one obtained with full-wave simulation of the complete

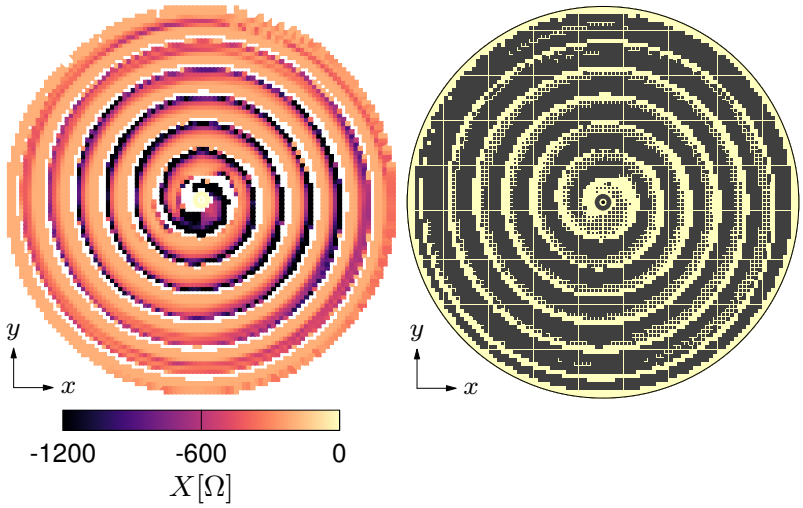


(a) (b)

Figure 3.10: *Circular metasurface with pencil beam*, full self-consistent design using edge-wise enforcement of PEC constraint: (a) synthesized impedance pattern, and (b) its implementation via square patches.

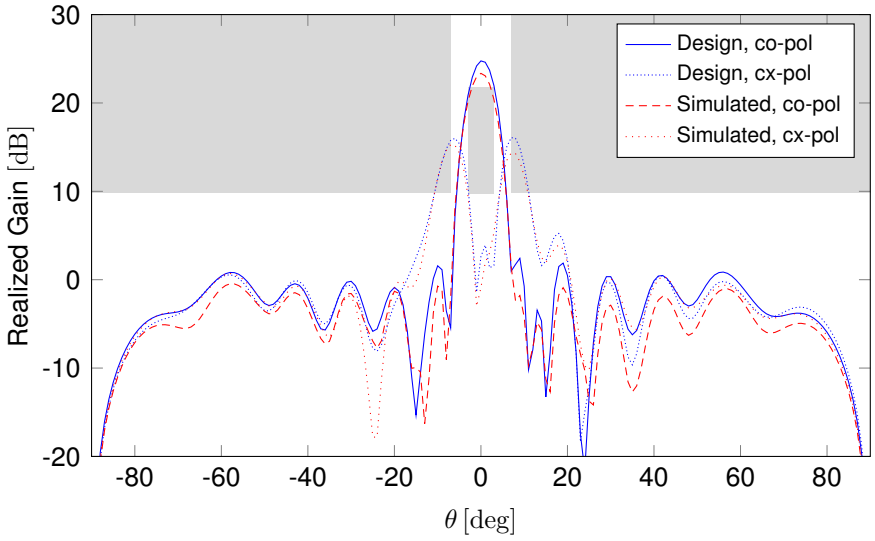


Figure 3.11: *Circular metasurface with pencil beam*, full self-consistent design with edge-wise enforcement of PEC constraint: comparison between the far-field pattern due to the reconstructed equivalent currents (*Design*) and the one obtained with full-wave simulation of the complete antenna (*Simulated*).

antenna is pictured in Fig. 3.11. The impedance pattern is very similar to the one obtained with *cell-wise* enforcement of the PEC constraint (see Fig. 3.7c); the main

discrepancy can be found near the central launching structure. On the other hand, there is excellent agreement between the expected and simulated radiation patterns also in the side-lobe region, while the achieved realized gain at broadside is the same as in the previous design. These results suggest that, for the circular geometry with central pin and annular ring, the *edge-wise* formulation may be slightly more effective in enforcing the PEC condition and the self-consistent evolution of the current density in these regions at every step of the optimization process. The total and the aperture efficiencies of the simulated antenna are 85% and 18%, respectively.

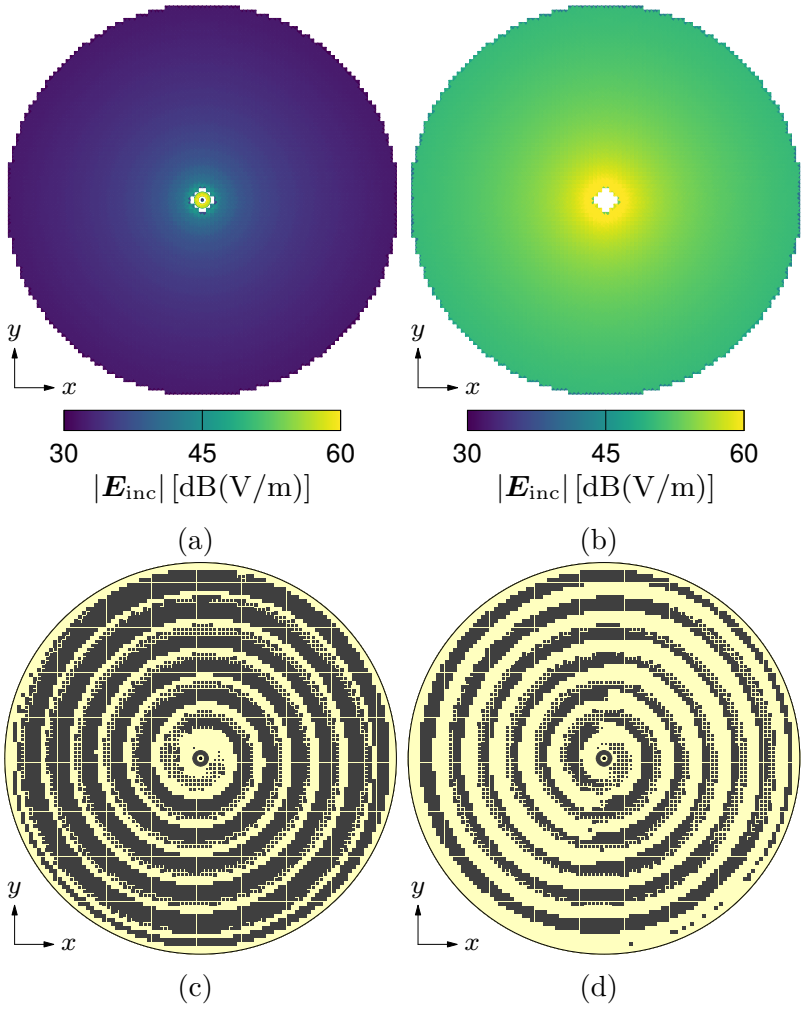


Figure 3.12: *Circular metasurface with pencil beam*, comparisons between the self-consistent design with a realistic feed of Section 3.4.2 and the one with a $TM_0$ approximate source: (a) incident electric field, realistic feed (same of Fig. 3.7a, different scale), (b) incident $TM_0$ electric field, (c) metallization pattern, realistic feed, (d) metallization pattern, $TM_0$ source.

### Design with ideal cylindrical surface wave

In order to demonstrate the advantage of including a realistic modeling of the feed in the design of circular metasurfaces, an alternative design case is presented in which the launching structure, comprising the central pin and the annular ring, is absent in the optimization instance, and the incident field is simply approximated with its asymptotic form as a $TM_0$ cylindrical surface wave, as it is commonly done in the literature [76, 6].

The $TM_0$ incident field is pictured in Fig. 3.12b, while the complete geometry of the antenna designed starting from such field is shown in Fig. 3.12d. The synthesized impedance pattern is very similar to the one obtained previously by properly modeling the launching structure (see Fig. 3.12c for a comparison with the design of Section 3.4.2); however, there are more empty areas (infinite impedance, no IBC) in the spiral distribution of patches, most likely due to the fact that the approximate $TM_0$ incident field decades less rapidly than the real one (see Fig. 3.12a and 3.12b) and it is thus still larger towards the edge of the circular area.

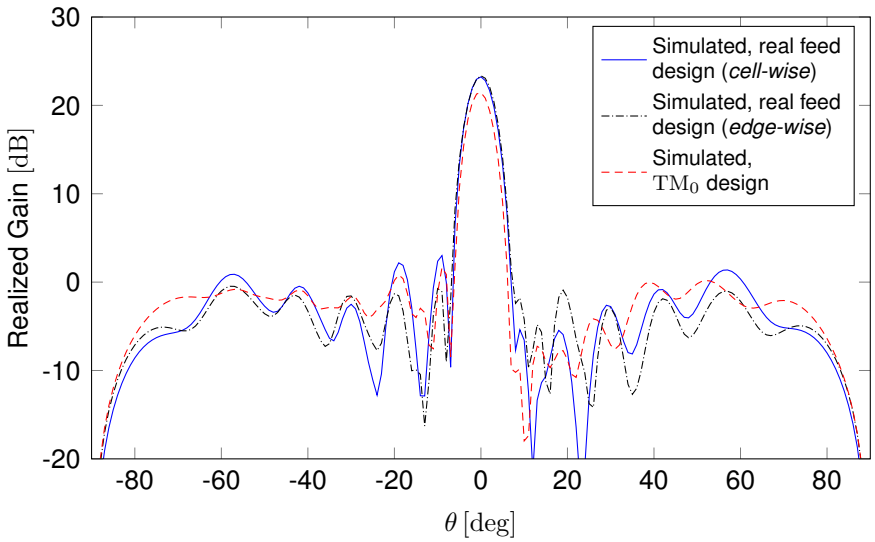


Figure 3.13: *Circular metasurface with pencil beam*, comparison between the designs with full feed and approximate $TM_0$ incident field. The patterns are the simulations of the actual antennas in Fig. 3.12c and 3.12d, that include the actual feed as in Fig. 3.9. Solid line: antenna designed considering the actual feed – cell-wise; dash-dotted line: antenna designed considering the actual feed – edge-wise; dashed line: antenna designed with a $TM_0$ incident field.

We now compare the performances of the three antennas: the one designed starting from a $TM_0$ incident field, and the ones designed with the accurate modeling of the feed (shown previously in Fig. 3.8 and 3.11). Fig. 3.13 shows the radiation

patterns of the complete antennas depicted in Fig. 3.7d, 3.10b and 3.12d. It appears that using the approximate $TM_0$ incident field for the antenna design leads to a drop in the actual antenna realized gain of about 2 dB; in fact, the antenna designed starting from the ideal cylindrical wave shows a lower total radiation efficiency of 66% and a smaller aperture efficiency of 15%. This proves the importance of considering the real 3-D feeding structure in the design of metasurface antennas.

### 3.4.3 Circular metasurface with multi-beam radiation

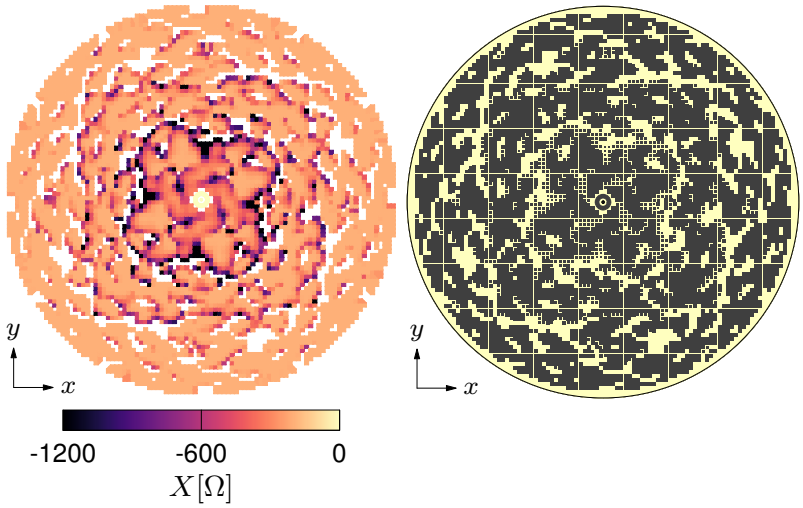


(a) (b)

Figure 3.14: *Circular metasurface with multi-beam*, design outputs using cell-wise enforcement of PEC constraint: (a) synthesized impedance pattern, and (b) its implementation via square patches.

A more challenging design of a circular metasurface radiating a circularly-polarized multi-beam is carried out to test the performance of the proposed automated design method. The same substrate and launching structure of Section 3.4.2 are employed to synthesize an antenna that radiates four beams in the directions given by $\theta = 45°, \varphi = \{45°, 135°, 225°, 315°\}$. An initial constant current with linear polarization is chosen, and the PEC constraint is enforced *cell-wise*. As in the previous cases, 1500 iterations of the optimization method were carried out, for a total running time of about 3 h.

The synthesized impedance pattern and its implementation using square patches are shown in Fig. 3.14, while the comparison between the far-field predicted by the design method and the one obtained with full-wave simulation of the complete antenna is pictured in Fig. 3.15. Multi-beam radiation is achieved without any a priori imposition on the shape of the impedance pattern. There is good agreement

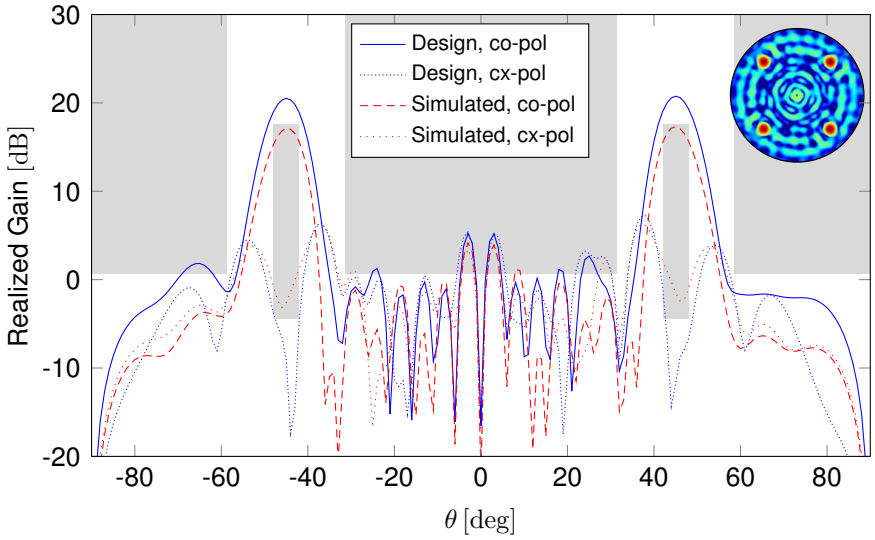


Figure 3.15: *Circular metasurface with multi-beam*, full self-consistent design with cell-wise enforcement of PEC constraint: comparison between the far-field pattern due to the reconstructed equivalent currents (*Design*) and the one obtained with full-wave simulation of the complete antenna (*Simulated*) in the plane $\varphi = 45°$. The inset shows the co-polarization pattern in the $u$-$v$ plane.

between the expected far-field pattern and the simulated one, with a drop of 3 dB in the peak simulated realized gain; this discrepancy may be due to inaccuracies in the full-wave simulation, given the large number of mesh cells required to obtain accurate results. The total radiation efficiency of the simulated antenna is equal to 75%.

### 3.4.4 "Strip-like" rectangular metasurface with broadside radiation

Another example of the application of the described numerical method is the design of a quasi-1D leaky-wave antenna (LWA) to achieve broadside radiation with inline feeding from one end. This is typically hard to obtain with conventional approaches [4, 3] due to the presence of an open stopband that leads to a nearly-total reflection of the traveling wave [10]; hence, it is a very good test for the proposed method.

The reference geometry is the rectangular one shown in Fig. 3.1b. A 2.286 mm-thick RO3006 substrate ($\varepsilon_r = 6.5$) is considered. The design frequency is 10 GHz. For "strip-like" metasurface antennas, the far-field mask-type constraints are set only in the $\varphi = 0°$ plane. The impedance constraints are based on the values that can be obtained using patch-type unit cells with a periodicity of 2 mm, for a total

feasible reactance range of $[-10\,000\,\Omega, -150\,\Omega]$.

As already noted, the physical layout makes it virtually compulsory to include the feeding structure (at least the tapering section) in the design process. The launching structure has been inspired by [4]; its optimization is carried out as described in Section 3.4.1, and its final layout is shown in Fig. 3.6a.

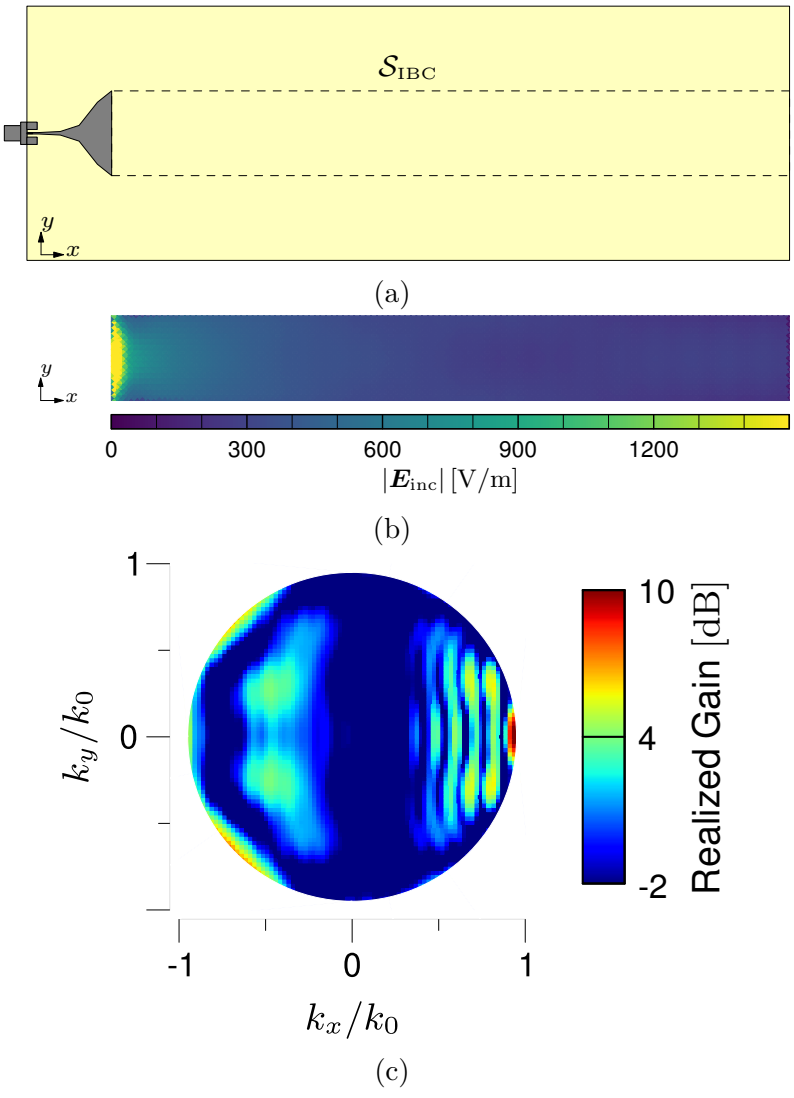


Figure 3.16: *Strip-like LWA, broadside radiation*: design inputs for the case without self-consistent modeling of the PEC launching structure: (a) setup for the simulation of the real antenna feed using CST, where the dashed lines enclose the area of extraction of the incident electric field ($\mathcal{S}_{\text{IBC}}$); (b) extracted incident electric field to be used in the design method in $\mathcal{S}_{\text{IBC}}$; (c) "input" far-field in the $u$-$v$ plane, due to the radiation of the feed, i.e. associated to the "incident" field.

The IBC region is a 30 mm×240 mm rectangular area. The current is initialized to an $\hat{\boldsymbol{x}}$-directed constant current which radiates broadside with linear polarization (which would not be physically realizable).

In the following, we examine the relevance of incorporating a realistic feed in the design of "strip-like" rectangular metasurface antennas, and the possible differences in using either the *cell-wise* or *edge-wise* enforcement of the PEC constraint. The number of degrees of freedom for the full geometry (IBC region and launching structure) is $N = 11\,116$. The optimization of the full rectangular antennas (including the launching structure) presented in Section 3.4.4 took 20 000 iterations, each requiring 0.85 s to complete, for a total running time of about 4 h 40 min for each case.

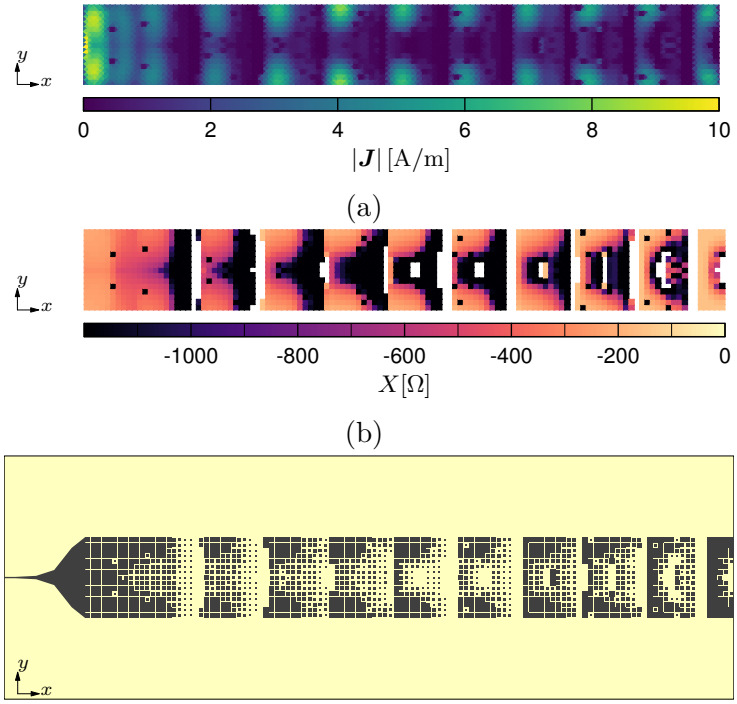


Figure 3.17: *Strip-like LWA, broadside radiation*: Design outputs for the solution without the self-consistent modeling of the launching structure: (a) optimum IBC current density returned by the design method; (b) impedance pattern corresponding to the optimum current in (a); (c) implementation via square patches of the synthesized impedance in (b).

### Design without self-consistent modeling of the launching structure

We begin our analysis by considering a simplified, non self-consistent description of the launching structure. For this (approximate) design case, the incident field

is the one generated by the full launching structure, comprising the 3-D connector and the tapered section; the tapered section is left open-ended as show in Fig. 3.16. It is apparent that this is already a good approximation, since it takes the feeding mechanism into account and does not use an ideal incident field. On the other hand, only the IBC rectangular area $\mathcal{S}_{\text{IBC}}$ is considered (i.e., optimized) in the design, but not the PEC launching region $\mathcal{S}_{\text{PEC}}$ (see Fig. 3.16a). This means that the tapered launching metal is non self-consistently accounted for. In this case, the number of degrees of freedom is $N = 10\,665$ and the optimization process required 15 000 iterations of 0.48 s each, for a total running time of about 2 h.

Figure 3.16b shows the incident electric field extracted from CST. Since the launching structure may generate (unwanted) radiation, it is necessary to consider also its contribution to the far-field as input to the design method (see Fig. 3.16c).

The optimum current synthesized by the automated method, the corresponding impedance pattern and its implementation with square patches are shown in Fig. 3.17. The empty areas in Fig. 3.17b indicate an open circuit condition for the IBC, i.e., absence of metallization on the dielectric substrate.

The radiation pattern predicted by the automated design process is compared to the one obtained via full-wave simulation of the complete antenna in Fig. 3.18, together with the far-field masks imposed as targets in the optimization instance. There are several discrepancies in the two patterns: the main beam in the CST simulation is not directed at broadside, but tilted towards 1.5°, and there is a

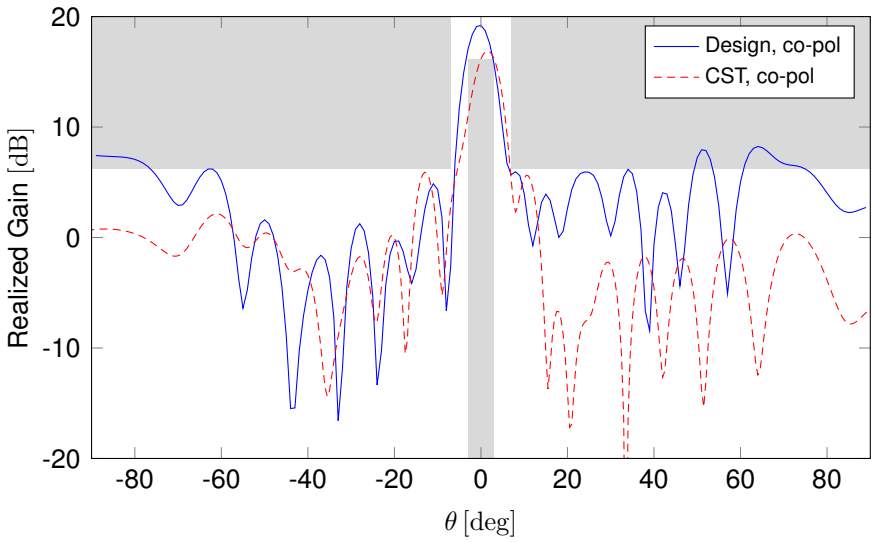


Figure 3.18: *Strip-like LWA, broadside radiation*: comparison between the far-field pattern due to the reconstructed equivalent currents (*Design*) and the one obtained by CST simulation (*CST*), for the design without self-consistent modeling of the launching structure inside the optimization instance.

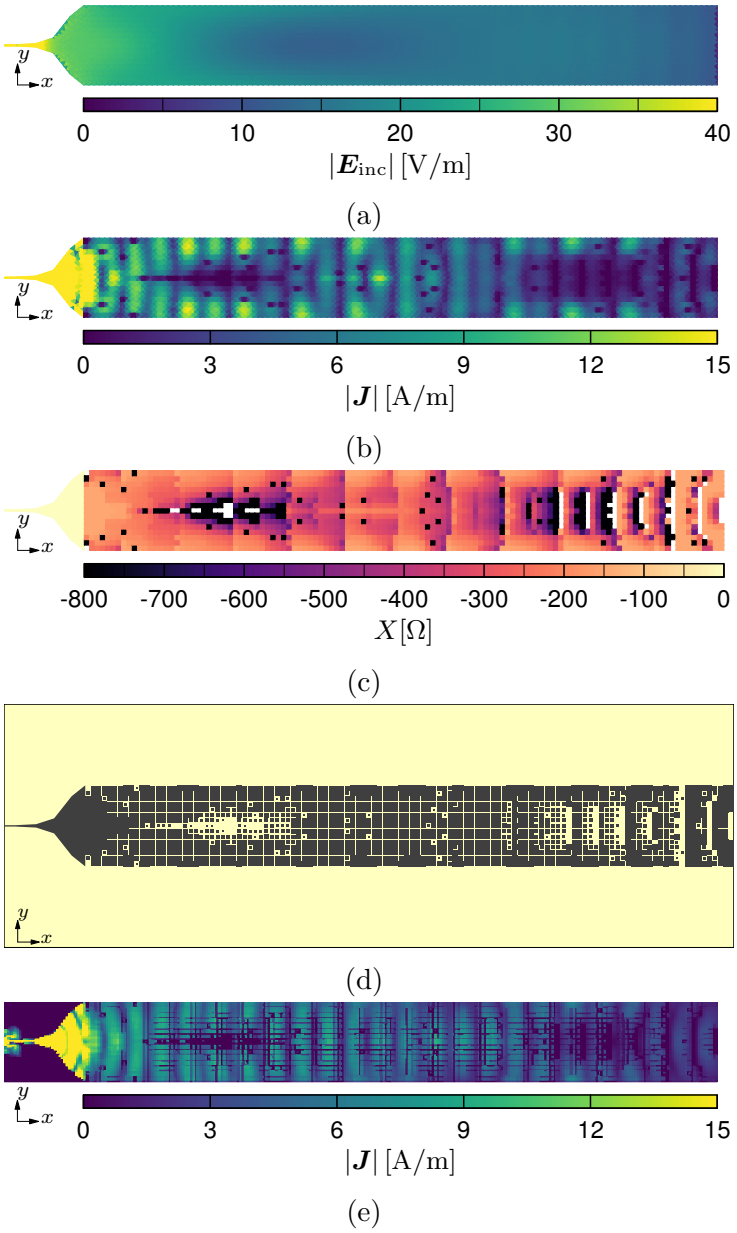


Figure 3.19: *Strip-like LWA, broadside radiation*: Design input/outputs with self-consistent modeling of the launching structure, obtained using cell-wise enforcement of PEC constraint: (a) incident electric field, extracted from the full-wave simulation of the coaxial connector in CST; (b) optimum current density returned as output by the design method and (c) the corresponding impedance pattern; (d) implementation via square patches of the synthesized impedance; (e) current density obtained simulating the actual antenna in CST.

2 dB loss in the realized gain, resulting in a total radiation efficiency of 84% and an aperture efficiency of about 56%. Moreover, the side lobes towards grazing directions, predicted by the approximate design method, are significantly higher than those of the actual antenna.

These differences indicate that failing to self-consistently model the tapered PEC section inside the design algorithm forces to neglect the interaction between the launching structure and the metasurface, leading to significant inaccuracies in the final results (despite the high accuracy level in the computation of the incident field achieved by including the feeding structure).

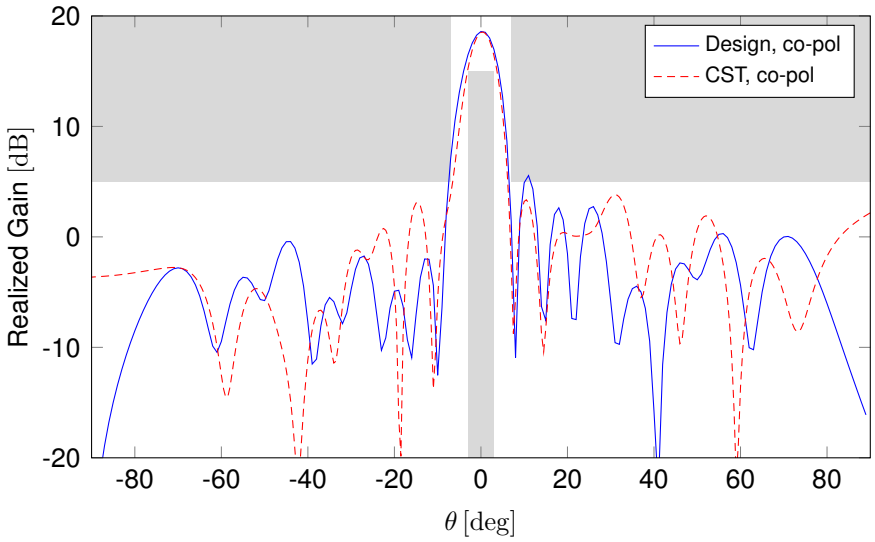


Figure 3.20: *Strip-like LWA, broadside radiation*: Comparison between the far-field pattern due to the reconstructed equivalent currents (*Design*) and the one obtained by full-wave simulation in CST (*CST*), for the self-consistent design with cell-wise enforcement of the PEC condition.

### Design with self-consistent modeling of the launching structure and cell-wise enforcement of PEC constraint

We consider now both the PEC and the IBC region self-consistently in the design process, as proposed in this Chapter; coherently with this, the incident field $\boldsymbol{E}_{\text{inc}}$ is now extracted from full-wave simulations of the 3-D coaxial feed *only* (see Fig. 3.6b). This field is shown in Fig. 3.19a, while the optimized current density returned by the automated method and the corresponding impedance pattern are represented in Fig. 3.19b and 3.19c, respectively. The synthesized impedance profile is unconventional and different from the typical sinusoidal modulation used to design 1D LWAs [4]. Figures 3.19d and 3.19e show the physical implementation of

the synthesized impedance pattern and the current density obtained from full-wave simulation of the full antenna.

The comparison between the simulated far-field pattern and the one predicted by the automated design method is shown in Fig. 3.20, together with the mask-type constraints imposed on the desired radiation pattern. There is excellent agreement between the two patterns: broadside radiation is achieved as expected with a *realized* gain of 18.5 dB, thus effectively overcoming the open stopband problem. Although different from those of the IBC approximation, the simulated side lobes satisfy the desired SLL. The discrepancies in the pattern are mainly due to the fact that the automated design method posits an infinite dielectric substrate, while in the 3-D simulation implemented in the commercial solver the dielectric layer is finite (see Fig. 3.19d). A further source of differences may be traced back to the unit cell design, which is based on a local-periodicity approximation. The total radiation efficiency shown by the simulated antenna is 92%, while the aperture efficiency is equal to 75%.

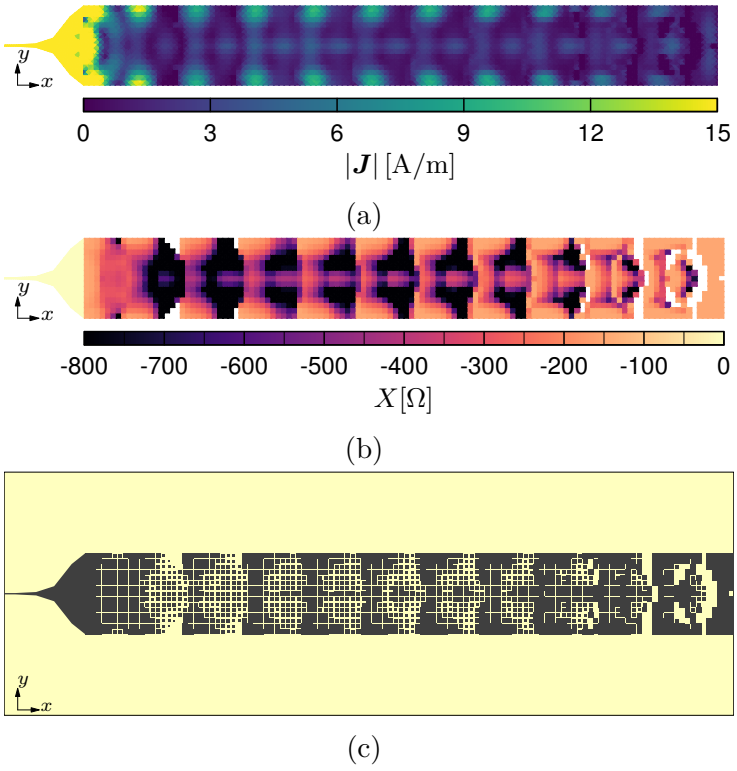


Figure 3.21: *Strip-like LWA, broadside radiation*: Design outputs for the self-consistent solution obtained with edge-wise enforcement of the PEC constraint: (a) optimum current density returned by the design method, (b) corresponding impedance pattern; (c) implementation via square patches of the synthesized impedance in CST.

**Design with self-consistent modeling of the launching structure and edge-wise enforcement of PEC constraint**

Finally, we carry out the same design as in Section 3.4.4 using the *edge-wise* enforcement of the PEC constraint defined in (3.32). The optimum current density and the corresponding impedance pattern are shown in Fig. 3.21, together with its implementation via square patches.

The two synthesized impedance profiles in Fig. 3.19c and Fig. 3.21b show some differences, resulting in slightly different patterns; the edge-wise enforcement (see Fig. 3.22) appears to achieve a higher realized gain of 19.2 dB, at the expenses of a worse side lobe profile. However, after the realization and simulation of the complete antenna with CST, the side lobes turn out to be better and actually very similar to those of the other method. The total radiation efficiency and the aperture efficiency are 98% and 82%, respectively.

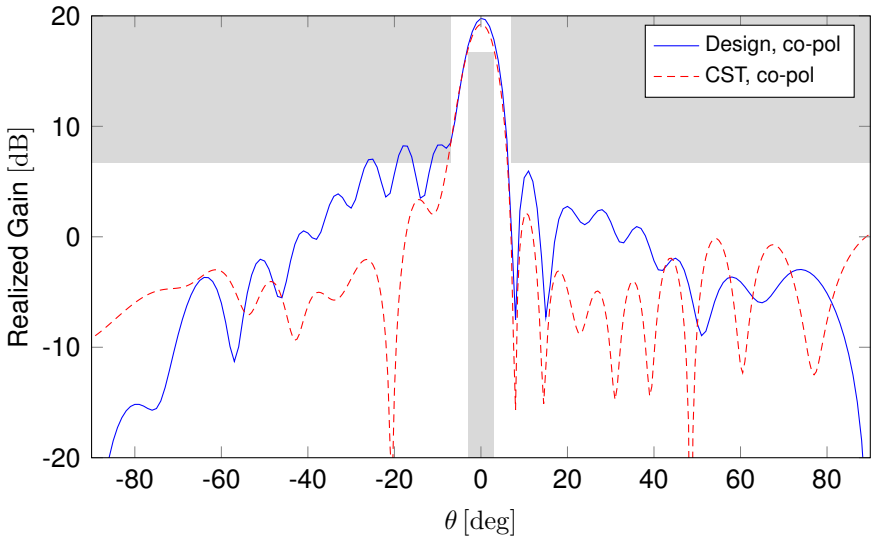


Figure 3.22: *Strip-like LWA, broadside radiation*: Comparison between the far-field pattern due to the reconstructed equivalent currents (*Design*) and the one obtained with full-wave simulation in CST (*CST*), for the design achieved by enforcing the PEC condition edge-wise.

### 3.4.5 "Strip-like" rectangular metasurface with squinted beam

The task of designing a "strip-like" antenna radiating a squinted beam is also undertaken, to demonstrate the capabilities of the proposed method. The same substrate and dimensions of the previous examples are considered, and the optimization process took again about 4 h 40 min.

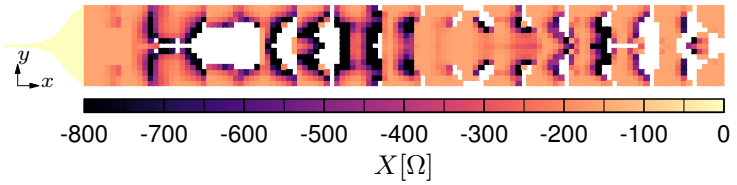


(a)

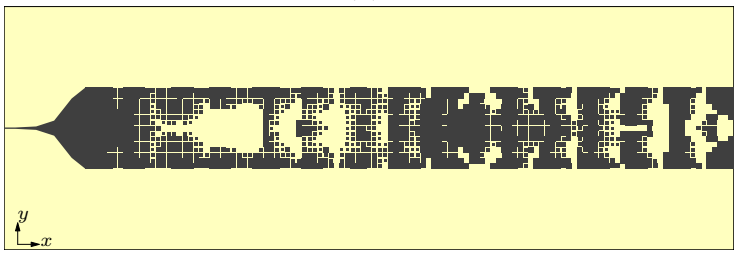


(b)

Figure 3.23: *Strip-like LWA, squinted beam*: Design outputs for the self-consistent solution obtained with cell-wise enforcement of the PEC constraint: (a) synthesized impedance pattern, and (b) its implementation via square patches.

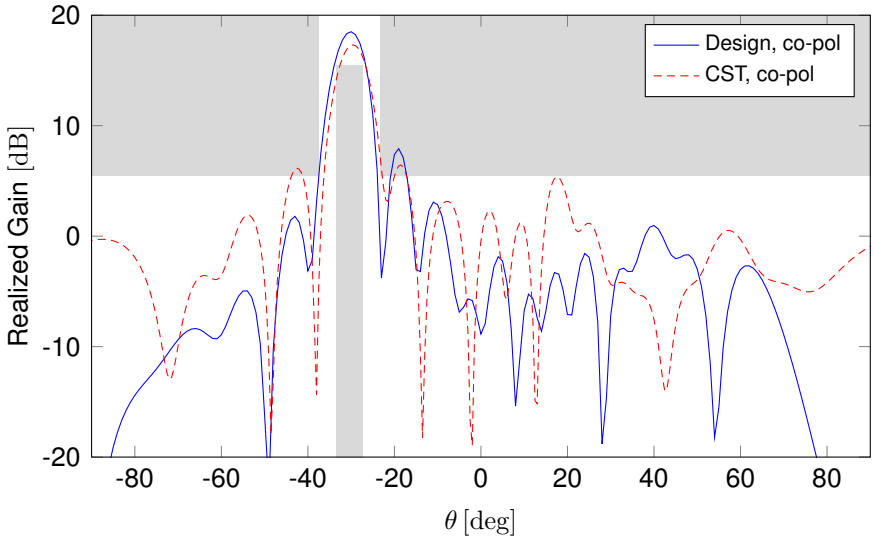


Figure 3.24: *Strip-like LWA, squinted beam*: Comparison between the far-field pattern due to the reconstructed equivalent currents (*Design*) and the one obtained with full-wave simulation in CST (*CST*).

The target is a $-30°$ backward beam. The design is carried out using *cell-wise* enforcement of the PEC constraint. The synthesized impedance pattern and its geometrical implementation using square patches are shown in Fig. 3.23, while the

far-field pattern returned by the design method and the one resulting from full-wave simulation of the complete antenna are pictured in Fig. 3.24, together with the far-field mask-type constraints imposed in the optimization instance. The two patterns are in excellent agreement around the main beam, with only a small drop ($-1.2\,\mathrm{dB}$) in the realized gain. The simulated total radiation efficiency is 98%. There is some discrepancy in the side lobes region, that increases going farther from the main beam and can be ascribed to the finite dielectric substrate used in the simulation environment; nevertheless, the simulated side lobes abide to the SLL mask constraint.

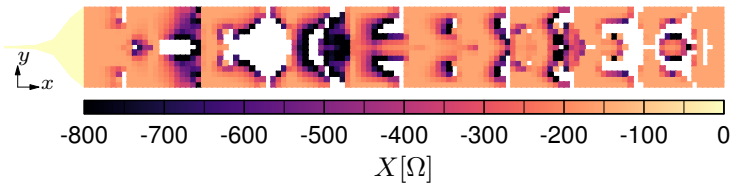


(a)

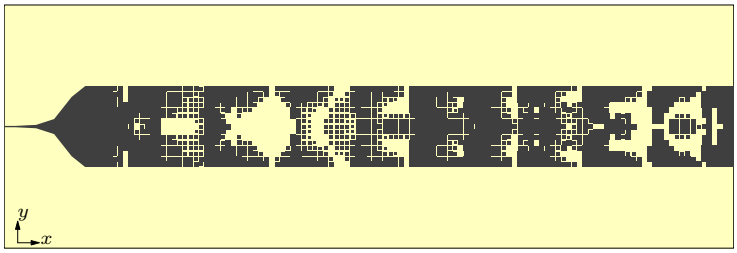


(b)

Figure 3.25: *Strip-like LWA, cosecant squared pattern*: Design outputs for the self-consistent solution obtained with cell-wise enforcement of the PEC constraint: (a) synthesized impedance pattern, and (b) its implementation via square patches.

### 3.4.6 "Strip-like" rectangular metasurface with cosecant squared pattern

Finally, we address the design of a rectangular metasurface that radiates a cosecant squared beam [68], with power pattern $D(\theta)$ defined as [6]:

$$D(\theta) = \frac{\sin^2(\theta_{\min})}{\sin^2(\theta)}, \quad \theta_{\min} \leq \theta \leq \theta_{\max}. \tag{3.35}$$

We consider a case with $\theta_{\min} = 10°$, $\theta_{\max} = 40°$; radiation constraints are imposed in the principal plane $\varphi = 0°$. The admissible ripple is set at $\pm 2\,\mathrm{dB}$ from the target mask. Using the same antenna geometry of the previous examples, this optimization instance required about 4 h 40 min to complete. *Cell-wise* enforcement of the PEC constraint is employed.

The synthesized impedance pattern and its geometrical implementation using square patches are shown in Fig. 3.25, while the far-field pattern returned by the design method and the one resulting from full-wave simulation of the complete antenna are pictured in Fig. 3.26. There is good agreement between the output of design method and the simulations results: the simulated radiation pattern abides to the mask-type constraints almost everywhere, with the exception of a small backward side lobe that was already expected to exceed the SLL mask from the design stage. The total radiation efficiency is 98%.

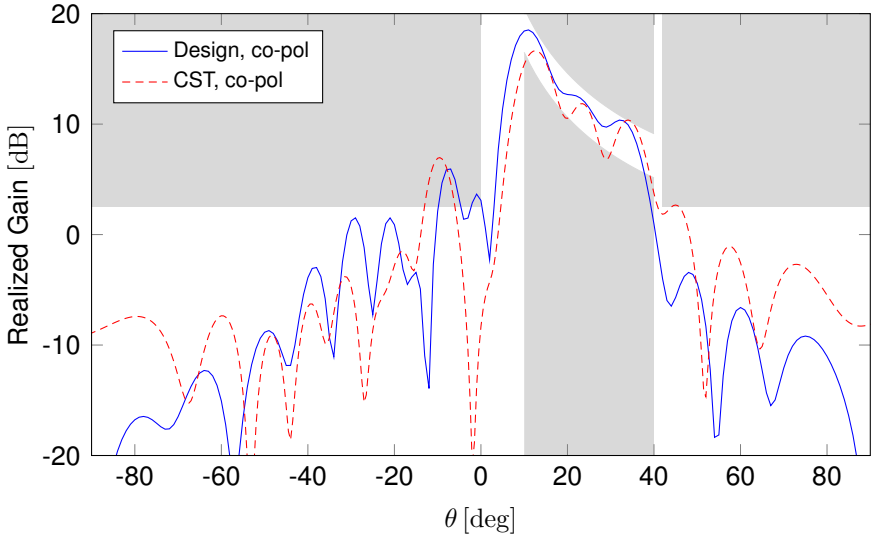


Figure 3.26: *Strip-like LWA, cosecant squared pattern*: Comparison between the far-field pattern due to the reconstructed equivalent currents (*Design*) and the one obtained with full-wave simulation in CST (*CST*).

## 3.5 Conclusions

We have presented a method to self-consistently incorporate a specified PEC feeding structure in the current-only inverse design of metasurface antennas. We have shown application examples of center-fed metasurface antennas and edge-fed "strip-like" LWAs; in the latter, the feed is electrically connected to the IBC part. We have found that including the feed in the design of center-fed circular antennas is important, especially to avoid deterioration of the peak gain, in line with recent literature. Its impact in "strip-like" LWAs is significantly more pronounced, affecting the accuracy of the radiation pattern in both the main and side lobe regions.

# Chapter 4

# Automated Synthesis of Metasurfaces for the Design of Broadside-Radiating Leaky-Wave Antennas

End-fed leaky-wave antennas notoriously suffer from the open-stopband problem, that hinders radiation at broadside and causes a dramatic drop in the realized gain. In this Chapter, we design and fabricate broadside-radiating leaky-wave antennas using the automated deterministic method for the synthesis of metasurfaces described in Chapter 3. The procedure effectively overcomes the open-stopband problem and enables radiation at broadside. The performance of the designed antennas is corroborated by full-wave simulations and experimental measurements of fabricated prototypes.

## 4.1 Introduction

The problem of the open stopband (OSB) at broadside in leaky-wave antennas (LWAs) has been the subject of many studies, aimed at finding design strategies to overcome this limitation. The OSB arises in periodic structures, such as sinusoidally-modulated reactance surfaces (SMRS) [3, 4], and is caused by the interaction at broadside of a couple of Floquet harmonics whose power flows in opposite direction [10, 77]. This leads to a rapid increase (and then drop to zero) in the attenuation constant of the propagating wave, thus transforming the latter in a standing wave and reducing the input matching and the efficiency of the antenna.

Techniques for suppressing the OSB have been developed over the years: for traditional LWAs, like slotted waveguides, they rely mainly on the optimization of the geometry of the constitutive unit cell of the periodic arrays (these unit cells are

of resonant size). Examples include the introduction of a quarter-wave transformer or a matching stub into the unit cell [78], the use of two non-identical elements [79], phase reversal [80], frequency balancing and Q-balancing in composite right/left-handed (CRLH) LWAs [81], and exploiting a more general longitudinal or transverse asymmetry [82, 83]. These methods usually require a combination of approximate circuit models and Bloch-wave analysis for the initial design, supported by full-wave modal analysis for final refinement; the aid of either eigenmode or driven full-wave solvers is needed for the determination of the equivalent transmission-line parameters.

More recently, metasurfaces have been employed in the realization of LWAs, thanks to their versatility in the manipulation of electromagnetic fields. In [84], a LWA capable of radiating at broadside was designed by means of a four-layer bian-isotropic Huygens' metasurface. In [85], open-stopband suppression was achieved using a sinusoidally-modulated anisotropic metasurface for circular polarization; it was concluded that an isotropic solution (with linear polarization) could not effectively remove the OSB effect. In [56, 57], optimization of the aperture fields allowed to synthesize linearly-polarized, broadside-radiating LWAs, with the design technique limited to 1-D solutions.

In this Chapter, we demonstrate the possibility to achieve linearly-polarized broadside radiation with LWAs based on a single-layer isotropic metasurface. For the first time, the antenna is designed using an automated, deterministic numerical method that considers the full 2-D impedance surface and a realistic 3-D feeding structure. The employed algorithm for the synthesis of metasurfaces, described in detail in Chapter 3, was first presented in [6] and generalized in [40]; this method allows control of side lobes and has the advantage of maximizing the *realized gain*, thus lending itself to be applied against the OSB problem, condition that causes a dramatic worsening of the reflection coefficient. In Chapter 3, a first example of broadside-radiating LWA synthesis was reported, with the aim of showing the ability to handle a complex feeding structure. In this Chapter, we will leverage that approach and conduct the full design, fabrication and measurement of two solutions based on different dielectric substrates. Measured results confirm indeed the achievement of broadside radiation with high realized gain.

## 4.2 Design

The automated method for the design of metasurface antennas used in this Chapter was described in detail in Chapter 3. Here, we will recount the design steps and show the results obtained with the aforementioned algorithm. The inputs of the automated design process are:

a) far-field mask-type specifications,

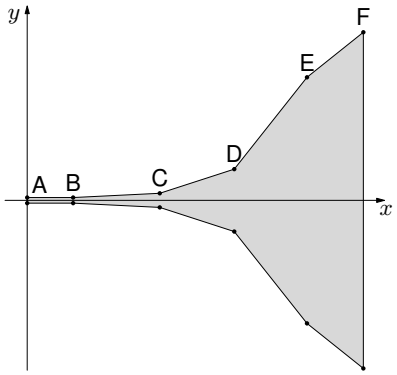


| | RO3006 | | Diclad880 | |
|---|---|---|---|---|
| | $x$ | $y$ | $x$ | $y$ |
| A | 0 | 0.25 | 0 | 0.25 |
| B | 4.1 | 0.25 | 4.1 | 0.25 |
| C | 11.83 | 0.63 | 15.08 | 0.69 |
| D | 18.48 | 2.785 | 23.14 | 1.785 |
| E | 24.97 | 10.98 | 27.17 | 15 |
| F | 30 | 15 | 30 | 15 |

Figure 4.1: Polygonal shape of the launching structure and optimized dimensions (in mm) for the two design cases. The shape is symmetric with respect to the $x$-axis.

b) antenna layout,

c) feasibility bounds on the impedance for the chosen size of the unit cell, and

d) geometric model of the feeding structure.

Two dielectric substrates are considered: a 2.286 mm-thick RO3006 substrate ($\varepsilon_r = 6.5$), and a 3.2 mm-thick Diclad880 substrate ($\varepsilon_r = 2.2$). The latter has been obtained by exploiting two panels of 1.524 mm thickness, coupled with a Rogers 2929 50 $\mu$m-thick film in the middle. The design frequency is 10 GHz. For both substrates, the IBC region is defined over a $240 \times 30\,\text{mm}^2$ rectangular area.

To realize the IBC we exploit the square patches metal pattern, since it is the more robust from the realization point of view. The geometric bounds of the patches are set in agreement with the fabrication specifications, and the impedance bounds associated to the realizability range are computed with the periodic approximation, adopting the extraction method described in [4]. The obtained impedance ranges are $[-10\,000\,\Omega, -150\,\Omega]$ for the RO3006 substrate and $[-10\,000\,\Omega, -200\,\Omega]$ for the Diclad880 design. Since we deal with isotropic (scalar) impedance, the translation from impedance to patch size is a straightforward process using the charts in Fig. 4.2.

Finally, the feeding structure is designed ahead of the synthesis process. It consists of a tapered microstrip section whose polygonal profile is optimized to match an input 50 $\Omega$-coaxial cable to the characteristic impedance of a microstrip line as wide as the metasurface region. This polygonal shape is outlined in Fig. 4.1, together with its dimensions for the considered two design cases, optimized using CST Studio Suite [38].

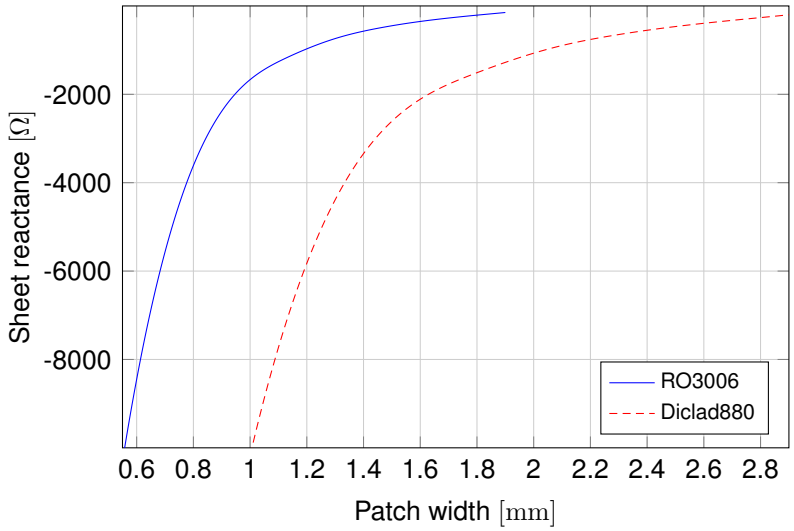


Figure 4.2: Mapping between patch width and reactance for the RO3006 and Diclad880 substrates.

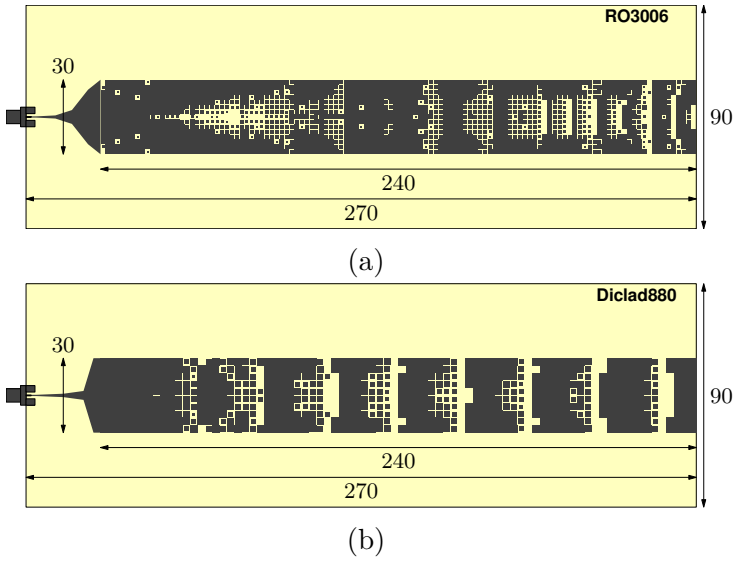


Figure 4.3: Antenna layout for the considered dielectric substrates: (a) RO3006, (b) Diclad880. Dimensions are in mm.

## 4.3 Results

The metasurface patterns synthesized by the automated method to achieve broadside radiation are shown in Fig. 4.3, for the considered dielectric substrates. From Fig. 4.3 it appears clear that forgoing the imposition of any analytical modulation scheme on the impedance surface allows the numerical method to exploit

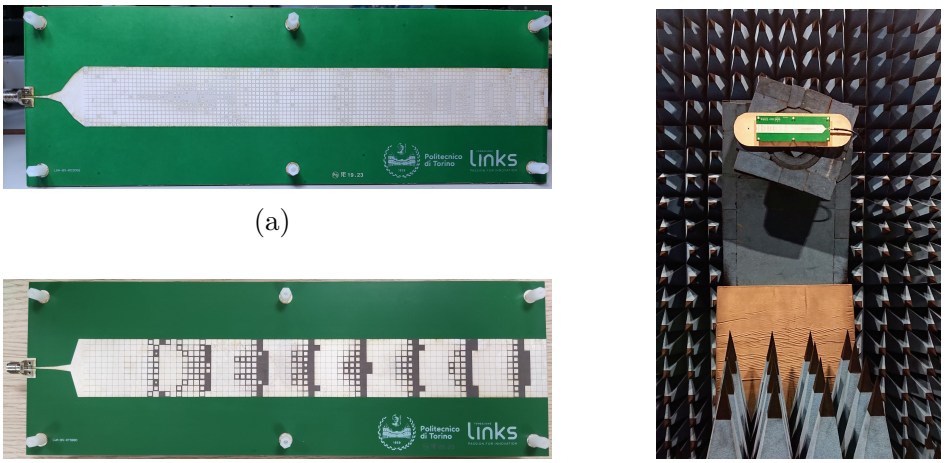

(a) (b) (c)

Figure 4.4: (a) Prototype of the RO3006 design, (b) prototype of the Diclad880 design, (c) measurement setup in the anechoic chamber.

all the degrees of freedom conveyed by the size and position of each patch.

The designed antennas shown in Fig. 4.3 were first simulated with CST; as these results were in very good agreement with those predicted by the design method, prototypes were fabricated for each design and their performance measured in the anechoic chamber of the Antenna Lab at Politecnico di Torino (see Fig. 4.4).

The simulated and measured radiation patterns for the RO3006 and the Diclad880 designs are shown in Figs. 4.5 and 4.6 respectively, together with the mask-type constraints on the desired far field imposed in the synthesis process and the pattern predicted by the design method. In both cases, broadside radiation is achieved as expected, showing excellent agreement with the simulated results. There are some differences in the side lobes between simulated and measured patterns, that may be attributed to inaccuracies in the simulation, due to the high number of mesh cells needed to properly model the structure, and to fabrication tolerances. For the RO3006 design, the side lobes comply with the SLL mask set in the synthesis process, which is not the case for the Diclad880 solution; this may be due to the smaller reactance range achievable with the latter substrate, which translates into fewer degrees of freedom for the control of the side lobe pattern.

To verify the actual suppression of the OSB, the reflection coefficient $S_{11}$ and the realized gain [68] at broadside of the prototypes must be examined. In particular, the peak gains of the prototypes are evaluated using a ridged horn as reference antenna.

The maximum realized gain values for both designs in a 400 MHz-frequency range around the working frequency of 10 GHz are shown in Fig. 4.7, while Table 4.1 lists the directivity, realized gain and $|S_{11}|$ at the central frequency, both simulated and measured, for the considered designs. It can be seen that, at the considered

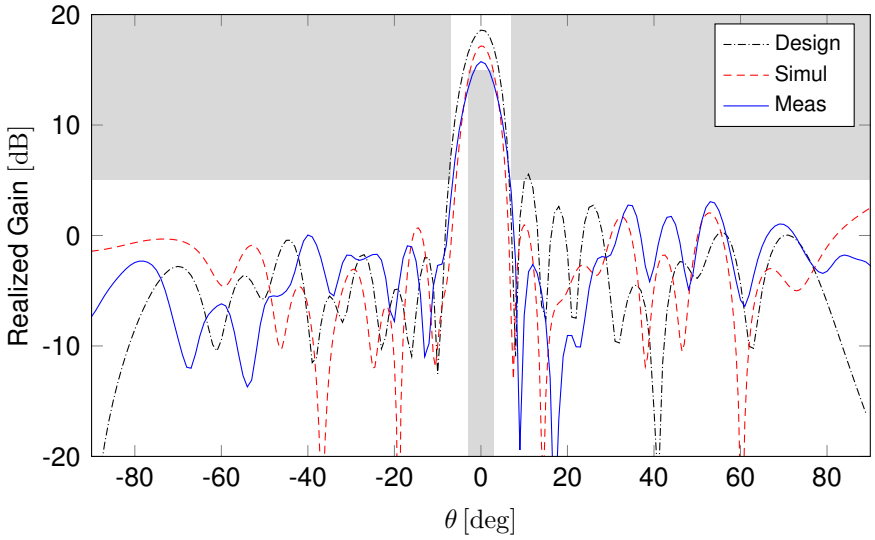


Figure 4.5: Simulated (CST) and measured realized gain pattern for the RO3006 design; the figure also shows the pattern predicted by the design method (that does not consider material losses).

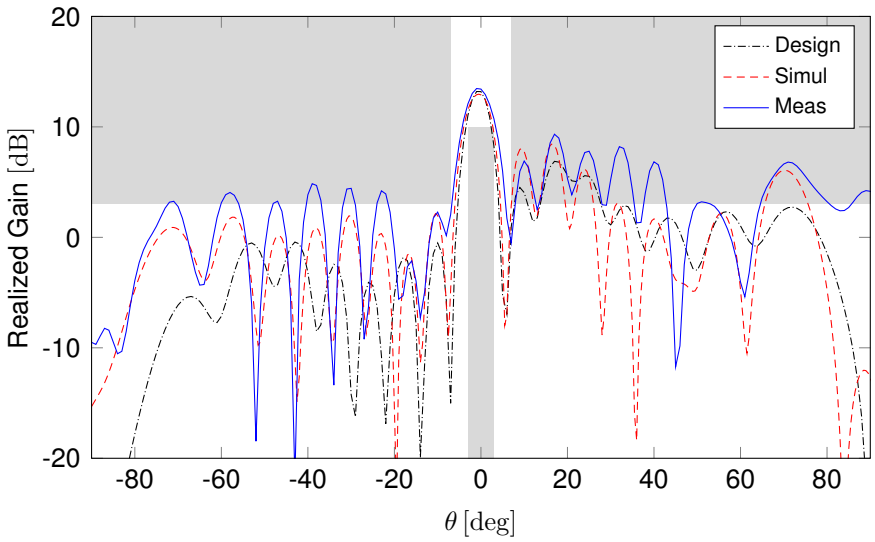


Figure 4.6: Simulated (CST) and measured realized gain pattern for the Diclad880 design; the figure also shows the pattern predicted by the design method (that does not consider material losses).

working frequency of 10 GHz (broadside radiation), the RO3006 and the Diclad880 prototypes achieve a realized gain of 15.7 dB and 13.5 dB, respectively. These values represent a loss of 2.6 dB and 1 dB with respect to the corresponding directivity values; more specifically, the measured realized gain for the RO3006 design is 1.5 dB

Table 4.1: Directivity, realized gain and $|S_{11}|$ at 10 GHz for both designs.

| | Simulated (CST) | | | Measured | | |
|---|---|---|---|---|---|---|
| Substrate | Dir. [dB] | Real. Gain [dB] | $\lvert S_{11}\rvert$ [dB] | Dir. [dB] | Real. Gain [dB] | $\lvert S_{11}\rvert$ [dB] |
| RO3006 | 18.3 | 17.2 | -15.0 | 18.3 | 15.7 | -4.4 |
| Diclad880 | 13.3 | 13.0 | -12.2 | 14.5 | 13.5 | -15.9 |

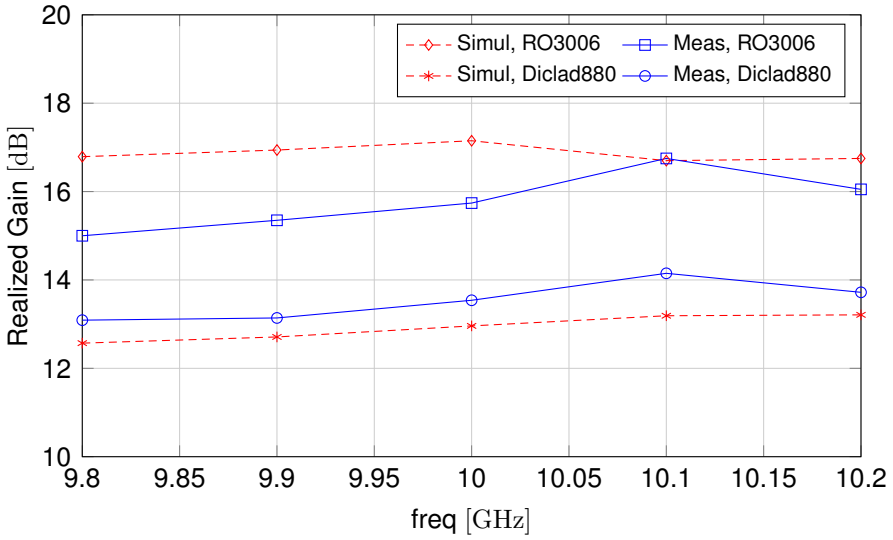


Figure 4.7: Measured realized gain values for the RO3006 and the Diclad880 designs.

lower than the simulated realized gain obtained with CST.

This drop in the realized gain with respect to the simulated one, which happens only for the RO3006 design, can be understood by observing the differences in the reflection coefficients.

Figures 4.8 and 4.9 show the simulated and measured reflection coefficient for the RO3006 and the Diclad880 designs, respectively. The simulated $S_{11}$ for the RO3006 design is way smaller than the measured one; this means that the solution designed with the automated numerical method effectively eliminates the OSB at simulation level, but the fabricated prototype, although radiating at broadside with an acceptable realized gain, shows a poorer behaviour in terms of $S_{11}$. This can be attributed to the RO3006 substrate: this material tends to be anisotropic in reality [86], and this characteristic is not considered in the simulation environment (the authors were unaware of this issue when choosing the substrate). From Fig. 4.8 it can be observed that the measured $S_{11}$ has a minimum at 10.1 GHz; at this frequency (see Fig. 4.10), the main beam is still nearly at broadside (shift of 2°), with a peak realized gain of 16.8 dB (in excellent agreement with the simulated results). This shows some degree of design robustness, especially in view of the more resonant design resulting from the larger permittivity ($\varepsilon_r = 6.5$) of RO3006.

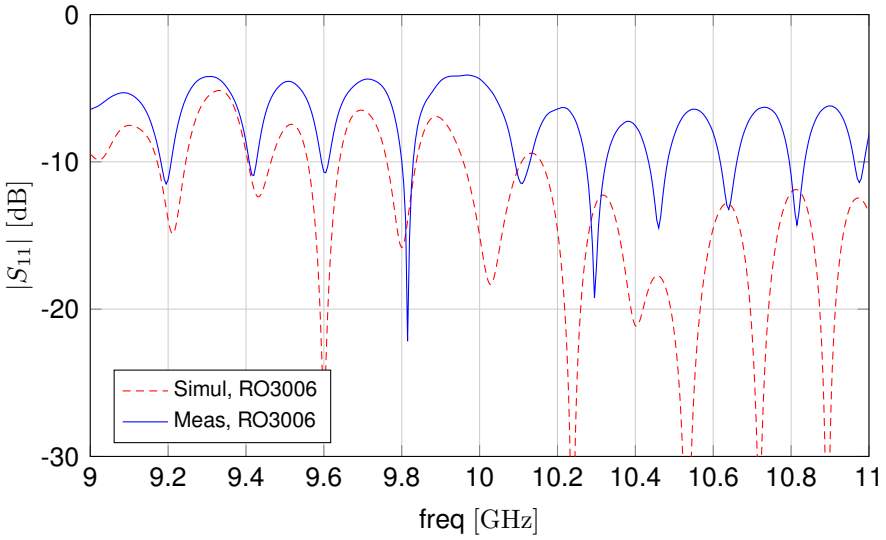


Figure 4.8: Simulated and measured $|S_{11}|$ for the RO3006 design.

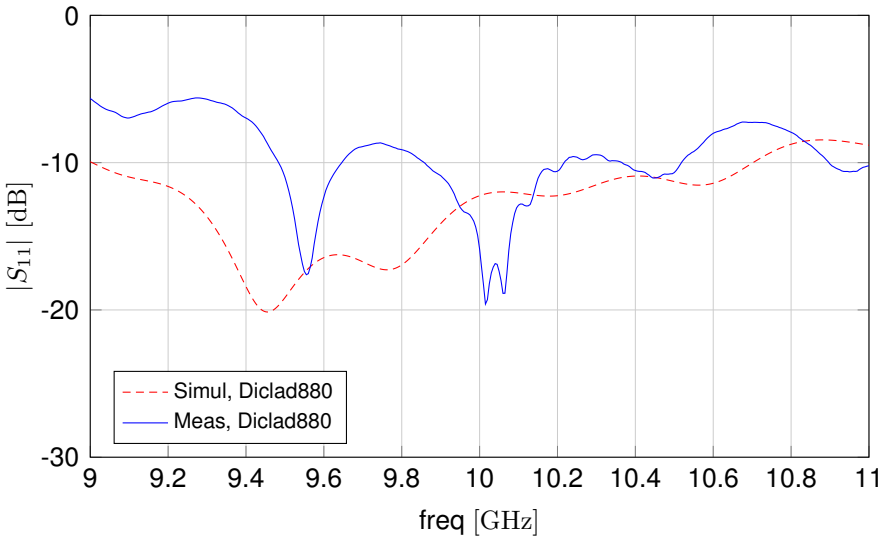


Figure 4.9: Simulated and measured $|S_{11}|$ for the Diclad880 design.

For the prototype built on the Diclad880 substrate ($\varepsilon_r = 2.2$), the measured $S_{11}$ is lower than the simulated one, and this translates into a higher realized gain at broadside.

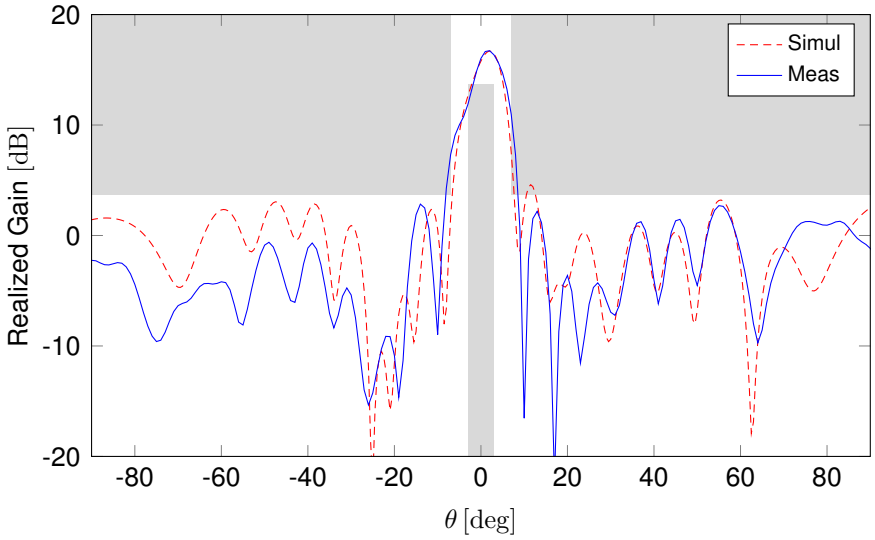


Figure 4.10: Simulated (CST) and measured realized gain pattern for the RO3006 design at 10.1 GHz.

## 4.4 Conclusions

In this Chapter, two broadside-radiating leaky-wave antennas based on different substrates were designed using an automated numerical method for the synthesis of metasurfaces, that does not require any analytical assumption on the impedance pattern and incorporates a realistic model of the feeding structure. Prototypes of the designed antennas were fabricated and measured, and broadside radiation was achieved as expected, thus effectively overcoming the open stopband problem.

# Chapter 5

# Automated Design of Tensor Metasurfaces

This Chapter introduces a preliminary tensor version of the automated design method of Chapter 3.

## 5.1 Introduction

Tensor metasurfaces (MTS) offer more flexibility in the manipulation of electromagnetic waves with respect to their scalar counterpart, thanks to the higher number of degrees of freedom. The majority of methods available in literature for the synthesis of tensor metasurfaces are tailored to sinusoidally modulated MTS antennas [41, 42, 53], that require specific parameterizations.

In this Chapter, the automated design method for the design of MTS antennas described in [6, 40], initially developed to deal with scalar impedances, is modified to accommodate the synthesis of tensor MTSs. The main innovations with respect to the isotropic version of the algorithm presented in Chapter 3 are related to the formulation of the impedance realizability constraints (see Appendix A.2), while the radiated field functional and the PEC condition remain the same.

This Chapter is organized as follows. Section 5.2 illustrates the properties of a realizable tensor impedance, while Section 5.3 introduces a new testing strategy that allows to express the components of the impedance tensor as functions of the current coefficients. Section 5.4 contains the expressions of the new cost functionals and their gradients. Finally, preliminary results regarding the synthesis of a circular antenna radiating a broadside pencil beam are reported in Section 5.5.

## 5.2 Realizable Tensor Impedance

A general tensor impedance can be expressed in terms of four basis dyadics, based on a local orthonormal basis $(\hat{\boldsymbol{u}}, \hat{\boldsymbol{v}})$ [87, 69]:

$$\overline{\overline{\boldsymbol{Z}}} = Z_{\mathrm{I}}\,\overline{\overline{\boldsymbol{I}}} + Z_{\mathrm{N}}\,\overline{\overline{\boldsymbol{N}}} + Z_{\mathrm{K}}\,\overline{\overline{\boldsymbol{K}}} + Z_{\mathrm{L}}\,\overline{\overline{\boldsymbol{L}}}, \tag{5.1}$$

where

$$\overline{\overline{\boldsymbol{I}}} = \hat{\boldsymbol{u}}\hat{\boldsymbol{u}} + \hat{\boldsymbol{v}}\hat{\boldsymbol{v}}, \tag{5.2}$$

$$\overline{\overline{\boldsymbol{N}}} = \hat{\boldsymbol{v}}\hat{\boldsymbol{u}} - \hat{\boldsymbol{u}}\hat{\boldsymbol{v}}, \tag{5.3}$$

$$\overline{\overline{\boldsymbol{K}}} = \hat{\boldsymbol{u}}\hat{\boldsymbol{u}} - \hat{\boldsymbol{v}}\hat{\boldsymbol{v}}, \tag{5.4}$$

$$\overline{\overline{\boldsymbol{L}}} = \hat{\boldsymbol{v}}\hat{\boldsymbol{u}} + \hat{\boldsymbol{u}}\hat{\boldsymbol{v}}. \tag{5.5}$$

As explained in [87, 69], the condition of *passivity* and *losslessness* for a tensor impedance requires

$$\operatorname{Re} Z_{\mathrm{I}} = \operatorname{Im} Z_{\mathrm{N}} = \operatorname{Re} Z_{\mathrm{K}} = \operatorname{Re} Z_{\mathrm{L}} = 0. \tag{5.6}$$

The term $\operatorname{Re} Z_{\mathrm{N}}$ is not required to be zero by the condition of passivity and absence of losses; however, it accounts for bianisotropic effects [69] that in practice would significantly complicate the realization of the unit cells; hence, we also require it to be zero. Therefore, the expression of a passive and lossless tensor impedance becomes

$$\overline{\overline{\boldsymbol{Z}}} = \mathrm{j}X_{\mathrm{I}}\,\overline{\overline{\boldsymbol{I}}} + \mathrm{j}X_{\mathrm{K}}\,\overline{\overline{\boldsymbol{K}}} + \mathrm{j}X_{\mathrm{L}}\,\overline{\overline{\boldsymbol{L}}}. \tag{5.7}$$

In matrix form, the impedance tensor can be written as

$$\mathsf{Z} = \mathrm{j}\begin{bmatrix} X_{uu} & X_{uv} \\ X_{vu} & X_{vv} \end{bmatrix} = \mathrm{j}\begin{bmatrix} X_{\mathrm{I}} + X_{\mathrm{K}} & X_{\mathrm{L}} \\ X_{\mathrm{L}} & X_{\mathrm{I}} - X_{\mathrm{K}} \end{bmatrix}. \tag{5.8}$$

This matrix can be diagonalized as

$$\mathsf{Z}^d = \mathrm{j}\begin{bmatrix} X_1 & 0 \\ 0 & X_2 \end{bmatrix}, \tag{5.9}$$

where

$$X_1 = X_{\mathrm{I}} + \sqrt{X_{\mathrm{K}}^2 + X_{\mathrm{L}}^2}, \tag{5.10}$$

$$X_2 = X_{\mathrm{I}} - \sqrt{X_{\mathrm{K}}^2 + X_{\mathrm{L}}^2}. \tag{5.11}$$

It can be shown that capacitive or inductive behavior is expressed by the sign of these eigenvalues; hence, enforcing unit cells of either type requires enforcing the

sign of the eingenvalue. For example, the most usual capacitive choice implies requiring that both eigenvalues $X_1, X_2$ be negative, i.e.,

$$X_{\mathrm{I}} < -\sqrt{X_{\mathrm{K}}^2 + X_{\mathrm{L}}^2}. \tag{5.12}$$

or, equivalently,

$$X_{\mathrm{I}} < 0, \tag{5.13}$$
$$X_{\mathrm{I}}^2 > X_{\mathrm{K}}^2 + X_{\mathrm{L}}^2. \tag{5.14}$$

These will be the conditions to enforce to ensure that the synthesized impedance profile be realizable with capacitive unit cells; we will discuss later on the bounding of these values.

## 5.3 Retrieval of Tensor Impedance Components

A new testing strategy must be devised to extract all the relevant components of the tensor impedance. The testing is carried out using the bilinear form

$$\langle \boldsymbol{a}, \boldsymbol{b} \rangle = \frac{1}{A_\Sigma} \int_\Sigma \boldsymbol{a} \cdot \boldsymbol{b} \, \mathrm{d}S. \tag{5.15}$$

where $\Sigma$ is a surface of interest (e.g. of the unit cell), and $A_\Sigma$ is its area. Let's consider the general realizable IBC equation

$$\boldsymbol{E} = \overline{\overline{\boldsymbol{Z}}} \cdot \boldsymbol{J} = \left( \mathrm{j}X_{\mathrm{I}} \, \overline{\overline{\boldsymbol{I}}} + \mathrm{j}X_{\mathrm{K}} \, \overline{\overline{\boldsymbol{K}}} + \mathrm{j}X_{\mathrm{L}} \, \overline{\overline{\boldsymbol{L}}} \right) \cdot \boldsymbol{J}. \tag{5.16}$$

This equation can be tested along four different directions, given by the scalar product of every basis dyadic and the complex conjugate of the current density $\boldsymbol{J}^*$:

$$\langle \overline{\overline{\boldsymbol{I}}} \cdot \boldsymbol{J}^*, \overline{\overline{\boldsymbol{Z}}} \cdot \boldsymbol{J} \rangle = \langle \overline{\overline{\boldsymbol{I}}} \cdot \boldsymbol{J}^*, \boldsymbol{E} \rangle \to \langle \boldsymbol{J}^* \cdot \overline{\overline{\boldsymbol{I}}}, \overline{\overline{\boldsymbol{Z}}} \cdot \boldsymbol{J} \rangle = \langle \boldsymbol{J}^* \cdot \overline{\overline{\boldsymbol{I}}}, \boldsymbol{E} \rangle, \tag{5.17}$$
$$\langle \overline{\overline{\boldsymbol{N}}} \cdot \boldsymbol{J}^*, \overline{\overline{\boldsymbol{Z}}} \cdot \boldsymbol{J} \rangle = \langle \overline{\overline{\boldsymbol{N}}} \cdot \boldsymbol{J}^*, \boldsymbol{E} \rangle \to \langle -\boldsymbol{J}^* \cdot \overline{\overline{\boldsymbol{N}}}, \overline{\overline{\boldsymbol{Z}}} \cdot \boldsymbol{J} \rangle = \langle -\boldsymbol{J}^* \cdot \overline{\overline{\boldsymbol{N}}}, \boldsymbol{E} \rangle, \tag{5.18}$$
$$\langle \overline{\overline{\boldsymbol{K}}} \cdot \boldsymbol{J}^*, \overline{\overline{\boldsymbol{Z}}} \cdot \boldsymbol{J} \rangle = \langle \overline{\overline{\boldsymbol{K}}} \cdot \boldsymbol{J}^*, \boldsymbol{E} \rangle \to \langle \boldsymbol{J}^* \cdot \overline{\overline{\boldsymbol{K}}}, \overline{\overline{\boldsymbol{Z}}} \cdot \boldsymbol{J} \rangle = \langle \boldsymbol{J}^* \cdot \overline{\overline{\boldsymbol{K}}}, \boldsymbol{E} \rangle, \tag{5.19}$$
$$\langle \overline{\overline{\boldsymbol{L}}} \cdot \boldsymbol{J}^*, \overline{\overline{\boldsymbol{Z}}} \cdot \boldsymbol{J} \rangle = \langle \overline{\overline{\boldsymbol{L}}} \cdot \boldsymbol{J}^*, \boldsymbol{E} \rangle \to \langle \boldsymbol{J}^* \cdot \overline{\overline{\boldsymbol{L}}}, \overline{\overline{\boldsymbol{Z}}} \cdot \boldsymbol{J} \rangle = \langle \boldsymbol{J}^* \cdot \overline{\overline{\boldsymbol{L}}}, \boldsymbol{E} \rangle. \tag{5.20}$$

Given that

$$\overline{\overline{\boldsymbol{I}}} \cdot \overline{\overline{\boldsymbol{I}}} = \overline{\overline{\boldsymbol{I}}}, \quad \overline{\overline{\boldsymbol{I}}} \cdot \overline{\overline{\boldsymbol{N}}} = \overline{\overline{\boldsymbol{N}}}, \quad \overline{\overline{\boldsymbol{I}}} \cdot \overline{\overline{\boldsymbol{K}}} = \overline{\overline{\boldsymbol{K}}}, \quad \overline{\overline{\boldsymbol{I}}} \cdot \overline{\overline{\boldsymbol{L}}} = \overline{\overline{\boldsymbol{L}}}, \tag{5.21}$$
$$\overline{\overline{\boldsymbol{N}}} \cdot \overline{\overline{\boldsymbol{I}}} = \overline{\overline{\boldsymbol{N}}}, \quad \overline{\overline{\boldsymbol{N}}} \cdot \overline{\overline{\boldsymbol{N}}} = -\overline{\overline{\boldsymbol{I}}}, \quad \overline{\overline{\boldsymbol{N}}} \cdot \overline{\overline{\boldsymbol{K}}} = \overline{\overline{\boldsymbol{L}}}, \quad \overline{\overline{\boldsymbol{N}}} \cdot \overline{\overline{\boldsymbol{L}}} = -\overline{\overline{\boldsymbol{K}}}, \tag{5.22}$$
$$\overline{\overline{\boldsymbol{K}}} \cdot \overline{\overline{\boldsymbol{I}}} = \overline{\overline{\boldsymbol{K}}}, \quad \overline{\overline{\boldsymbol{K}}} \cdot \overline{\overline{\boldsymbol{N}}} = -\overline{\overline{\boldsymbol{L}}}, \quad \overline{\overline{\boldsymbol{K}}} \cdot \overline{\overline{\boldsymbol{K}}} = \overline{\overline{\boldsymbol{I}}}, \quad \overline{\overline{\boldsymbol{K}}} \cdot \overline{\overline{\boldsymbol{L}}} = -\overline{\overline{\boldsymbol{N}}}, \tag{5.23}$$
$$\overline{\overline{\boldsymbol{L}}} \cdot \overline{\overline{\boldsymbol{I}}} = \overline{\overline{\boldsymbol{L}}}, \quad \overline{\overline{\boldsymbol{L}}} \cdot \overline{\overline{\boldsymbol{N}}} = \overline{\overline{\boldsymbol{K}}}, \quad \overline{\overline{\boldsymbol{L}}} \cdot \overline{\overline{\boldsymbol{K}}} = \overline{\overline{\boldsymbol{N}}}, \quad \overline{\overline{\boldsymbol{L}}} \cdot \overline{\overline{\boldsymbol{L}}} = \overline{\overline{\boldsymbol{I}}}, \tag{5.24}$$

one obtains

$$\overline{\overline{\boldsymbol{I}}} \cdot \overline{\overline{\boldsymbol{Z}}} = \mathrm{j}X_{\mathrm{I}}\,\overline{\overline{\boldsymbol{I}}} + \mathrm{j}X_{\mathrm{K}}\,\overline{\overline{\boldsymbol{K}}} + \mathrm{j}X_{\mathrm{L}}\,\overline{\overline{\boldsymbol{L}}}, \tag{5.25}$$

$$\overline{\overline{\boldsymbol{N}}} \cdot \overline{\overline{\boldsymbol{Z}}} = \mathrm{j}X_{\mathrm{I}}\,\overline{\overline{\boldsymbol{N}}} + \mathrm{j}X_{\mathrm{K}}\,\overline{\overline{\boldsymbol{L}}} - \mathrm{j}X_{\mathrm{L}}\,\overline{\overline{\boldsymbol{K}}}, \tag{5.26}$$

$$\overline{\overline{\boldsymbol{K}}} \cdot \overline{\overline{\boldsymbol{Z}}} = \mathrm{j}X_{\mathrm{I}}\,\overline{\overline{\boldsymbol{K}}} + \mathrm{j}X_{\mathrm{K}}\,\overline{\overline{\boldsymbol{I}}} - \mathrm{j}X_{\mathrm{L}}\,\overline{\overline{\boldsymbol{N}}}, \tag{5.27}$$

$$\overline{\overline{\boldsymbol{L}}} \cdot \overline{\overline{\boldsymbol{Z}}} = \mathrm{j}X_{\mathrm{I}}\,\overline{\overline{\boldsymbol{L}}} + \mathrm{j}X_{\mathrm{K}}\,\overline{\overline{\boldsymbol{N}}} + \mathrm{j}X_{\mathrm{L}}\,\overline{\overline{\boldsymbol{I}}}, \tag{5.28}$$

and (5.17)-(5.20) become:

$$\mathrm{j}X_{\mathrm{I}} \langle \boldsymbol{J}^*, \overline{\overline{\boldsymbol{I}}} \cdot \boldsymbol{J} \rangle + \mathrm{j}X_{\mathrm{K}} \langle \boldsymbol{J}^*, \overline{\overline{\boldsymbol{K}}} \cdot \boldsymbol{J} \rangle + \mathrm{j}X_{\mathrm{L}} \langle \boldsymbol{J}^*, \overline{\overline{\boldsymbol{L}}} \cdot \boldsymbol{J} \rangle = \langle \boldsymbol{J}^*, \overline{\overline{\boldsymbol{I}}} \cdot \boldsymbol{E} \rangle, \tag{5.29}$$

$$\mathrm{j}X_{\mathrm{I}} \langle \boldsymbol{J}^*, \overline{\overline{\boldsymbol{N}}} \cdot \boldsymbol{J} \rangle + \mathrm{j}X_{\mathrm{K}} \langle \boldsymbol{J}^*, \overline{\overline{\boldsymbol{L}}} \cdot \boldsymbol{J} \rangle - \mathrm{j}X_{\mathrm{L}} \langle \boldsymbol{J}^*, \overline{\overline{\boldsymbol{K}}} \cdot \boldsymbol{J} \rangle = \langle \boldsymbol{J}^*, \overline{\overline{\boldsymbol{N}}} \cdot \boldsymbol{E} \rangle, \tag{5.30}$$

$$\mathrm{j}X_{\mathrm{I}} \langle \boldsymbol{J}^*, \overline{\overline{\boldsymbol{K}}} \cdot \boldsymbol{J} \rangle + \mathrm{j}X_{\mathrm{K}} \langle \boldsymbol{J}^*, \overline{\overline{\boldsymbol{I}}} \cdot \boldsymbol{J} \rangle - \mathrm{j}X_{\mathrm{L}} \langle \boldsymbol{J}^*, \overline{\overline{\boldsymbol{N}}} \cdot \boldsymbol{J} \rangle = \langle \boldsymbol{J}^*, \overline{\overline{\boldsymbol{K}}} \cdot \boldsymbol{E} \rangle, \tag{5.31}$$

$$\mathrm{j}X_{\mathrm{I}} \langle \boldsymbol{J}^*, \overline{\overline{\boldsymbol{L}}} \cdot \boldsymbol{J} \rangle + \mathrm{j}X_{\mathrm{K}} \langle \boldsymbol{J}^*, \overline{\overline{\boldsymbol{N}}} \cdot \boldsymbol{J} \rangle + \mathrm{j}X_{\mathrm{L}} \langle \boldsymbol{J}^*, \overline{\overline{\boldsymbol{I}}} \cdot \boldsymbol{J} \rangle = \langle \boldsymbol{J}^*, \overline{\overline{\boldsymbol{L}}} \cdot \boldsymbol{E} \rangle. \tag{5.32}$$

Expressing $\boldsymbol{J}$ and $\boldsymbol{E}$ in the local basis $(\hat{\boldsymbol{u}}, \hat{\boldsymbol{v}})$,

$$\boldsymbol{J} = J_u \hat{\boldsymbol{u}} + J_v \hat{\boldsymbol{v}}, \tag{5.33}$$

$$\boldsymbol{E} = E_u \hat{\boldsymbol{u}} + E_v \hat{\boldsymbol{v}}, \tag{5.34}$$

and recalling (5.2)-(5.5), the following quantities can be defined:

$$\mu_{\mathrm{I}} = \langle \boldsymbol{J}^*, \overline{\overline{\boldsymbol{I}}} \cdot \boldsymbol{J} \rangle = |J_u|^2 + |J_v|^2, \tag{5.35}$$

$$\mu_{\mathrm{N}} = \langle \boldsymbol{J}^*, \overline{\overline{\boldsymbol{N}}} \cdot \boldsymbol{J} \rangle = -J_u^* J_v + J_u J_v^* = 2\mathrm{j}\,\mathrm{Im}(J_u J_v^*), \tag{5.36}$$

$$\mu_{\mathrm{K}} = \langle \boldsymbol{J}^*, \overline{\overline{\boldsymbol{K}}} \cdot \boldsymbol{J} \rangle = |J_u|^2 - |J_v|^2, \tag{5.37}$$

$$\mu_{\mathrm{L}} = \langle \boldsymbol{J}^*, \overline{\overline{\boldsymbol{L}}} \cdot \boldsymbol{J} \rangle = J_u^* J_v + J_u J_v^* = 2\,\mathrm{Re}(J_u J_v^*), \tag{5.38}$$

$$S_{\mathrm{I}} = \langle \boldsymbol{J}^*, \overline{\overline{\boldsymbol{I}}} \cdot \boldsymbol{E} \rangle = J_u^* E_u + J_v^* E_v, \tag{5.39}$$

$$S_{\mathrm{N}} = \langle \boldsymbol{J}^*, \overline{\overline{\boldsymbol{N}}} \cdot \boldsymbol{E} \rangle = -J_u^* E_v + J_v^* E_u, \tag{5.40}$$

$$S_{\mathrm{K}} = \langle \boldsymbol{J}^*, \overline{\overline{\boldsymbol{K}}} \cdot \boldsymbol{E} \rangle = J_u^* E_u - J_v^* E_v, \tag{5.41}$$

$$S_{\mathrm{L}} = \langle \boldsymbol{J}^*, \overline{\overline{\boldsymbol{L}}} \cdot \boldsymbol{E} \rangle = J_u^* E_v + J_v^* E_u. \tag{5.42}$$

where all $J$ and $E$ quantities above are intended as averages over the chosen surface $\Sigma$. Now, (5.29)-(5.32) can be compactly written as

$$\mathrm{j}X_{\mathrm{I}}\,\mu_{\mathrm{I}} + \mathrm{j}X_{\mathrm{K}}\,\mu_{\mathrm{K}} + \mathrm{j}X_{\mathrm{L}}\,\mu_{\mathrm{L}} = S_{\mathrm{I}}, \tag{5.43}$$

$$\mathrm{j}X_{\mathrm{I}}\,\mu_{\mathrm{N}} + \mathrm{j}X_{\mathrm{K}}\,\mu_{\mathrm{L}} - \mathrm{j}X_{\mathrm{L}}\,\mu_{\mathrm{K}} = S_{\mathrm{N}}, \tag{5.44}$$

$$\mathrm{j}X_{\mathrm{I}}\,\mu_{\mathrm{K}} + \mathrm{j}X_{\mathrm{K}}\,\mu_{\mathrm{I}} - \mathrm{j}X_{\mathrm{L}}\,\mu_{\mathrm{N}} = S_{\mathrm{K}}, \tag{5.45}$$

$$\mathrm{j}X_{\mathrm{I}}\,\mu_{\mathrm{L}} + \mathrm{j}X_{\mathrm{K}}\,\mu_{\mathrm{N}} + \mathrm{j}X_{\mathrm{L}}\,\mu_{\mathrm{I}} = S_{\mathrm{L}}. \tag{5.46}$$

From (5.35)-(5.38) it can be observed that the quantities $\mu_{\mathrm{I}}$, $\mu_{\mathrm{K}}$ and $\mu_{\mathrm{L}}$ are real, while $\mu_{\mathrm{N}}$ is purely imaginary. Keeping this in mind, (5.43)-(5.46) can be decomposed in real and imaginary parts as follows:

$$X_{\mathrm{I}}\,\mu_{\mathrm{I}} + X_{\mathrm{K}}\,\mu_{\mathrm{K}} + X_{\mathrm{L}}\,\mu_{\mathrm{L}} = \mathrm{Im}\,S_{\mathrm{I}}, \tag{5.47}$$
$$0 = \mathrm{Re}\,S_{\mathrm{I}}, \tag{5.48}$$
$$X_{\mathrm{K}}\,\mu_{\mathrm{L}} - X_{\mathrm{L}}\,\mu_{\mathrm{K}} = \mathrm{Im}\,S_{\mathrm{N}}, \tag{5.49}$$
$$-X_{\mathrm{I}}\,\mathrm{Im}\,\mu_{\mathrm{N}} = \mathrm{Re}\,S_{\mathrm{N}}, \tag{5.50}$$
$$X_{\mathrm{I}}\,\mu_{\mathrm{K}} + X_{\mathrm{K}}\,\mu_{\mathrm{I}} = \mathrm{Im}\,S_{\mathrm{K}}, \tag{5.51}$$
$$X_{\mathrm{L}}\,\mathrm{Im}\,\mu_{\mathrm{N}} = \mathrm{Re}\,S_{\mathrm{K}} \tag{5.52}$$
$$X_{\mathrm{I}}\,\mu_{\mathrm{L}} + X_{\mathrm{L}}\,\mu_{\mathrm{I}} = \mathrm{Im}\,S_{\mathrm{L}}, \tag{5.53}$$
$$-X_{\mathrm{K}}\,\mathrm{Im}\,\mu_{\mathrm{N}} = \mathrm{Re}\,S_{\mathrm{L}}. \tag{5.54}$$

In the above, (5.48) expresses the condition of passivity and losslessness:

$$\mathrm{Re}\,(\boldsymbol{J}^{*}\cdot\boldsymbol{E}) = 0. \tag{5.55}$$

Assuming this condition is satisfied during the optimization process, what remains is 7 useful equations for 3 unknowns. This system is clearly overdetermined; a subset of equations is therefore sufficient to retrieve the 3 components of the impedance tensor. In particular, selecting (5.50), (5.54) and (5.52), a diagonal system is obtained:

$$\begin{bmatrix} -\mathrm{Im}\,\mu_{\mathrm{N}} & 0 & 0 \\ 0 & -\mathrm{Im}\,\mu_{\mathrm{N}} & 0 \\ 0 & 0 & \mathrm{Im}\,\mu_{\mathrm{N}} \end{bmatrix} \begin{bmatrix} X_{\mathrm{I}} \\ X_{\mathrm{K}} \\ X_{\mathrm{L}} \end{bmatrix} = \begin{bmatrix} \mathrm{Re}\,S_{\mathrm{N}} \\ \mathrm{Re}\,S_{\mathrm{L}} \\ \mathrm{Re}\,S_{\mathrm{K}} \end{bmatrix}. \tag{5.56}$$

Finally,

$$X_{\mathrm{I}} = -\frac{\mathrm{Re}\,S_{\mathrm{N}}}{\mathrm{Im}\,\mu_{\mathrm{N}}}, \tag{5.57}$$
$$X_{\mathrm{K}} = -\frac{\mathrm{Re}\,S_{\mathrm{L}}}{\mathrm{Im}\,\mu_{\mathrm{N}}}, \tag{5.58}$$
$$X_{\mathrm{L}} = \frac{\mathrm{Re}\,S_{\mathrm{K}}}{\mathrm{Im}\,\mu_{\mathrm{N}}}. \tag{5.59}$$

These results will be important to enforce the condition of capacitive tensor impedance in terms of current coefficients only, as shown in Sec. 5.4. It is interesting to notice that another system can be derived from (5.47)-(5.54), if (5.47), (5.51) and (5.53) are chosen:

$$\begin{bmatrix} \mu_{\mathrm{I}} & \mu_{\mathrm{K}} & \mu_{\mathrm{L}} \\ \mu_{\mathrm{K}} & \mu_{\mathrm{I}} & 0 \\ \mu_{\mathrm{L}} & 0 & \mu_{\mathrm{I}} \end{bmatrix} \begin{bmatrix} X_{\mathrm{I}} \\ X_{\mathrm{K}} \\ X_{\mathrm{L}} \end{bmatrix} = \begin{bmatrix} \mathrm{Im}\,S_{\mathrm{I}} \\ \mathrm{Im}\,S_{\mathrm{K}} \\ \mathrm{Im}\,S_{\mathrm{L}} \end{bmatrix}. \tag{5.60}$$

Inverting (5.60), one obtains:

$$X_{\mathrm{I}} = \frac{\mu_{\mathrm{I}} \operatorname{Im} S_{\mathrm{I}} - \mu_{\mathrm{K}} \operatorname{Im} S_{\mathrm{K}} - \mu_{\mathrm{L}} \operatorname{Im} S_{\mathrm{L}}}{\mu_{\mathrm{I}}^2 - \mu_{\mathrm{K}}^2 - \mu_{\mathrm{L}}^2}, \tag{5.61}$$

$$X_{\mathrm{K}} = \frac{-\mu_{\mathrm{K}} \operatorname{Im} S_{\mathrm{I}} + \mu_{\mathrm{I}} \operatorname{Im} S_{\mathrm{K}} + \mu_{\mathrm{L}}/\mu_{\mathrm{I}}(\mu_{\mathrm{K}} \operatorname{Im} S_{\mathrm{L}} - \mu_{\mathrm{L}} \operatorname{Im} S_{\mathrm{K}})}{\mu_{\mathrm{I}}^2 - \mu_{\mathrm{K}}^2 - \mu_{\mathrm{L}}^2}, \tag{5.62}$$

$$X_{\mathrm{L}} = \frac{-\mu_{\mathrm{L}} \operatorname{Im} S_{\mathrm{I}} + \mu_{\mathrm{I}} \operatorname{Im} S_{\mathrm{L}} + \mu_{\mathrm{K}}/\mu_{\mathrm{I}}(\mu_{\mathrm{L}} \operatorname{Im} S_{\mathrm{K}} - \mu_{\mathrm{K}} \operatorname{Im} S_{\mathrm{L}})}{\mu_{\mathrm{I}}^2 - \mu_{\mathrm{K}}^2 - \mu_{\mathrm{L}}^2}. \tag{5.63}$$

These equations offer an alternative for the retrieval of $X_{\mathrm{I}}$, $X_{\mathrm{K}}$ and $X_{\mathrm{L}}$ with respect to the diagonal system (5.56).

## 5.4 Enforcement of Realizability Constraints

As explained in [6, 40], in order to exploit the advantages in terms of efficiency of a current-based optimization algorithm, all cost functionals must be expressed in terms of current coefficients only. Regarding the IBC constraints, the requirement for passivity and losslessness is maintained from the scalar version of the automated design method (see Chapter 3), while new constraints must be enforced involving $X_{\mathrm{I}}$, $X_{\mathrm{K}}$ and $X_{\mathrm{L}}$.

This enforcement is based on the relationships between the tensor impedance quantities and the fields involved in the optimization process ($\boldsymbol{J}$ and $\boldsymbol{E}$). It is advantageous to limit the polynomial order of the functionals to fourth, which allows a closed-form line search. Hence, we will employ the diagonal version (5.57)-(5.59) of such relationships.

Specifically, the realizability constraints aim at ensuring that the synthesizable impedance profile can be implemented using capacitive unit cells, as mentioned in Sec. 5.2. Assuming lower and upper bound values for $X_{\mathrm{I}}$, these constraints will be:

$$X_{\min} < X_{\mathrm{I}} < X_{\max}, \tag{5.64}$$

$$X_{\mathrm{I}}^2 > X_{\mathrm{K}}^2 + X_{\mathrm{L}}^2, \tag{5.65}$$

with $X_{\min} < X_{\max} < 0$. Using (5.57)-(5.59), they can be equivalently written as

$$-X_{\max} \operatorname{Im} \mu_{\mathrm{N}} < \operatorname{Re} S_{\mathrm{N}} < -X_{\min} \operatorname{Im} \mu_{\mathrm{N}}, \tag{5.66}$$

$$(\operatorname{Re} S_{\mathrm{N}})^2 > (\operatorname{Re} S_{\mathrm{K}})^2 + (\operatorname{Re} S_{\mathrm{L}})^2. \tag{5.67}$$

These conditions must be enforced in the average sense over each triangular mesh

cell (see App. A). The following cell-wise terms are defined:

$$P_i = \mathrm{Re}\, S_{\mathrm{I}i} = \frac{1}{A_i} \mathrm{Re} \iint_{\mathcal{S}_i} \boldsymbol{J}^* \cdot \overline{\overline{\boldsymbol{I}}} \cdot \boldsymbol{E}\, \mathrm{d}S = \mathrm{Re}\,(\mathsf{I}^{\mathsf{H}} \boldsymbol{\Gamma}_i \mathsf{V}), \tag{5.68}$$

$$Q_i = \mathrm{Im}\, S_{\mathrm{I}i} = \frac{1}{A_i} \mathrm{Im} \iint_{\mathcal{S}_i} \boldsymbol{J}^* \cdot \overline{\overline{\boldsymbol{I}}} \cdot \boldsymbol{E}\, \mathrm{d}S = \mathrm{Im}\,(\mathsf{I}^{\mathsf{H}} \boldsymbol{\Gamma}_i \mathsf{V}), \tag{5.69}$$

$$P_{\mathrm{N}i} = \mathrm{Re}\, S_{\mathrm{N}i} = \frac{1}{A_i} \mathrm{Re} \iint_{\mathcal{S}_i} \boldsymbol{J}^* \cdot \overline{\overline{\boldsymbol{N}}} \cdot \boldsymbol{E}\, \mathrm{d}S = \mathrm{Re}\,(\mathsf{I}^{\mathsf{H}} \boldsymbol{\Gamma}^i_{\mathrm{N}} \mathsf{V}), \tag{5.70}$$

$$P_{\mathrm{K}i} = \mathrm{Re}\, S_{\mathrm{K}i} = \frac{1}{A_i} \mathrm{Re} \iint_{\mathcal{S}_i} \boldsymbol{J}^* \cdot \overline{\overline{\boldsymbol{K}}} \cdot \boldsymbol{E}\, \mathrm{d}S = \mathrm{Re}\,(\mathsf{I}^{\mathsf{H}} \boldsymbol{\Gamma}^i_{\mathrm{K}} \mathsf{V}), \tag{5.71}$$

$$Q_{\mathrm{K}i} = \mathrm{Im}\, S_{\mathrm{K}i} = \frac{1}{A_i} \mathrm{Im} \iint_{\mathcal{S}_i} \boldsymbol{J}^* \cdot \overline{\overline{\boldsymbol{K}}} \cdot \boldsymbol{E}\, \mathrm{d}S = \mathrm{Im}\,(\mathsf{I}^{\mathsf{H}} \boldsymbol{\Gamma}^i_{\mathrm{K}} \mathsf{V}), \tag{5.72}$$

$$P_{\mathrm{L}i} = \mathrm{Re}\, S_{\mathrm{L}i} = \frac{1}{A_i} \mathrm{Re} \iint_{\mathcal{S}_i} \boldsymbol{J}^* \cdot \overline{\overline{\boldsymbol{L}}} \cdot \boldsymbol{E}\, \mathrm{d}S = \mathrm{Re}(\mathsf{I}^{\mathsf{H}} \boldsymbol{\Gamma}^i_{\mathrm{L}} \mathsf{V}), \tag{5.73}$$

$$Q_{\mathrm{L}i} = \mathrm{Im}\, S_{\mathrm{L}i} = \frac{1}{A_i} \mathrm{Im} \iint_{\mathcal{S}_i} \boldsymbol{J}^* \cdot \overline{\overline{\boldsymbol{L}}} \cdot \boldsymbol{E}\, \mathrm{d}S = \mathrm{Im}\,(\mathsf{I}^{\mathsf{H}} \boldsymbol{\Gamma}^i_{\mathrm{L}} \mathsf{V}), \tag{5.74}$$

$$\mathcal{J}_i = \mu_{\mathrm{I}i} = \frac{1}{A_i} \iint_{\mathcal{S}_i} \boldsymbol{J}^* \cdot \overline{\overline{\boldsymbol{I}}} \cdot \boldsymbol{J}\, \mathrm{d}S = \mathsf{I}^{\mathsf{H}} \boldsymbol{\Gamma}_i \mathsf{I}, \tag{5.75}$$

$$\mathcal{J}_{\mathrm{N}i} = \mathrm{Im}\, \mu_{\mathrm{N}i} = \frac{1}{A_i} \mathrm{Im} \iint_{\mathcal{S}_i} \boldsymbol{J}^* \cdot \overline{\overline{\boldsymbol{N}}} \cdot \boldsymbol{J}\, \mathrm{d}S = \mathrm{Im}(\mathsf{I}^{\mathsf{H}} \boldsymbol{\Gamma}^i_{\mathrm{N}} \mathsf{I}), \tag{5.76}$$

$$\mathcal{J}_{\mathrm{K}i} = \mu_{\mathrm{K}i} = \frac{1}{A_i} \iint_{\mathcal{S}_i} \boldsymbol{J}^* \cdot \overline{\overline{\boldsymbol{K}}} \cdot \boldsymbol{J}\, \mathrm{d}S = \mathsf{I}^{\mathsf{H}} \boldsymbol{\Gamma}^i_{\mathrm{K}} \mathsf{I}, \tag{5.77}$$

$$\mathcal{J}_{\mathrm{L}i} = \mu_{\mathrm{L}i} = \frac{1}{A_i} \iint_{\mathcal{S}_i} \boldsymbol{J}^* \cdot \overline{\overline{\boldsymbol{L}}} \cdot \boldsymbol{J}\, \mathrm{d}S = \mathsf{I}^{\mathsf{H}} \boldsymbol{\Gamma}^i_{\mathrm{L}} \mathsf{I}, \tag{5.78}$$

where $\boldsymbol{\Gamma}^i_{\mathrm{T}} \in \mathbb{R}^{N \times N}$, $\mathrm{T} = \mathrm{N}, \mathrm{K}, \mathrm{L}$ is the (averaging) local *mixed* Gram matrix for the $i$-th cell, defined as

$$(\boldsymbol{\Gamma}^i_{\mathrm{T}})_{mn} = \frac{1}{A_i} \iint_{\mathcal{S}_i} \boldsymbol{\Lambda}_m(\boldsymbol{r}) \cdot \overline{\overline{\boldsymbol{T}}} \cdot \boldsymbol{\Lambda}_n(\boldsymbol{r})\, \mathrm{d}\boldsymbol{r}. \tag{5.79}$$

The total realizability cost function for the IBC now becomes:

$$f_{\mathrm{ibc}} = \sum_i w^{\mathrm{act}}_i \rho^{\mathrm{act}}_i + \sum_i w^{\mathrm{imp}}_{\mathrm{L}i} \rho^{\mathrm{imp}}_{\mathrm{L}i} + \sum_i w^{\mathrm{imp}}_{\mathrm{U}i} \rho^{\mathrm{imp}}_{\mathrm{U}i} + \sum_i w^{\mathrm{imp}}_{\mathrm{A}i} \rho^{\mathrm{imp}}_{\mathrm{A}i}, \tag{5.80}$$

where

$$\rho^{\mathrm{act}}_i = P_i^2 \tag{5.81}$$

$$\rho^{\mathrm{imp}}_{\mathrm{L}i} = \mathrm{r}^2(\Psi^{\mathrm{imp}}_{\mathrm{L}i}), \quad \Psi^{\mathrm{imp}}_{\mathrm{L}i} = P_{\mathrm{N}i} + X_{\min} \mathcal{J}_{\mathrm{N}i}, \tag{5.82}$$

$$\rho^{\mathrm{imp}}_{\mathrm{U}i} = \mathrm{r}^2(\Psi^{\mathrm{imp}}_{\mathrm{U}i}), \quad \Psi^{\mathrm{imp}}_{\mathrm{U}i} = -P_{\mathrm{N}i} - X_{\max} \mathcal{J}_{\mathrm{N}i}, \tag{5.83}$$

$$\rho^{\mathrm{imp}}_{\mathrm{A}i} = \mathrm{r}(\Psi^{\mathrm{imp}}_{\mathrm{A}i}), \quad \Psi^{\mathrm{imp}}_{\mathrm{A}i} = P^2_{\mathrm{K}i} + P^2_{\mathrm{L}i} - P^2_{\mathrm{N}i}. \tag{5.84}$$

In the above expressions, $\mathrm{r}(x) = \max(x,0)$ is the ramp function. The functional $\rho_{\mathrm{A}i}^{\mathrm{imp}}$, which is used to enforce that an anisotropic unit cell be capacitive, does not contain a *squared* ramp function, unlike the other functionals expressing inequalities. This choice is made because using the squared ramp would transform this functional in a eighth-degree polynomial in the current coefficients, and despite the regularity of the squared ramp (continuous with continuous first derivative), it is advantageous to keep all polynomials of degree four in order to limit the number of possible local minima and perform the line search in closed-form [69].

Finally, the gradients of the newly defined functionals can be computed as:

$$\tilde{\nabla}\rho_{\mathrm{L}i}^{\mathrm{imp}} = \mathrm{r}(\Psi_{\mathrm{L}i}^{\mathrm{imp}})\,(\boldsymbol{\nu}_{\mathrm{N}i} - (\mathrm{j}2X_{\min}\mathbf{1} + \mathbf{K}^{\mathsf{H}})\,\boldsymbol{\iota}_{\mathrm{N}i}), \tag{5.85}$$

$$\tilde{\nabla}\rho_{\mathrm{U}i}^{\mathrm{imp}} = \mathrm{r}(\Psi_{\mathrm{U}i}^{\mathrm{imp}})\,(-\boldsymbol{\nu}_{\mathrm{N}i} + (\mathbf{K}^{\mathsf{H}} + \mathrm{j}2X_{\max}\mathbf{1})\,\boldsymbol{\iota}_{\mathrm{N}i}), \tag{5.86}$$

$$\tilde{\nabla}\rho_{\mathrm{A}i}^{\mathrm{imp}} = \mathrm{s}(\Psi_{\mathrm{A}i}^{\mathrm{imp}})\,[P_{\mathrm{K}i}\,\boldsymbol{\nu}_{\mathrm{K}i} + P_{\mathrm{L}i}\,\boldsymbol{\nu}_{\mathrm{L}i} - P_{\mathrm{N}i}\,\boldsymbol{\nu}_{\mathrm{N}i} + \mathbf{K}^{\mathsf{H}}(P_{\mathrm{K}i}\,\boldsymbol{\iota}_{\mathrm{K}i} + P_{\mathrm{L}i}\,\boldsymbol{\iota}_{\mathrm{L}i} + P_{\mathrm{N}i}\,\boldsymbol{\iota}_{\mathrm{N}i})]\,, \tag{5.87}$$

where $\mathrm{s}(x) = 0.5\,(1 + \mathrm{sgn}(x))$ is the step function and

$$\boldsymbol{\nu}_{\mathrm{T}i} = \boldsymbol{\Gamma}_{\mathrm{T}}^{i}\mathsf{V}, \qquad \boldsymbol{\iota}_{\mathrm{T}i} = \boldsymbol{\Gamma}_{\mathrm{T}}^{i}\mathsf{I}, \qquad \mathrm{T} = \mathrm{N},\mathrm{K},\mathrm{L}. \tag{5.88}$$

Once the optimum current density has been synthesized by the automated design method, the tensor impedance components can be retrieved using either (5.57)-(5.59) (from now on indicated as "diagonal formulation") or the (5.61)-(5.63) ("dense formulation"). Expressing these formulas in terms of cell-wise quantities, one has:

- diagonal formulation:
$$\begin{aligned} X_{\mathrm{I}}^{i} &= -\frac{P_{\mathrm{N}i}}{\mathcal{J}_{\mathrm{N}i}} \\ X_{\mathrm{K}}^{i} &= -\frac{P_{\mathrm{L}i}}{\mathcal{J}_{\mathrm{N}i}}, \\ X_{\mathrm{L}}^{i} &= \frac{P_{\mathrm{K}i}}{\mathcal{J}_{\mathrm{N}i}} \end{aligned} \tag{5.89}$$

- dense formulation:
$$\begin{aligned} X_{\mathrm{I}}^{i} &= \frac{\mathcal{J}_i Q_i - \mathcal{J}_{\mathrm{K}i} Q_{\mathrm{K}i} - \mathcal{J}_{\mathrm{L}i} Q_{\mathrm{L}i}}{\mathcal{J}_i^2 - \mathcal{J}_{\mathrm{K}i}^2 - \mathcal{J}_{\mathrm{L}i}^2} \\ X_{\mathrm{K}}^{i} &= \frac{-\mathcal{J}_{\mathrm{K}i} Q_i + \mathcal{J}_i Q_{\mathrm{K}i} + \mathcal{J}_{\mathrm{L}i}/\mathcal{J}_i(\mathcal{J}_{\mathrm{K}i} Q_{\mathrm{L}i} - \mathcal{J}_{\mathrm{L}i} Q_{\mathrm{K}i})}{\mathcal{J}_i^2 - \mathcal{J}_{\mathrm{K}i}^2 - \mathcal{J}_{\mathrm{L}i}^2}. \\ X_{\mathrm{L}}^{i} &= \frac{-\mathcal{J}_{\mathrm{L}i} Q_i + \mathcal{J}_i Q_{\mathrm{L}i} + \mathcal{J}_{\mathrm{K}i}/\mathcal{J}_i(\mathcal{J}_{\mathrm{L}i} Q_{\mathrm{K}i} - \mathcal{J}_{\mathrm{K}i} Q_{\mathrm{L}i})}{\mathcal{J}_i^2 - \mathcal{J}_{\mathrm{K}i}^2 - \mathcal{J}_{\mathrm{L}i}^2} \end{aligned} \tag{5.90}$$

## 5.5 Numerical Results

The developed tensor design method has been applied to a preliminary test case.

The considered antenna geometry is the circular one shown in Fig. 3.1a; for this first test, in order to limit the number of degrees of freedoms and the time per iteration required, the feeding structure (central pin and annular ring) is not modelled inside the optimization instance, but it is accounted for by employing as incident electric field the one generated by the launching structure in absence of the metasurface and by including its contribution to the far-field radiation. It is noted that this is expected to result in poor control of radiation efficiency.

An RO3003 dielectric substrate with $\varepsilon_r = 3$ and thickness 1.27 mm is chosen. The antenna has a radius of $6\,\lambda_0$ at the working frequency of 23 GHz, for a diameter of 156 mm. For this design, the lower and upper bounds for $X_{\mathrm{I}}$ are set equal to $-20\,000\,\Omega$ and $-200\,\Omega$, respectively; these values derive from the analysis of the data set of a double-anchor unit cell of size of about $1/6\,\lambda_0$ (not reported here). The goal is to achieve a broadside-radiating pencil beam; one must recall that no analytical modulation is assumed for the tensor impedance profile.

In case of circular geometry, such as this one, it seems natural to choose the cylindrical coordinate vectors $(\hat{\boldsymbol{\rho}}, \hat{\boldsymbol{\varphi}})$ as local orthonormal basis $(\hat{\boldsymbol{u}}, \hat{\boldsymbol{v}})$ for the definition of the four impedance dyadics:

$$\overline{\overline{\boldsymbol{I}}} = \hat{\boldsymbol{\rho}}\hat{\boldsymbol{\rho}} + \hat{\boldsymbol{\varphi}}\hat{\boldsymbol{\varphi}} = \hat{\boldsymbol{x}}\hat{\boldsymbol{x}} + \hat{\boldsymbol{y}}\hat{\boldsymbol{y}}, \tag{5.91}$$

$$\overline{\overline{\boldsymbol{N}}} = \hat{\boldsymbol{\varphi}}\hat{\boldsymbol{\rho}} - \hat{\boldsymbol{\rho}}\hat{\boldsymbol{\varphi}} = \hat{\boldsymbol{y}}\hat{\boldsymbol{x}} - \hat{\boldsymbol{x}}\hat{\boldsymbol{y}}, \tag{5.92}$$

$$\overline{\overline{\boldsymbol{K}}} = \hat{\boldsymbol{\rho}}\hat{\boldsymbol{\rho}} - \hat{\boldsymbol{\varphi}}\hat{\boldsymbol{\varphi}} = \cos(2\phi_i)\hat{\boldsymbol{x}}\hat{\boldsymbol{x}} + \sin(2\phi_i)\hat{\boldsymbol{x}}\hat{\boldsymbol{y}} + \sin(2\phi_i)\hat{\boldsymbol{y}}\hat{\boldsymbol{x}} - \cos(2\phi_i)\hat{\boldsymbol{y}}\hat{\boldsymbol{y}}, \tag{5.93}$$

$$\overline{\overline{\boldsymbol{L}}} = \hat{\boldsymbol{\varphi}}\hat{\boldsymbol{\rho}} + \hat{\boldsymbol{\rho}}\hat{\boldsymbol{\varphi}} = -\sin(2\phi_i)\hat{\boldsymbol{x}}\hat{\boldsymbol{x}} + \cos(2\phi_i)\hat{\boldsymbol{x}}\hat{\boldsymbol{y}} + \cos(2\phi_i)\hat{\boldsymbol{y}}\hat{\boldsymbol{x}} + \sin(2\phi_i)\hat{\boldsymbol{y}}\hat{\boldsymbol{y}}, \tag{5.94}$$

where $\phi_i$ is the angular coordinate of the centroid of each cell. It is clear that the final current density and radiation pattern would not change if rectangular coordinates were to be used. With this choice of coordinates, one has, on every $i$-th cell

$$X^i_{\rho\rho} = X^i_{\mathrm{I}} + X^i_{\mathrm{K}}, \tag{5.95}$$

$$X^i_{\rho\varphi} = X^i_{\varphi\rho} = X^i_{\mathrm{L}}, \tag{5.96}$$

$$X^i_{\varphi\varphi} = X^i_{\mathrm{I}} - X^i_{\mathrm{K}}. \tag{5.97}$$

The synthesized current density returned by the automated design method and the tensor impedance components are shown in Figs. 5.1 and 5.2, respectively.

The tensor impedance components shown in Fig. 5.2 are obtained from the optimum current density using the "dense formulation" (5.90) and applying a moving average scheme over clusters of neighboring cells. The same results (not shown here) are obtained if the "diagonal formulation" (5.89) is applied.

The obtained radiation pattern is plotted in Fig. 5.3, together with the mask-type constraints set ahead of the optimization process. The current density and the radiation pattern plotted in Figs. 5.1 and 5.3 are then computed by solving

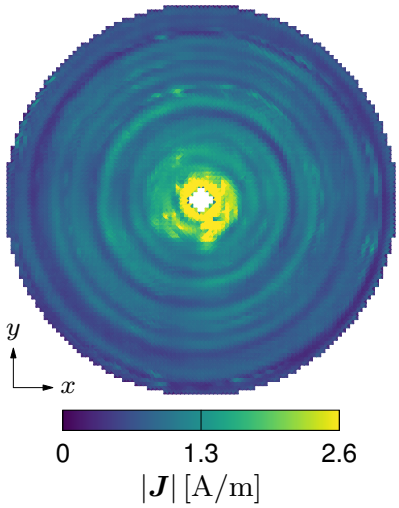


Figure 5.1: *Circular tensor metasurface with pencil beam*: optimum current density synthesized by the automated design method.

the forward problem for this impedance profile, to account for a possible efficiency reduction due to the impedance reconstruction process, similarly to what was done in Chapter 3. These are called "reconstructed" current and patterns in the following. From Fig. 5.3 it can be seen that the tensor impedance pattern synthesized by the automated design method satisfies the mask-type constraints (in particular, a $-20$ dB SLL). The aperture efficiency is 25%, higher than the one obtained with solutions based on an isotropic impedance (see Sec. 3.4.2). Radiation efficiency was not optimized as the feeding structure was not properly accounted for inside the optimization instance (see Chapter 3), which results in a low such value (12%).

It is interesting to notice that, despite the fact that no analytical modulation was imposed on the synthesizable tensor impedance profile ahead of the optimization process, the tensor components in Fig. 5.2 do resemble a spiral-like pattern [5, 42, 53].

The results appear noisy; this may be due to two main reasons:

- *intrinsic uncertainty of the employed tensor impedance retrieval technique*: both formulations (5.89)-(5.90) are based on a testing strategy of the EFIE that depends on $\boldsymbol{J}^*$; this means that in the areas where $\boldsymbol{J}$ is linearly polarized ($\mathrm{Im}(J_u J_v^*) = 0$), but not zero, the retrieval formulas either assume an indeterminate form of the kind $0/0$ or are unbounded, which cannot be equate to an open circuit situation as in the scalar case due to $|\boldsymbol{J}| \neq 0$. Therefore, in these regions the retrieved impedance components exhibit noise, very high values o rapid change in sign. This kind of uncertainty is partially mitigated by the application of a moving average scheme; a better compensation of this problem could be achieved by performing additional smoothing on the results

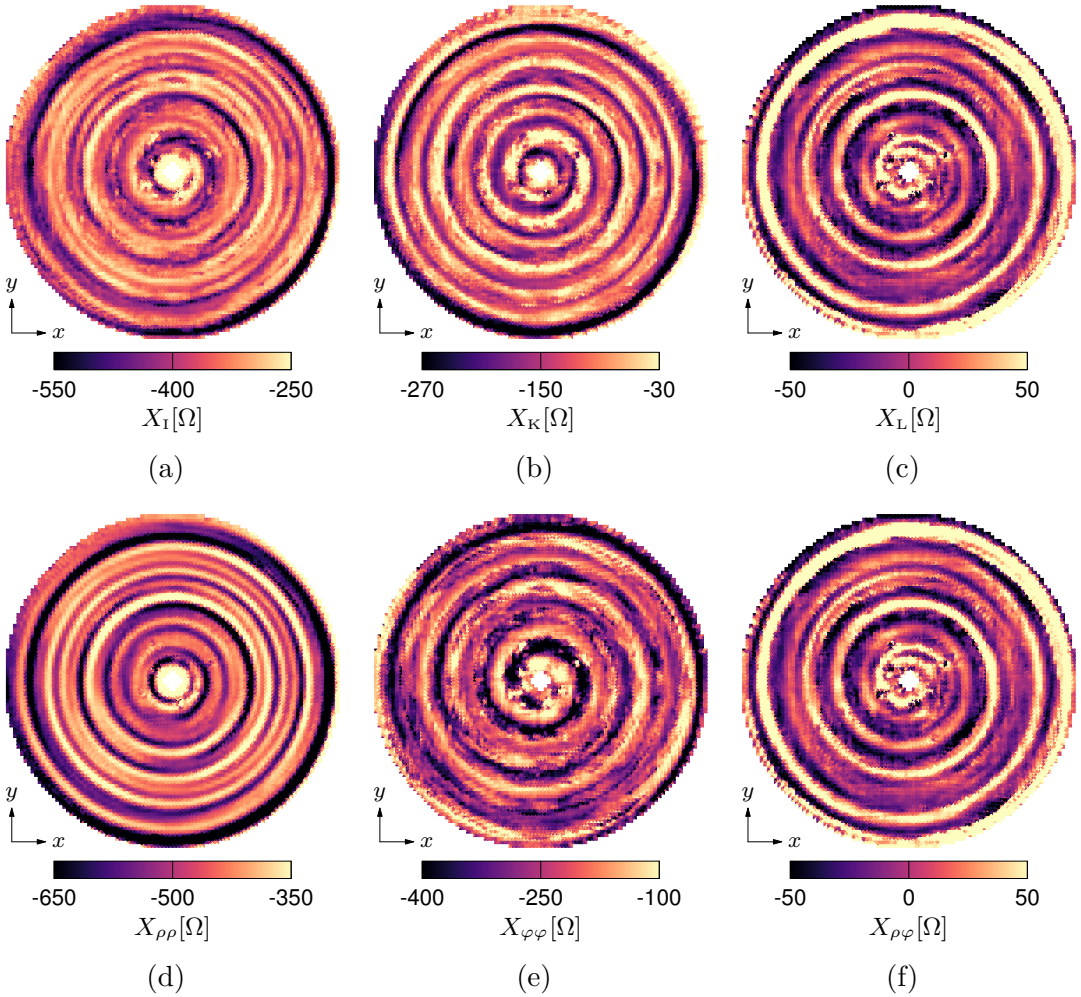


Figure 5.2: *Circular tensor metasurface with pencil beam*, tensor impedance components obtained using (5.90): (a) $X_{\mathrm{I}}$, (b) $X_{\mathrm{K}}$, (c) $X_{\mathrm{L}}$, (d) $X_{\rho\rho}$, (e) $X_{\varphi\varphi}$, (f) $X_{\rho\varphi}$.

(averaging over larger areas) or by enforcing some degree of regularity on the current density inside the optimization process.

- *incomplete convergence/sub-optimal solution because of unbalanced weights*: in its current state, the automated design algorithm, both in the scalar and tensor version, is very sensitive to the user's choice of the weighting parameters associated to the different functionals, which may either accelerate or hinder the convergence of the optimization process. To address this problem, work is in progress on a novel adapting weighting scheme to automatically select optimal weights [88].

In order to understand performances (and some intrinsic properties of the field manipulation), it is instructive to analyze the tensor impedance in its eigen-basis

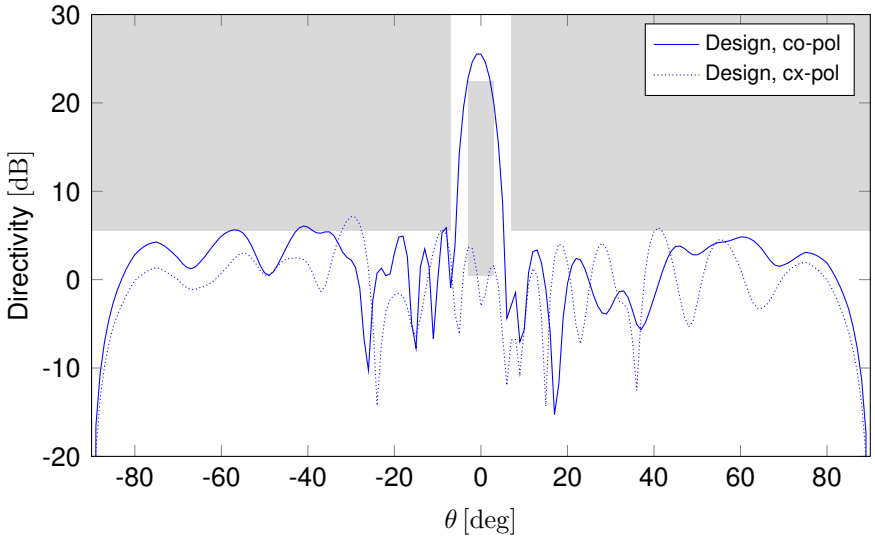


Figure 5.3: *Circular tensor metasurface with pencil beam*: far-field cut at $\varphi = 0°$ generated by the reconstructed current density.

(diagonal), using the relationship in Sec. 5.2. To this aim, Fig. 5.4 shows the spatial distribution of the eigenvalues $X_1$ and $X_2$. Both quantities are capacitive everywhere on the metasurface, as desired. It is observed than one eigenvalue only is noisy (denoted with 2). In order to analyze the impact of the eigenvalues on the overall functioning of the metasurface it is instructive to analyze the (local) energy associated to the eigenvalues, i.e.

$$W_i = \langle \boldsymbol{U}_i \, , \boldsymbol{J}^* \rangle X_i \langle \boldsymbol{U}_i \, , \boldsymbol{J} \rangle, \quad i = 1,2 \tag{5.98}$$

where $\boldsymbol{U}_i$ is the eigenvector associated to eigenvalue $X_i$; this is reported in Fig. 5.5 (in terms of Poynting theorem this stored energy density is proportional to the reactive power density). From this figure it is apparent that the noisy eigenvalue $X_2$ contributes significantly less to energy storage. On one hand, this explains why recovering it from energy-type testings of current and field is more prone to noise. On the other hand, it also implies some degree of robustness of the process, as the noise appears in the least relevant component of the impedance tensor *for the specific case of the undertaken design.*

## 5.6 Conclusions and Future Work

In this Chapter, an automated design method for the design of tensor metasurfaces has been presented. Preliminary numerical results related to a circular metasurface radiating a broadside pencil beam are promising; the next step will involve implementation of the synthesized tensor impedance using anisotropic unit

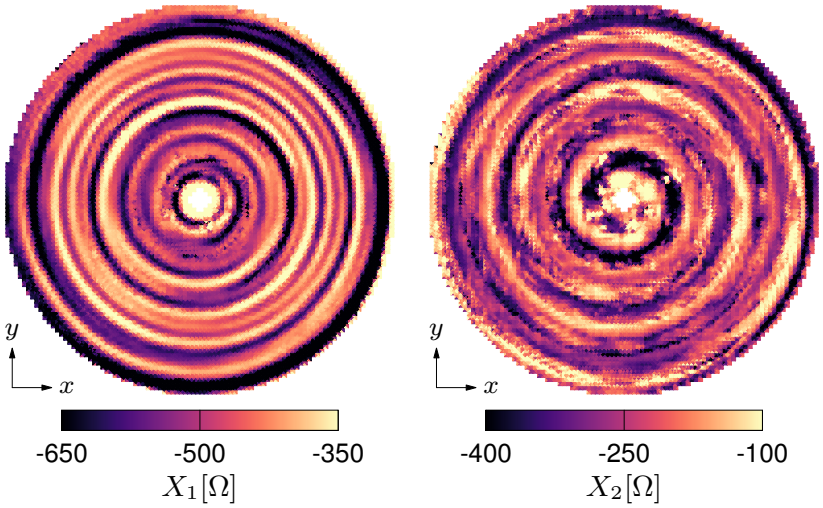


(a) (b)

Figure 5.4: *Circular tensor metasurface with pencil beam*, tensor impedance eigenvalues: (a) $X_1$, (b) $X_2$.

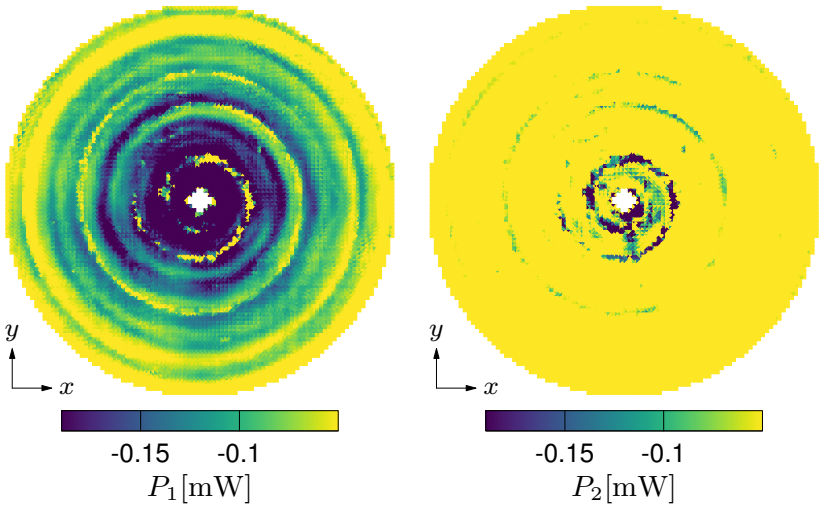


(a) (b)

Figure 5.5: *Circular tensor metasurface with pencil beam*, reactive power density associated to the tensor impedance eigenvalues: (a) $P_1$, (b) $P_2$.

cells and validation of the design method via full-wave simulation of the complete antenna.

# Chapter 6

# Conclusions

In this dissertation, the deterministic design of metasurface antennas has been addressed, by exploring and enhancing existing design methods and developing more advanced ones. The metasurface is consistently modelled as an impedance boundary condition (IBC); both analytical and numerical design approaches were considered in the development of reconfigurable or static, scalar or tensor metasurfaces.

First, an analytical design approach, based on the leaky-wave radiation paradigm in sinusoidally-modulated reactance surfaces and the transverse equivalent network analysis of multilayered structures, was used to design a low-profile, beam-scanning dual-metasurface antenna, where beam steering is achieved thanks to a reconfigurable metasurface loaded with varactor diodes, biased by a single voltage signal without the need for vertical vias. A prototype of the designed antenna was fabricated and tested, and its performances were in excellent agreement with design and simulation results, demonstrating the accuracy of the employed analytical tools. At the same time, the noisy radiation pattern highlighted the limitation of employing a sinusoidal modulation of the surface impedance to generate radiation, thus shifting the focus towards deterministic numerical methods for the synthesis of metasurfaces.

In this perspective, a recently-developed current-based automated method for metasurface design was generalized by introducing realistic 3-D feeding structures and PEC regions inside the optimization instance, thus allowing the fully numerical, self-consistent design of metasurface antennas by taking into account the interactions between the real launching structure and the proper IBC region. This required the introduction of a new functional inside the cost function that could effectively impose the PEC condition on the corresponding region. This generalized automated design method was successfully applied to the synthesis of center-fed circular antennas and edge-fed rectangular antennas, with radiation patterns ranging from broadside beams to squinted, multi-beam and cosecant squared patterns.

To further validate the proposed method, the design and fabrication of edge-fed,

broadside-radiating leaky-wave antennas (LWAs), which notoriously suffer from the open stopband (OSB) problem, was undertaken. The proper modeling of the feeding structure and the intrinsic maximization of the realized gain in the proposed algorithm were instrumental in overcoming the OSB, as demonstrated by experimental results.

Finally, the automated synthesis method was extended to deal with tensor metasurfaces; this required to devise a new retrieval strategy for the tensor impedance components from the optimum current and to define new IBC realizability functionals. Preliminary results involving a broadside-radiating, circular tensor metasurface showed that the method is capable of numerically synthesizing tensor impedances without the need of a-priori parameterizations on the impedance profile.

Based on the work presented in this Thesis, several improvements can be outlined and pursued. First of all, given the great interest and potentiality in tensor metasurfaces, the generalized tensor numerical method should be applied to the synthesis of more complicated designs that involve realistic feeding structures; these designs must then be physically implemented with anisotropic unit cells (e.g., double anchors) and simulated to validate the method. Multi-feed excitation should also be explored, since the same tensor metasurface can generate different radiation patterns when illuminated by different incident fields.

Another very relevant improvement would be the fully automated selection of the optimum weights in the optimization cost function for the rapid convergence of the synthesis algorithm, both in the scalar and tensor cases. In the perspective of improving the performance of the proposed method, optimization algorithms other than the non-linear conjugate gradient should be tested.

Finally, the deterministic numerical method could also be applied to the design of multilayered, beam-scanning antennas, to investigate the possibility of obtaining a wider steering range and overall better performances than the ones obtained with analytical methods.

# Appendix A

# Cost Functionals

## A.1 Radiated Field Functional

The cost function encompassing the radiation requirements is defined as

$$f_{\mathrm{rad}} = w^{\mathrm{co}}\rho^{\mathrm{co}} + w^{\mathrm{cx}}\rho^{\mathrm{cx}} + w^{\mathrm{tot}}\rho^{\mathrm{tot}}, \tag{A.1}$$

where each individual functional of the weighted sum is given by the sum of terms over all considered far field directions:

$$\rho^{\mathrm{x}} = \sum\nolimits_{j=1}^{N_{\mathrm{ff}}} \rho_j^{\mathrm{x}} \tag{A.2}$$

where "x" should be replaced by the corresponding component ("co", "cx" or "tot"), and the index $j = 1, \ldots, N_{\mathrm{ff}}$ refers to the far field direction $(\theta_j, \phi_j)$. Below are the definitions of each term:

$$\rho_j^{\mathrm{co}} = \mathrm{r}^2(M_{\mathrm{L},j}^{\mathrm{co}} - F_j^{\mathrm{co}}) + \mathrm{r}^2(F_j^{\mathrm{co}} - M_{\mathrm{U},j}^{\mathrm{co}}), \tag{A.3}$$

$$\rho_j^{\mathrm{cx}} = \mathrm{r}^2(F_j^{\mathrm{cx}} - M_j^{\mathrm{cx}}), \tag{A.4}$$

$$\rho_j^{\mathrm{tot}} = \mathrm{r}^2(F_j^{\mathrm{tot}} - M_j^{\mathrm{tot}}), \tag{A.5}$$

where $\mathrm{r}(x) = \max(x,0)$, and

$$F_j^{\mathrm{co}} = \left|E_j^{\mathrm{co}}\right|^2, \tag{A.6}$$

$$F_j^{\mathrm{cx}} = \left|E_j^{\mathrm{cx}}\right|^2, \tag{A.7}$$

$$F_j^{\mathrm{tot}} = \left|E_j^{\mathrm{co}}\right|^2 + \left|E_j^{\mathrm{cx}}\right|^2. \tag{A.8}$$

The co- and cross-polarization components of the electric field are obtained by applying the discretized radiation operator to the current coefficients:

$$\mathsf{E}^{\mathrm{co}} = \mathbf{R}^{\mathrm{co}}\,\mathsf{I}, \tag{A.9}$$

$$\mathsf{E}^{\mathrm{cx}} = \mathbf{R}^{\mathrm{cx}}\,\mathsf{I}. \tag{A.10}$$

## A.2 Scalar Impedance Realizability Functional

The total realizability cost function for the IBC includes the conditions of passivity and losslessness ("act"), scalarity ("scal"), and upper/lower impedance bounds ("imp"):

$$f_{\text{ibc}} = w^{\text{act}}\rho^{\text{act}} + w^{\text{scal}}\rho^{\text{scal}} + w^{\text{imp}}\rho^{\text{imp}}. \tag{A.11}$$

It is formulated as a weighted sum of functionals. Each of these functionals in turn is expressed as a sum of functionals defined over individual cells,

$$\rho^{\text{x}} = \sum\nolimits_{i\in\mathcal{I}_{\text{ibc}}} \rho_i^{\text{x}} \tag{A.12}$$

where "x" should be replaced by the corresponding condition ("act", "scal" or "imp"), and $\mathcal{I}_{\text{ibc}} = \{i \in \mathbb{N} \,|\, \mathcal{S}_i \subset \mathcal{S}_{\text{IBC}}\}$. Individual terms are defined as follows:

$$\rho_i^{\text{act}} = P_i^2, \tag{A.13}$$

$$\rho_i^{\text{scal}} = \mathcal{E}_i\,\mathcal{J}_i - \left(P_i^2 + Q_i^2\right), \tag{A.14}$$

$$\rho_i^{\text{imp}} = \text{r}^2(X_{\min}\mathcal{J}_i - Q_i) + \text{r}^2(Q_i - X_{\max}\mathcal{J}_i), \tag{A.15}$$

where

$$P_i = \frac{1}{A_i}\,\text{Re}\iint_{\mathcal{S}_i} \boldsymbol{E}\cdot\boldsymbol{J}^*\,\text{d}S = \text{Re}\left(\mathsf{I}^{\text{H}}\boldsymbol{\Gamma}_i\mathsf{V}\right), \tag{A.16}$$

$$Q_i = \frac{1}{A_i}\,\text{Im}\iint_{\mathcal{S}_i} \boldsymbol{E}\cdot\boldsymbol{J}^*\,\text{d}S = \text{Im}\left(\mathsf{I}^{\text{H}}\boldsymbol{\Gamma}_i\mathsf{V}\right), \tag{A.17}$$

$$\mathcal{J}_i = \frac{1}{A_i}\iint_{\mathcal{S}_i} |\boldsymbol{J}|^2\,\text{d}S = \mathsf{I}^{\text{H}}\boldsymbol{\Gamma}_i\mathsf{I}, \tag{A.18}$$

$$\mathcal{E}_i = \frac{1}{A_i}\iint_{\mathcal{S}_i} |\boldsymbol{E}|^2\,\text{d}S = \mathsf{V}^{\text{H}}\boldsymbol{\Gamma}_i\mathsf{V}, \tag{A.19}$$

with $A_i$ being the surface area of the $i$-th cell. In the above,

$$\mathsf{V} = \mathbf{G}^{-1}(\mathsf{V}_{\text{inc}} + \mathbf{L}\mathsf{I}), \tag{A.20}$$

where $\mathbf{G} \in \mathbb{R}^{N\times N}$ is the Gram matrix of the RWG basis functions, defined as

$$(\mathbf{G})_{mn} = \iint \boldsymbol{\Lambda}_m(\boldsymbol{r})\cdot\boldsymbol{\Lambda}_n(\boldsymbol{r})\,\text{d}\boldsymbol{r} \tag{A.21}$$

and $\boldsymbol{\Gamma}_i \in \mathbb{R}^{N\times N}$ is the (averaging) local Gram matrix for the $i$-th cell, defined as

$$(\boldsymbol{\Gamma}_i)_{mn} = \frac{1}{A_i}\iint_{\mathcal{S}_i} \boldsymbol{\Lambda}_m(\boldsymbol{r})\cdot\boldsymbol{\Lambda}_n(\boldsymbol{r})\,\text{d}\boldsymbol{r}. \tag{A.22}$$

# Appendix B

# Scalar Impedance Retrieval

Starting from the discretized integral equation (3.6) restricted to the IBC region, the impedance is first expanded into a linear combination of basis functions,

$$Z(\boldsymbol{r}) = \sum_{i=1}^{M} z_i \, \psi_i(\boldsymbol{r}). \tag{B.1}$$

From the knowledge of the (optimal) equivalent current, the coefficients of the impedance expansion are found by minimizing the error in the integral equation, i.e.,

$$\mathsf{z} = \underset{\mathsf{z}\in\mathbb{C}^M}{\arg\min} \, \|\mathsf{V}_{\text{tot}} - \boldsymbol{\Psi}\mathsf{z}\| \tag{B.2}$$

where $\mathsf{z}$ collects the impedance coefficients, $\mathsf{V}_{\text{tot}} = \mathsf{V}_{\text{inc}} + \boldsymbol{\mathsf{L}}\mathsf{I}$ is the total electric field in terms of the equivalent current, and the elements of the matrix $\boldsymbol{\Psi}$,

$$(\boldsymbol{\Psi})_{mi} = \langle \, \boldsymbol{\Lambda}_m \, , \psi_i \, \boldsymbol{J}^{\Lambda} \, \rangle \tag{B.3}$$

with $\boldsymbol{J}^{\Lambda} = \sum_{n=1}^{N} I_n \boldsymbol{\Lambda}_n$, represent the linear dependence of the total field on the coefficients of the impedance. Finding the impedance through (B.2) constitutes a convex optimization problem.

If we express the impedance in terms of piece-wise constant basis functions on each triangle, i.e.,

$$\psi_i(\boldsymbol{r}) = \begin{cases} 1, & \text{for } \boldsymbol{r} \in \mathcal{S}_i \\ 0, & \text{elsewhere} \end{cases} \qquad i = 1, \ldots, N_{\text{c}} \tag{B.4}$$

the optimum impedance coefficients can be obtained in closed form as

$$z_i = \frac{\iint_{\mathcal{S}_i} \boldsymbol{E}_{\tan} \cdot \boldsymbol{J}^* \, \mathrm{d}S}{\iint_{\mathcal{S}_i} |\boldsymbol{J}|^2 \, \mathrm{d}S} = \frac{\mathsf{I}^{\mathsf{H}} \boldsymbol{\mathsf{\Gamma}}_i \mathsf{V}}{\mathsf{I}^{\mathsf{H}} \boldsymbol{\mathsf{\Gamma}}_i \mathsf{I}}. \tag{B.5}$$

A limiting case, often encountered in practice, is when the denominator of (B.5) is close to zero, while its numerator is much larger than zero, which corresponds to an infinite impedance value. This implies the absence of the IBC over the considered triangle, a condition that can be easily implemented in the numerical solution by removing the corresponding degrees of freedom from the discretization.

# Bibliography


[1] S. Maci, G. Minatti, M. Casaletti, and M. Bosiljevac, "Metasurfing: Addressing Waves on Impenetrable Metasurfaces", *IEEE Antennas Wirel. Propag. Lett.*, vol. 10, pp. 1499–1502, 2011.

[2] A. M. Patel and A. Grbic, "Modeling and Analysis of Printed-Circuit Tensor Impedance Surfaces", *IEEE Trans. Antennas Propag.*, vol. 61, no. 1, pp. 211–220, Jan. 2013.

[3] A. Oliner and A. Hessel, "Guided waves on sinusoidally-modulated reactance surfaces", *IRE Trans. Antennas Propag.*, vol. 7, no. 5, pp. 201–208, Dec. 1959.

[4] A. M. Patel and A. Grbic, "A Printed Leaky-Wave Antenna Based on a Sinusoidally-Modulated Reactance Surface", *IEEE Trans. Antennas Propag.*, vol. 59, no. 6, pp. 2087–2096, Jun. 2011.

[5] G. Minatti, F. Caminita, M. Casaletti, and S. Maci, "Spiral Leaky-Wave Antennas Based on Modulated Surface Impedance", *IEEE Trans. Antennas Propag.*, vol. 59, no. 12, pp. 4436–4444, Dec. 2011.

[6] M. Zucchi, F. Vernì, M. Righero, and G. Vecchi, "Current Based Automated Design of Realizable Metasurface Antennas With Arbitrary Pattern Constraints", *IEEE Trans. Antennas Propag.*, vol. 71, no. 6, pp. 4888–4902, Jun. 2023.

[7] T. Brown, Y. Vahabzadeh, C. Caloz, and P. Mojabi, "Electromagnetic Inversion With Local Power Conservation for Metasurface Design", *IEEE Antennas Wirel. Propag. Lett.*, vol. 19, no. 8, pp. 1291–1295, Aug. 2020.

[8] M. Salucci, A. Gelmini, G. Oliveri, N. Anselmi, and A. Massa, "Synthesis of Shaped Beam Reflectarrays With Constrained Geometry by Exploiting Non-radiating Surface Currents", *IEEE Trans. Antennas Propag.*, vol. 66, no. 11, pp. 5805–5817, Nov. 2018.

[9] C. Walter, *Traveling Wave Antennas*. New York:McGraw-Hill, 1965.

[10] D. R. Jackson, C. Caloz, and T. Itoh, "Leaky-Wave Antennas", *Proc. IEEE*, vol. 100, no. 7, pp. 2194–2206, Jul. 2012.

[11] L. Teodorani, F. Vernì, G. Giordanengo, R. Gaffoglio, and G. Vecchi, "Experimental Demonstration of Beam Scanning of Dual-Metasurface Antenna", *Electronics*, vol. 12, no. 8, p. 1833, Jan. 2023.

[12] C. G. Christodoulou, Y. Tawk, S. A. Lane, and S. R. Erwin, "Reconfigurable Antennas for Wireless and Space Applications", *Proc. IEEE*, vol. 100, no. 7, pp. 2250–2261, Jul. 2012.

[13] J. Schoebel *et al.*, "Design considerations and technology assessment of phased-array antenna systems with RF MEMS for automotive radar applications", *IEEE Trans. Microw. Theory Tech.*, vol. 53, no. 6, pp. 1968–1975, Jun. 2005.

[14] K.-C. Huang and Z. Wang, "Millimeter-wave circular polarized beam-steering antenna array for gigabit wireless communications", *IEEE Trans. Antennas Propag.*, vol. 54, no. 2, pp. 743–746, Feb. 2006.

[15] A. Ohadi and G. V. Eleftheriades, "Fixed-Frequency Beam-Steering Using Slotted Waveguide With Tunable Impedance Walls", *IEEE Open J. Antennas Propag.*, vol. 2, pp. 978–990, 2021.

[16] F. Monticone and A. Alu, "Leaky-Wave Theory, Techniques, and Applications: From Microwaves to Visible Frequencies", *Proc. IEEE*, vol. 103, no. 5, pp. 793–821, May 2015.

[17] M. Esquius-Morote, J. S. Gómez-Dı´az, and J. Perruisseau-Carrier, "Sinusoidally Modulated Graphene Leaky-Wave Antenna for Electronic Beamscanning at THz", *IEEE Trans. Terahertz Sci. Technol.*, vol. 4, no. 1, pp. 116–122, Jan. 2014.

[18] E. Torabi, A. Rozhkova, P.-Y. Chen, and D. Erricolo, "Compact and Reconfigurable Leaky Wave Antenna Based on a Tunable Substrate Integrated Embedded Metasurface", in *2020 IEEE Int. Symp. Antennas Propag. North Am. Radio Sci. Meet.*, Jul. 2020, pp. 163–164.

[19] E. Martini *et al.*, "Reconfigurable Antenna Based on Liquid Crystals for Continuous Beam Scanning with a Single Control", in *2019 IEEE Int. Symp. Antennas Propag. USNC-URSI Radio Sci. Meet.*, Jul. 2019, pp. 449–450.

[20] S. C. Pavone, E. Martini, F. Caminita, M. Albani, and S. Maci, "Surface Wave Dispersion for a Tunable Grounded Liquid Crystal Substrate Without and With Metasurface on Top", *IEEE Trans. Antennas Propag.*, vol. 65, no. 7, pp. 3540–3548, Jul. 2017.

[21] M. S. Rabbani, J. Churm, and A. P. Feresidis, "Continuous Beam-Steering Low-Loss Millimeter-Wave Antenna Based on a Piezo-Electrically Actuated Metasurface", *IEEE Trans. Antennas Propag.*, vol. 70, no. 4, pp. 2439–2449, Apr. 2022.

[22] D. Sievenpiper, "Forward and backward leaky wave radiation with large effective aperture from an electronically tunable textured surface", *IEEE Trans. Antennas Propag.*, vol. 53, no. 1, pp. 236–247, Jan. 2005.

[23] R. Guzman-Quiros, J. L. Gomez-Tornero, A. R. Weily, and Y. J. Guo, "Electronically Steerable 1-D Fabry-Perot Leaky-Wave Antenna Employing a Tunable High Impedance Surface", *IEEE Trans. Antennas Propag.*, vol. 60, no. 11, pp. 5046–5055, Nov. 2012.

[24] D. J. Gregoire, A. Patel, and R. Quarfoth, "A design for an electronically-steerable holographic antenna with polarization control", in *2015 IEEE Int. Symp. Antennas Propag. Usn. Natl. Radio Sci. Meet.*, Jul. 2015, pp. 2203–2204.

[25] R. G. Quarfoth, A. M. Patel, and D. J. Gregoire, "Ka-band electronically scanned artificial impedance surface antenna", in *2016 IEEE Int. Symp. Antennas Propag. APSURSI*, Jun. 2016, pp. 651–652.

[26] N. Shlezinger, G. C. Alexandropoulos, M. F. Imani, Y. C. Eldar, and D. R. Smith, "Dynamic Metasurface Antennas for 6G Extreme Massive MIMO Communications", *IEEE Wirel. Commun.*, vol. 28, no. 2, pp. 106–113, Apr. 2021.

[27] M. Wang, H. F. Ma, W. xuan Tang, H. C. Zhang, W. xiang Jiang, and T. J. Cui, "A Dual-Band Electronic-Scanning Leaky-Wave Antenna Based on a Corrugated Microstrip Line", *IEEE Trans. Antennas Propag.*, vol. 67, no. 5, pp. 3433–3438, May 2019.

[28] Z. Lin *et al.*, "Refracting RIS-Aided Hybrid Satellite-Terrestrial Relay Networks: Joint Beamforming Design and Optimization", *IEEE Trans. Aerosp. Electron. Syst.*, vol. 58, no. 4, pp. 3717–3724, Aug. 2022.

[29] H. Niu *et al.*, "Active RIS Assisted Rate-Splitting Multiple Access Network: Spectral and Energy Efficiency Tradeoff", *IEEE J. Sel. Areas Commun.*, vol. 41, no. 5, pp. 1452–1467, May 2023.

[30] H. Niu *et al.*, "Joint Beamforming Design for Secure RIS-Assisted IoT Networks", *IEEE Internet Things J.*, vol. 10, no. 2, pp. 1628–1641, Jan. 2023.

[31] Z. Lin, M. Lin, B. Champagne, W.-P. Zhu, and N. Al-Dhahir, "Secrecy-Energy Efficient Hybrid Beamforming for Satellite-Terrestrial Integrated Networks", *IEEE Trans. Commun.*, vol. 69, no. 9, pp. 6345–6360, Sep. 2021.

[32] A. J. Martinez-Ros, J. L. Gomez-Tornero, and G. Goussetis, "Broadside radiation from radial arrays of substrate integrated leaky-wave antennas", in *2012 6th Eur. Conf. Antennas Propag. EUCAP*, Prague, Mar. 2012, pp. 252–254.

[33] D. M. Pozar, *Microwave Engineering, 4th Edition*. John Wiley & Sons, 2011.

[34] Z. Wu and A. Grbic, "Serrodyne Frequency Translation Using Time-Modulated Metasurfaces", *IEEE Trans. Antennas Propag.*, vol. 68, no. 3, pp. 1599–1606, Mar. 2020.

[35] MACOM Technology Solutions, https://www.macom.com/products/product-detail/MAVR-011020-1411.

[36] S. Maci, M. Caiazzo, A. Cucini, and M. Casaletti, "A pole-zero matching method for EBG surfaces composed of a dipole FSS printed on a grounded dielectric slab", *IEEE Trans. Antennas Propag.*, vol. 53, no. 1, pp. 70–81, Jan. 2005.

[37] R. Guzmán Quirós, "Analysis and design of new electronically reconfigurable periodic leaky-wave antennas", PhD dissertation, Universidad Politécnica de Cartagena, 2014.

[38] *CST Studio Suite®*, Dassault Systèmes.

[39] D. Yang and S. Nam, "Tapered Unit Cell Control of a Sinusoidally Modulated Reactance Surface Antenna", *IEEE Antennas Wirel. Propag. Lett.*, vol. 17, no. 12, pp. 2479–2483, Dec. 2018.

[40] L. Teodorani, M. Zucchi, and G. Vecchi, "Generalized Deterministic Automated Design of Metasurface Antennas with 3D Feeding Structures", *IEEE Trans. Antennas Propag.*, pp. 1–1, 2024.

[41] G. Minatti *et al.*, "Modulated Metasurface Antennas for Space: Synthesis, Analysis and Realizations", *IEEE Trans. Antennas Propag.*, vol. 63, no. 4, pp. 1288–1300, Apr. 2015.

[42] G. Minatti, F. Caminita, E. Martini, M. Sabbadini, and S. Maci, "Synthesis of Modulated-Metasurface Antennas With Amplitude, Phase, and Polarization Control", *IEEE Trans. Antennas Propag.*, vol. 64, no. 9, pp. 3907–3919, Sep. 2016.

[43] M. Bodehou, C. Craeye, and I. Huynen, "Electric Field Integral Equation-Based Synthesis of Elliptical-Domain Metasurface Antennas", *IEEE Trans. Antennas Propag.*, vol. 67, no. 2, pp. 1270–1274, Feb. 2019.

[44] A. Scarabosio, F. Vernì, M. Righero, G. Giordanengo, and G. Vecchi, "Toward Fast Machine Design of Metasurface Antennas", in *Proc. 16th Eur. Conf. Antennas Propag.*, Madrid, Mar. 2022.

[45] F. Vernì, "Advanced Computational Electromagnetics for Metasurfaces", Ph.D. dissertation, Politecnico di Torino, Aug. 2020.

[46] J. Cavillot, M. Bodehou, and C. Craeye, "Metasurface Antennas Design: Full-Wave Feeder Modeling and Far-Field Optimization", *IEEE Trans. Antennas Propag.*, vol. 71, no. 1, pp. 39–49, Jan. 2023.

[47] J. Budhu, L. Szymanski, and A. Grbic, "Design of Planar and Conformal, Passive, Lossless Metasurfaces That Beamform", *IEEE J. Microw.*, vol. 2, no. 3, pp. 401–418, Jul. 2022.

[48] A. Epstein and G. V. Eleftheriades, "Synthesis of passive lossless metasurfaces using auxiliary fields for reflectionless beam splitting and perfect reflection", *Phys. Rev. Lett.*, vol. 117, no. 25, p. 256 103, Dec. 2016. arXiv: 1607.02954 [physics].

[49] V. G. Ataloglou and G. V. Eleftheriades, "Arbitrary Wave Transformations With Huygens' Metasurfaces Through Surface-Wave Optimization", *IEEE Antennas Wirel. Propag. Lett.*, vol. 20, no. 9, pp. 1750–1754, Sep. 2021.

[50] T. Brown and P. Mojabi, "Cascaded Metasurface Design Using Electromagnetic Inversion With Gradient-Based Optimization", *IEEE Trans. Antennas Propag.*, vol. 70, no. 3, pp. 2033–2045, Mar. 2022.

[51] J. Budhu and A. Grbic, "Perfectly Reflecting Metasurface Reflectarrays: Mutual Coupling Modeling Between Unique Elements Through Homogenization", *IEEE Trans. Antennas Propag.*, vol. 69, no. 1, pp. 122–134, Jan. 2021.

[52] J. Budhu, E. Michielssen, and A. Grbic, "The Design of Dual Band Stacked Metasurfaces Using Integral Equations", *IEEE Trans. Antennas Propag.*, vol. 70, no. 6, pp. 4576–4588, Jun. 2022.

[53] M. Bodehou, C. Craeye, E. Martini, and I. Huynen, "A Quasi-Direct Method for the Surface Impedance Design of Modulated Metasurface Antennas", *IEEE Trans. Antennas Propag.*, vol. 67, no. 1, pp. 24–36, Jan. 2019.

[54] M. Bodehou, K. A. Khalifeh, S. N. Jha, and C. Craeye, "Direct Numerical Inversion Methods for the Design of Surface Wave-Based Metasurface Antennas: Fundamentals, Realizations, and Perspectives", *IEEE Antennas Propag. Mag.*, vol. 64, no. 4, pp. 24–36, Aug. 2022.

[55] S. Pearson and S. V. Hum, "Optimization of Electromagnetic Metasurface Parameters Satisfying Far-Field Criteria", *IEEE Trans. Antennas Propag.*, vol. 70, no. 5, pp. 3477–3488, May 2022.

[56] D.-H. Kwon, "Modulated Reactance Surfaces for Leaky-Wave Radiation Based on Complete Aperture Field Synthesis", *IEEE Trans. Antennas Propag.*, vol. 68, no. 7, pp. 5463–5477, Jul. 2020.

[57] H. Lee and D.-H. Kwon, "Printed Metasurface Leaky Wave Antennas Based on Penetrable Aperture Field Synthesis", *IEEE Trans. Antennas Propag.*, vol. 71, no. 6, pp. 4724–4736, Jun. 2023.

[58] H. Lee and D.-H. Kwon, "2-D Circularly Polarized Printed Metasurface Leaky-Wave Antennas on a Conformal Aperture", *IEEE Antennas Wirel. Propag. Lett.*, vol. 22, no. 11, pp. 2614–2618, Nov. 2023.

[59] F. Caminita, E. Martini, G. Minatti, M. Sabbadini, and S. Maci, "Low-Profile Dual-Polarized Isoflux Antennas for Space Applications", *IEEE Trans. Antennas Propag.*, vol. 69, no. 6, pp. 3204–3213, Jun. 2021.

[60] M. Bodehou and C. Craeye, "Array Surface-Wave Launcher for the Efficient Generation of Shaped Beam and Multibeam With Metasurface", *IEEE Trans. Antennas Propag.*, vol. 69, no. 12, pp. 8860–8865, Dec. 2021.

[61] L. Teodorani, M. Zucchi, and G. Vecchi, "Modeling of 3D Feeding Structures in the Automated Design of Metasurface Antennas", in *Proc. 18th Eur. Conf. Antennas Propag.*, Glasgow, Mar. 2024, pp. 1285–1287.

[62] E. Kuester, M. Mohamed, M. Piket-May, and C. Holloway, "Averaged transition conditions for electromagnetic fields at a metafilm", *IEEE Trans. Antennas Propag.*, vol. 51, no. 10, pp. 2641–2651, Oct. 2003.

[63] K. A. Michalski and J. R. Mosig, "Multilayered media Green's functions in integral equation formulations", *IEEE Trans. Antennas Propag.*, vol. 45, no. 3, pp. 508–519, Mar. 1997.

[64] S. Rao, D. Wilton, and A. Glisson, "Electromagnetic scattering by surfaces of arbitrary shape", *IEEE Trans. Antennas Propag.*, vol. 30, no. 3, pp. 409–418, May 1982.

[65] K. A. Michalski, "Electromagnetic Field Computation in Planar Multilayers", in *Encyclopedia of RF and Microwave Engineering*, John Wiley & Sons, Ltd, 2005.

[66] J. Nocedal and S. J. Wright, *Numerical Optimization* (Springer Series in Operations Research), 2nd ed. New York: Springer, 2006.

[67] M. Salucci, L. Poli, P. Rocca, and A. Massa, "Learned Global Optimization for Inverse Scattering Problems: Matching Global Search With Computational Efficiency", *IEEE Trans. Antennas Propag.*, vol. 70, no. 8, pp. 6240–6255, Aug. 2022.

[68] "IEEE Standard for Definitions of Terms for Antennas", *IEEE Std 145-2013 Revis. IEEE Std 145-1993*, pp. 1–50, Mar. 2014.

[69] M. Zucchi, "Numerical Techniques for the Automated Design of Metasurface Antennas", Ph.D. dissertation, Politecnico di Torino, Oct. 2022.

[70] D. H. Brandwood, "A complex gradient operator and its application in adaptive array theory", *IEE Proc. H Microw. Opt. Antennas*, vol. 130, no. 1, pp. 11–16, Feb. 1983.

[71] R. Maggiora, G. Vecchi, V. Lancellotti, and V. Kyrytsya, "Efficient 3D/1D self-consistent integral-equation analysis of ICRH antennae", *Nucl. Fusion*, vol. 44, no. 8, p. 846, Jul. 2004.

[72] W. C. Chew, Z. Nie, Q. H. Liu, and Y. T. Lo, "Analysis of a probe-fed microstrip disk antenna", *IEE Proc. H Microw. Antennas Propag.*, vol. 138, no. 2, pp. 185–191, Apr. 1991.

[73] G. Minatti, E. Martini, and S. Maci, "Efficiency of Metasurface Antennas", *IEEE Trans. Antennas Propag.*, vol. 65, no. 4, pp. 1532–1541, Apr. 2017.

[74] S. M. Seo and J.-F. Lee, "A fast IE-FFT algorithm for solving PEC scattering problems", *IEEE Trans. Magn.*, vol. 41, no. 5, pp. 1476–1479, May 2005.

[75] Fasenfest, Capolino, Wilton, Jackson, and Champagne, "A fast MoM solution for large arrays: Green's function interpolation with FFT", *IEEE Antennas Wirel. Propag. Lett.*, vol. 3, pp. 161–164, 2004.

[76] F. Vernì, M. Righero, and G. Vecchi, "On the Use of Entire-Domain Basis Functions and Fast Factorizations for the Design of Modulated Metasurface", *IEEE Trans. Antennas Propag.*, vol. 68, no. 5, pp. 3824–3833, May 2020.

[77] P. Baccarelli, S. Paulotto, D. R. Jackson, and A. A. Oliner, "A New Brillouin Dispersion Diagram for 1-D Periodic Printed Structures", *IEEE Trans. Microw. Theory Tech.*, vol. 55, no. 7, pp. 1484–1495, Jul. 2007.

[78] S. Paulotto, P. Baccarelli, F. Frezza, and D. R. Jackson, "A Novel Technique for Open-Stopband Suppression in 1-D Periodic Printed Leaky-Wave Antennas", *IEEE Trans. Antennas Propag.*, vol. 57, no. 7, pp. 1894–1906, Jul. 2009.

[79] J. Liu, W. Zhou, and Y. Long, "A Simple Technique for Open-Stopband Suppression in Periodic Leaky-Wave Antennas Using Two Nonidentical Elements Per Unit Cell", *IEEE Trans. Antennas Propag.*, vol. 66, no. 6, pp. 2741–2751, Jun. 2018.

[80] N. Yang, C. Caloz, and K. Wu, "Full-Space Scanning Periodic Phase-Reversal Leaky-Wave Antenna", *IEEE Trans. Microw. Theory Tech.*, vol. 58, no. 10, pp. 2619–2632, Oct. 2010.

[81] S. Paulotto, P. Baccarelli, F. Frezza, and D. R. Jackson, "Full-Wave Modal Dispersion Analysis and Broadside Optimization for a Class of Microstrip CRLH Leaky-Wave Antennas", *IEEE Trans. Microw. Theory Tech.*, vol. 56, no. 12, pp. 2826–2837, Dec. 2008.

[82] S. Otto, A. Al-Bassam, A. Rennings, K. Solbach, and C. Caloz, "Radiation Efficiency of Longitudinally Symmetric and Asymmetric Periodic Leaky-Wave Antennas", *IEEE Antennas Wirel. Propag. Lett.*, vol. 11, pp. 612–615, 2012.

[83] S. Otto, A. Al-Bassam, A. Rennings, K. Solbach, and C. Caloz, "Transversal Asymmetry in Periodic Leaky-Wave Antennas for Bloch Impedance and Radiation Efficiency Equalization Through Broadside", *IEEE Trans. Antennas Propag.*, vol. 62, no. 10, pp. 5037–5054, Oct. 2014.

[84] E. Abdo-Sánchez, M. Chen, A. Epstein, and G. V. Eleftheriades, "A Leaky-Wave Antenna With Controlled Radiation Using a Bianisotropic Huygens' Metasurface", *IEEE Trans. Antennas Propag.*, vol. 67, no. 1, pp. 108–120, Jan. 2019.

[85] F. Giusti, S. Maci, and E. Martini, "Complete Open-Stopband Suppression Using Sinusoidally Modulated Anisotropic Metasurfaces", *IEEE Trans. Antennas Propag.*, vol. 71, no. 11, pp. 8537–8547, Nov. 2023.

[86] A. F. Horn, P. A. LaFrance, J. W. Reynolds, and J. Coonrod, "The influence of test method, conductor profile and substrate anisotropy on the permittivity values required for accurate modeling of high frequency planar circuits", *Circuit World*, vol. 38, no. 4, pp. 219–231, Jan. 2012.

[87] I. Lindell, A. Sihvola, and I. Hänninen, "Perfectly anisotropic impedance boundary", *IET Microw. Antennas Propag.*, vol. 1, no. 3, p. 561, 2007.

[88] M. Zucchi, A. Guida, and G. Vecchi, "Adaptive Weighting Scheme for Multi-Objective Optimization in Metasurface Antenna Design", in *2024 18th Eur. Conf. Antennas Propag. EuCAP*, Glasgow, Mar. 2024, pp. 1–4.

This Ph.D. thesis has been typeset by means of the TEX-system facilities. The typesetting engine was pdfLATEX. The document class was `toptesi`, by Claudio Beccari, with option `tipotesi=scudo`. This class is available in every up-to-date and complete TEX-system installation.